Politecnico di Milano

School of Industrial and Information Engineering
Department of Electronics, Information and Bioengineering
Master of Science in Biomedical Engineering


# Leveraging a Neurocomputational Model in Multiple Sclerosis

Supervisor: Prof. Giuseppe BASELLI
Foreign Supervisor: Prof. Dr. Ir. Jeroen VAN SCHEPENDOM
Foreign Co-Supervisor: Prof. Dr. Ir. Guy NAGELS

Master Thesis of:
**Chiara ROSSI** Matr. 896259

Anno Accademico 2019-2020

Alla mia Super Nonna Maria.
Alla mia Super Famiglia.

*Trust Yourself.*

# Abstract

Multiple Sclerosis, MS, is a chronic neurological disease, that entails cognitive impairment in 40% to 70% of cases, and one of the most affected cognitive domains is information processing speed, IPS. Mainly due to demyelination, a characteristic phenomenon of multiple sclerosis, a delay in the conduction velocity characterizing the communication between brain regions is introduced. This thesis implements a neurocomputational model, the time-delayed coupled oscillators, to assess the impairment of the conduction velocity, and hence IPS. Given a MEG dataset including 50 healthy and 100 MS subjects, the resting-state brain activity is evaluated by computing the Functional Connectivity, FC, matrix; in parallel, the simulated FC is inferred from brain resting-state activity simulated by the model when it is given in input the structural connectivity of the subject or group in analysis. Empirical and Simulated FC are correlated to elicit the optimal model parameter, $\tau$, time delay, that permits the model to emulate the brain resting-state dynamics at the best. This parameter represents a delay between brain regions network interactions, due to finite conduction velocity, and it is expected to vary in agreement with IPS impairment. The model's performances are consistent with literature results when healthy subjects are investigated. Moreover, the optimal conduction delay $\tau$ shows some variations between the simulations of the healthy and the MS population, depicting the model ability to simulate the impairment in the conduction velocity. However, the variations detected at group level are not elicited in the subject specific simulations, where $\tau$ variations do not seem to correlate with CI features. The limitation can be related to the static perspective of the investigation, and future analyses might consider optimizing model parameters by matching the simulated and empirical dynamic properties of the brain activity.

**Keywords**: Multiple Sclerosis, MEG, Resting State, Neurocomputational Model, Kuramoto Model.

# Sommario

La sclerosi multipla è una malattia neurodegenerativa che colpisce il sistema nervoso, e comporta un deterioramento cognitivo nel 40-70% dei pazienti, colpendo particolarmente il dominio della velocità di elaborazione delle informazioni. A causa del fenomeno di demielinizzazione caratteristico della sclerosi multipla, è introdotto un ritardo nella velocità di comunicazione tra distinte regioni cerebrali. Questa tesi ha lo scopo di investigare il deterioramento della velocità di elaborazione attraverso l'implementazione di un modello computazionale di oscillatori accoppiati con ritardo temporale. Da un dataset di 150 soggetti, 50 sani e 100 pazienti con sclerosi multipla, l'attività cerebrale a risposo acquisita attraverso magnetoencefalografia è analizzata attraverso l'estrazione della matrice di connettività funzionale statica. Attraverso la correlazione della connettività funzionale sperimentale con quella simulata, estratta dalla attività cerebrale simulata dal modello, si identifica il parametro ottimale $\tau$ che permette al modello di emulare l'attività magnetoencegalografica. Questo parametro identifica il ritardo temporale nella comunicazione tra distinte aree cerebrali, e si ipotizza l'identificazione di un incremento di questo ritardo, e dunque del parametro $\tau$, nella popolazione di pazienti con sclerosi multipla, data la compromissione della velocità di elaborazione delle informazioni. Le prestazioni del modello sono coerenti con i risultati della letteratura quando vengono studiati soggetti sani. Nel confronto delle prestazioni del modello quando sono considerate la popolazione sana e quella dei pazienti con sclerosi multipla, si rileva una variazione del parametro ottimale $\tau$, e dunque il modello sembra simulare il ritardo di conduzione caratteristico della patologia. Invece, i parametri $\tau$ delle simulazioni sui singoli soggetti non sembrano riprodurre i risultati ottenuti nelle analisi a livello di popolazione. La principale limitazione riguarda la prospettiva statica dell'indagine e analisi future potrebbero prendere in considerazione l'ottimizzazione dei parametri del modello facendo corrispondere le proprietà dinamiche simulate ed empiriche dell'attività cerebrale.

**Parole Chiave**: Sclerosi Multipla, MEG, Modello computazionale, Modello di Kuramoto.

# Contents

# Glossary

| Abbreviations | Meaning |
|---|---|
| **CI** | Cognitive Impairment |
| **CNS** | Central Nervous System |
| **DTI** | Diffusion Tensor Image |
| **DWI** | Diffusion Weighted Imaging |
| **EC** | Effective Connectivity |
| **FC** | Functional Connectivity |
| **HC** | Healthy Control |
| **IPS** | Information Processing Speed |
| **k** | Global Coupling Strength |
| **MEG** | Magnetoencephalography |
| **MRI** | Magnetic Resonance Imaging |
| **MS** | Multiple Sclerosis |
| **MSB** | Multiple Sclerosis - Benzodiazepine positive |
| **SC** | Structural Connectivity |
| **SNR** | Signal to Noise Ratio |
| $\theta$ | Oscillators' Phase |
| $\tau$ | Time Delay |

# List of Figures

# List of Tables

# Chapter 1

# Introduction

In order to properly understand the work conducted throughout this thesis, this introduction illustrates briefly the context of research, and introduces some concepts and key-points which the further analysis refers to. Therefore, this section does not aim at being exhaustive, but at defining a backbone knowledge for the following sections. Based on these considerations, some anatomical and physiological aspects of the *Central Nervous System, CNS*, are presented, as well as the bases and mechanisms of some neuroimaging techniques used to study both the neuroanatomy and neurophysiology.
Before developing this chapter, a small paragraph introduces the research objectives of this thesis, to contextualize the work.
This section's references are mainly [9, 10, 11], unless it is specified that another source is cited.

## Aims

Cognition is a commonly impaired trait in neurodegenerative diseases, such Multiple Sclerosis, MS [12, 13]. Late researches aim to identify reliable and objective parameters, *biomarkers*, that can overcome the pitfalls of neuropsychological tests, and provide a quantitative measure of the cognitive impairment [14]. These markers can be extracted by the employment of neuroimaging techniques and neurocomputational models, studying the performances of the model parameters in function of the different pato-physiological conditions. This thesis is developed in this research context, aiming to find a quantitative measure that can be related to the impairment of the specific cognitive domain, *information processing speed, IPS*. The analysis is conducted on an extended MEG dataset containing both healthy and MS subjects, and a novel neurocomputational model, the time-delayed coupled oscillators is applied. The work consists in three major work parts:

1. **Validation of the model**: the first important analysis consists in reproducing the important literature results proposed by Cabral et al. [5]. By applying the modified Kuramoto Model on the available dataset, the model performances are validated.
2. **Population level analysis**: the model is employed to simulate the activity of groups of subjects with different conditions: Healthy, MS, MS-Benzo+. A qualitative evaluation of the model performances is conducted.
3. **Subject level analysis**: the model is used to simulate subject brain activity. The final analysis aims at identifying the potential model parameter that traces the subject pathological condition.

## 1.1 The Brain

The brain, together with the spinal cord, constitutes the *central nervous system, CNS*. This is one of the most complex systems in the human body, both considering its functionality, which is not yet completely understood, and its anatomical structure. The development and arrangement of the functional and anatomical building block, *the neuron*, resemble a network. Each network's thread is composed of a series of neurons that, communicating with each other, transfer the information between different network's nodes. This description focuses on the microscopic level, but a parallelism is observed between the microscopic and macroscopic organization of the CNS[8]. Consequently, the macroscopic structure of the brain can be investigated as a network as well. In the following section, how this network is built and its characteristics are described. One of the most characteristic aspects of the brain, is the intrinsic relationship between structure and function of each component, and this dissertation aims at highlighting this aspect.

### 1.1.1 Microscopic Level

#### Anatomy

At cellular scale, the structural and functional building block of the CNS is found: *the neuron*. This has the intrinsic characteristic to be electrically sensible: the information within the cell is coded as an electrical signal. There are several morphologies of neurons, nevertheless, four main parts are always identifiable. These four structures vary among neurons' typologies, depending on the neuron's anatomical location and function. Below, each component is described, and displayed in figure 1.1:

- Dendrites: cell's hair.
  Dendrites are protuberances detecting adjacent neuronal activity. These function as receiving channels for the incoming information.
- Soma: cell's body.
  In this portion, the information coming from neighboring neuronal activity is processed and integrated both spatially and temporally.
- Axon: cell's tail.
  This component embodies the channel along which the information is transferred from the soma to the opposite extremity. The beginning part of the axon is entitled as the *Axon Hillock*. This region is characterized by a trigger zone where an Action Potential, AP, can arise, when specific conditions are fulfilled. This phenomenon is explained in the following section 1.1.1, here it is referred as a general electrical event. The length of an axon can vary from a few *mm* to about a meter, depending on the anatomical location of the cell. Most of the neurons have their axons partially wrapped into a myelin sheath, and for this characteristic these are defined *myelinated neurons*. This is an important aspect affecting the *conduction velocity*. This last concerns the speed of information transfer along the axon.
- Synaptic Terminal: cell's hand.
  This part characterizes the neuron's terminal region, where the AP is transmitted to the following step of communication, the post-synaptic neuron. The phenomenon concerning the information transfer is defined *synapsis*, and it is explained in the following section.

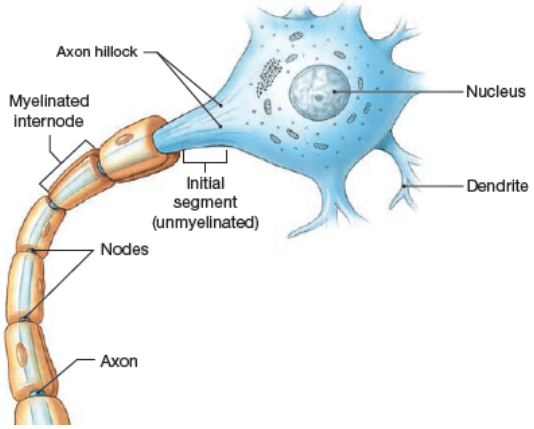


**Figure 1.1:** Brain functional and structural building block: The Neuron. Four main parts of the structure are identified, with the related features.

Here it is introduced the second group of cells presents in the central nervous system: the non-neural cells or *Glia cells*. These compose a big and varied ensemble, whose roles consist in supporting and sustaining the neurons' structure and functionality. The following figure 1.2 shows a scheme of the main typologies of Glia cells, with the related functions.

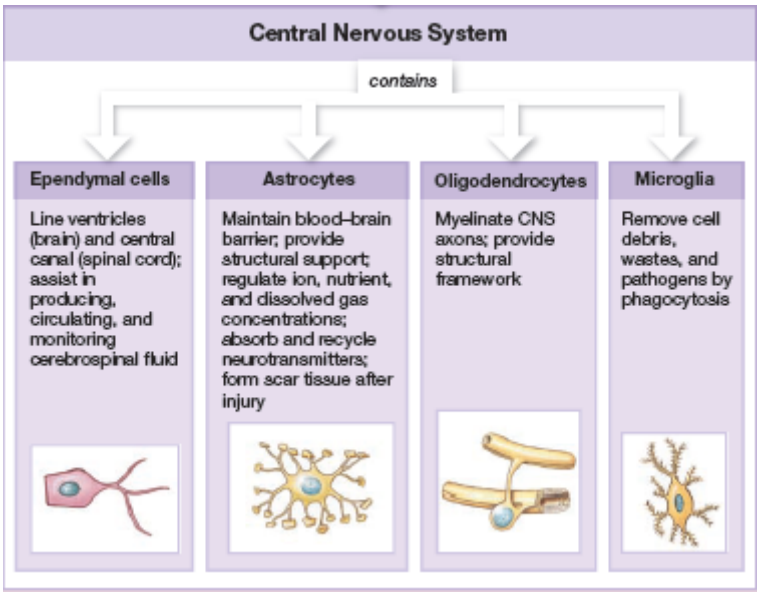


**Figure 1.2:** In this table, the main types of non-neuronal cells are presented, with the related functions and roles in the CNS.

The group of non-neural cells that is worth mentioning concerns the *Oligodendrocytes*. These cells are responsible for building the *myelin sheaths* around the axons. The characteristic Olygodendrocytes' protuberances are flat structures of two membrane layers with a very thin intracellular space in between, that wrap the neuronal axon in defined regions, creating an extra concentric layer of plasma membrane, *the sheath*, figure 1.3. This structure is lipid, therefore, it allows to electrically isolate the axon from the extracellular space, decreasing the ionic and water leakages towards the outside, and increasing the conduction velocity along the axon.

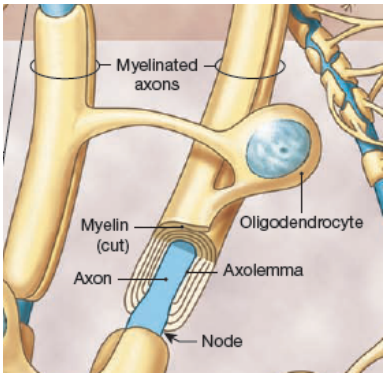


**Figure 1.3:** This picture presents a zoom on the structural interaction between an Oligodendrocyte and an axon.

A single oligodendrocyte can provide myelin sheaths to different neuronal axons. However, these coated layers do not cover the whole axon's length, but only small portions, which are interposed by unmyelinated regions, *the nodes of Ranvier*, as shown in figure 1.3.

### Physiology: The Action Potential

As mentioned in the previous section, neurons are electrically sensible cells, which code the information as an electrical signal identified as an *action potential, AP*. Following, the functions related to the anatomy previously described is briefly introduced.

### Action Potential

The cellular membrane is a semipermeable structure composed of a lipid double layer. Small and uncharged substances pass through the membrane, while big and/or charged molecules can cross the membrane through specific protein-based structures, the *ionic channels*, shown in figure 1.4. These channels can either be passive or active. Those demanding energy to move a particle from the intracellular to the extracellular space or vice versa are defined as *active*. An example of an active ionic channel is the *Na-K pump*. As shown in figure 1.4, this channel transports 2 atoms of $K^+$ inside the cell, and 3 atoms of $Na^+$ outside, moving the particles against gradient of concentration. Instead, the diffusive movement occurs through passive channels, and it is driven by a difference in ionic concentration among the extracellular and intracellular space. Considering $Na^+$ and $K^+$, the velocity of the active transfer does not match the one related to free ionic movement, and a difference in chemical and ionic composition between intracellular and extracellular spaces occurs. Consequently, an electric voltage gradient is developed over the cellular membrane, *the Membrane Potential*. Generally, a resting membrane potential is set around $-70mV$, and no specific cellular activity is associated to it.

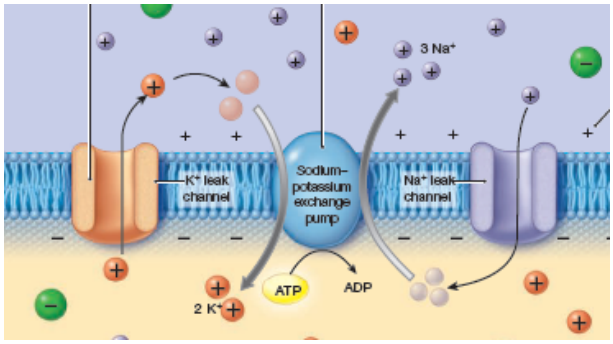


**Figure 1.4:** This figure pictures an active Na-K Channel, describing how the Membrane Potential is developed.

Changes in membrane potential are induced by variations in membrane's permeability to specific ions, due to inter-cellular interactions defined as synapses; these can be either electrical or chemical interactions. Electrical synapses are based on direct communication channels between neurons, allowing fast information transfer. On the other hand, chemical synapses convert the electrical information into a chemical event, in which a certain *type* and *amount* of chemical transmitters, neurotransmitters, are released by the pre-synaptic neuron. These are detected by neighbouring neurons' dendrites by specific bounding receptors. This interaction induces changes in the membrane permeability of the post-synaptic neuron, and an ionic current alters the membrane potential. The interaction is defined as inhibitory, IPS, when the membrane potential is decreased, while an excitatory synapses, EPS, increases the membrane potential. One neuron takes part to several synapsis as a post-synaptic neuron, and all the resulting interactions at the level of its dendrites, are then integrated both in time and space, to elicit the overall outcome. This last is coded in the resulting membrane potential. When this reaches a certain threshold, e.g. $-55mV$, an action potential is triggered at the Axon Hillock. This is an *all-or-nothing event*, where a cascade of events concerning different ionic currents makes the membrane potential fluctuate in a specific point of the axon. The mechanisms characterizing this process are shown in figure 1.5.

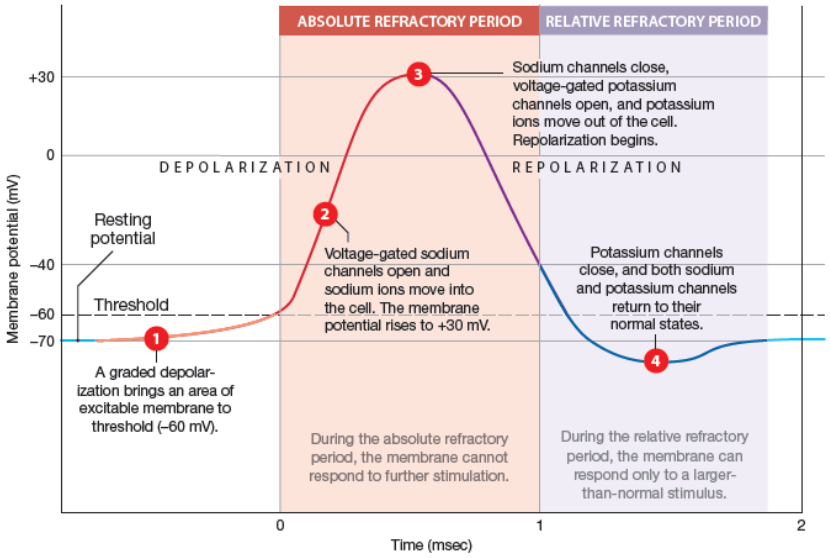


**Figure 1.5:** The cascade of events characterizing an Action Potential is shown.

When an action potential arises, the ionic currents involved induce relative currents in the adjacent regions, which make the membrane potential vary in these points, as pictured in figure 1.6. When the perturbation takes the membrane potential of the adjacent axonal point above the threshold, a new AP occurs, and the same process is repeated. The recurrence of an AP along an axon

characterizes the mechanism employed to transfer information along the axon itself, and, depending on the neuronal structure, the conduction speed can vary. In fact, the AP arises every infinitesimal portion of axon when this last is unmyelinated. Therefore, the conduction speed results very slow, about 2 m/s, and due to spontaneous ionic diffusion, the propagating current is partially lost along the axon. Conversely, the conduction velocity is very high concerning a myelinated axon, from 5 to 120 m/s, depending on the axon's diameter and length. In this case, the AP arises only in the nodes of Ranvier, whilst the current runs undisturbed between nodes, where the axon is wrapped into a myelin sheath. This characteristic conduction mechanism is defined as *saltatory conduction*. The lipid sheath increases the resistance of the plasma membrane, and the probability of current leaking is very low, as shown in figure 1.6. When a neurological disease affects the conduction velocity, this is the disrupted mechanism.

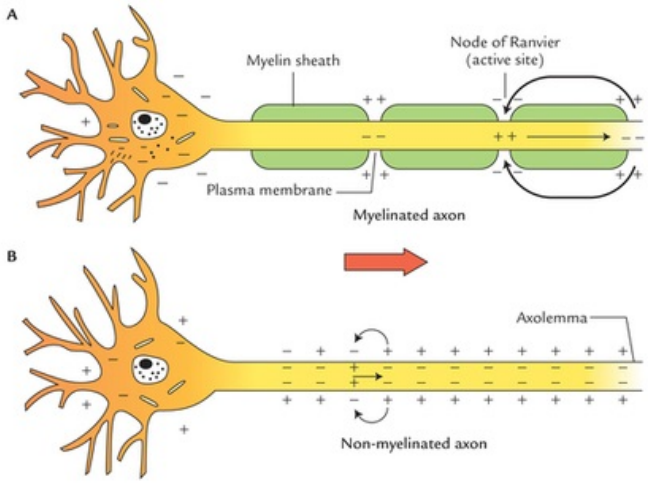


**Figure 1.6:** A) The mechanism of saltatory conduction in a myelinated neuron is displayed. B) The mechanism of Non-saltatory conduction in a non-myelinated neuron is presented. The figure shows how the action potential affects adjacent regions, generating currents that modify the adjacent membrane potential. This creates the condition to trigger a second action potential in the following point.

### 1.1.2 Macroscopic Level

#### Anatomy

The following step of discussion concerns the investigation of the brain's structure above the cellular level. At this scale, two parts can be identified in the brain, based on two different colors: *white* and *grey matter*, recognizable in figure 1.7. The former consists of an aggregation of neuronal somas; the latter, instead, is composed of bundles of axons, and the characteristic white color is given by the presence of myelin sheaths, lipid components.

**Figure 1.7:** In this figure an horizontal cross-section of the brain is shown. Two parts are identifiable, characterized by two different colors, Grey and White matters.

Anatomically, the brain is divided into two hemispheres which have almost the same symmetrical structure. The division can be identified by the longitudinal fissure, a big groove splitting the brain into two halves, two hemispheres, characteristics observable in figure 1.8. For each hemisphere, the cortex, the outer surface of the whole brain, is divided into four lobes: frontal, parietal, temporal and occipital, figure 1.11. Each lobe contains grey matter involved in the processing of specific functions. Focusing on white matter, the fibers are classified considering which brain regions they connect. The commissural fibers run across the corpus callosum connecting the two hemispheres, the association fibers connect regions within the same hemisphere, and last, the projection fibers bond cortical with non-cortical regions, figure 1.8.

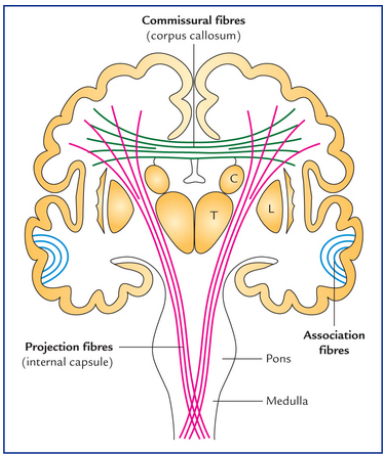


**Figure 1.8:** This figure shows bundles of fibers connecting different parts of the brain.

The cortex is characterized by a folded-like shape, creating sulci and gyri. This configuration allows to increase the total brain surface, and therefore, the amount of grey matter in the cortex. Microscopically, pyramidal neurons are the cortical functional and structural units of this portion. These have triangular body, spread branches-like dendrites, and their axons run perpendicular to the cortical surface. Groups of pyramidal neurons develop their axons all in parallel. The cortex' thickness is about $2 - 4$ mm, and 6 different layers are identified along the axonal lengthening direction by grouping of pyramidal somas, as shown in figure 1.9.

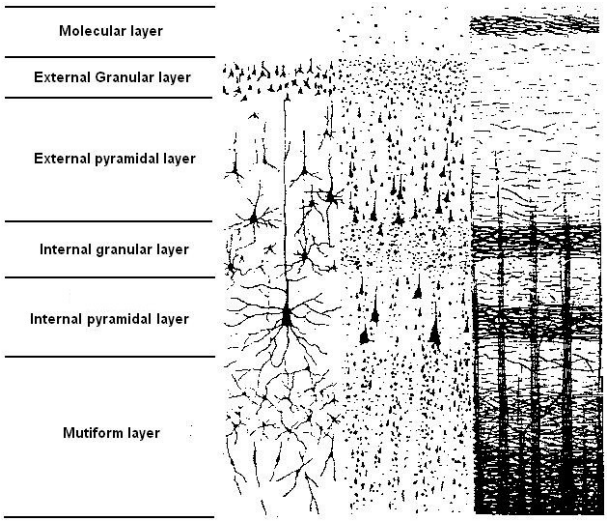


**Figure 1.9:** Pyramidal Neurons. Their characteristic disposition in the cortical region is displayed, showing the different layers.

### Physiology: what is brain activity at the macroscopic level?

A step forward concerns the investigation of macroscopic brain activity, starting from the microscopic activity described in the previous section. Microscopically, an action potential causes a membrane potential variation of about $80mV$, and this provokes an extracellular current, defined as *secondary current*. This last evokes a very small voltage potential of about $600\mu V$ next to the neuron's membrane. However, due to its small amplitude, this potential is dissipated in the range of sub-mm. These processes are shown in figure 1.10.

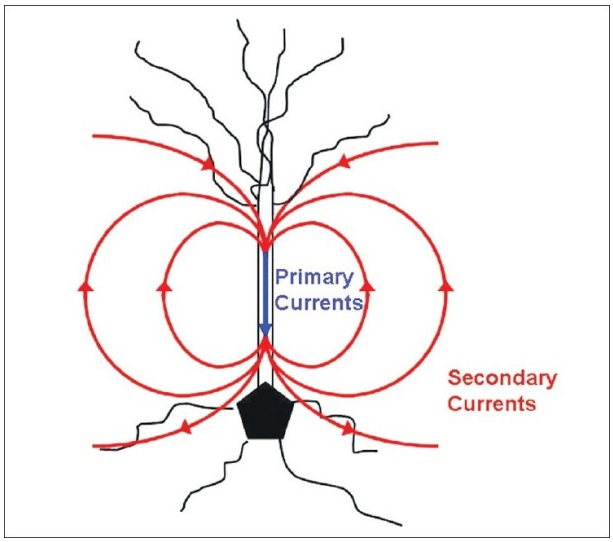


**Figure 1.10:** This figure displays the primary and secondary currents concerning a pyramidal neuron. When several of these structures are put in parallel, a summation of secondary currents occur both in time and space.

However, a particular case concerns pyramidal neurons. Groups of neighbouring pyramidal cells work close together to accomplish the same function, and this phenomenon is displayed by simultaneous firing. The parallel arrangement of pyramidal neurons make the related action potentials run in parallel, and a summation of all the secondary currents occurs. This can reach the skull,

developing an electrical voltage of about $100\mu V$, detectable on the scalp surface. This last quantity is the macroscopic expression of microscopic activity, which cannot be investigated directly, unless invasively. However, depending on the scale of examination, the number of functional segregated regions in the brain can vary. An observation follows: when conducting an investigation regarding brain's anatomy or physiology, a proper observational scale must be selected, to identify the brain functional parcellation that better corresponds to the objective of investigation. In figure 1.11, a very common and general functional subdivision of the cortex is shown.

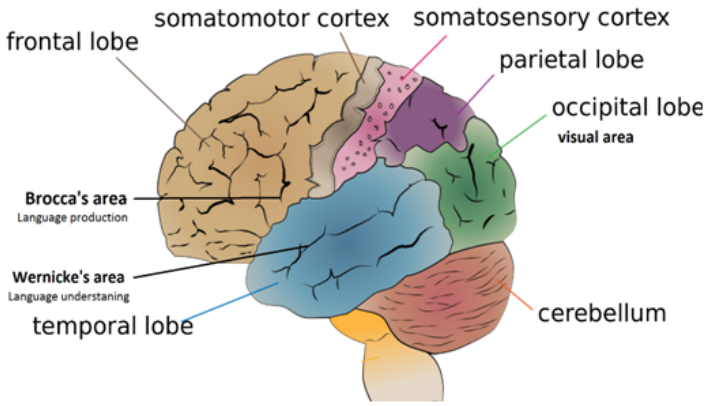


**Figure 1.11:** Sagittal section of the brain showing the macroscopic structures.

To date, a general neuranatomical and neurophysiological description of the brain is presented, considering a normal condition, a healthy brain; what happens when the brain functionality or structure is damaged? What is a neurological disease? In this work, the neurological disease in analysis is Multiple Sclerosis, MS, and the following section presents an overview on the pathology.

## 1.2 Multiple Sclerosis

Multiple Sclerosis (MS) is one of the most common chronic and non-traumatic diseases that affect the Central Nervous System, interesting about 2 to 2.5 million people worldwide[2, 12]. It is diagnosed mostly between young adults, in the age-range of $20 - 40$ years old, and the lifespan is reduced of about $5-10$ years in average[15]. Multiple Sclerosis is more common among women, with a lifetime risk of 2.5%, against the 1.4% for men, representing an important health and economic burden for the community[12, 16]. Although it is increasingly considered a global disease, it is known to be unevenly distributed worldwide[2, 16].

### 1.2.1 MS Pathology

Multiple Sclerosis is a heterogeneous and complex disease when its pathophysiology is examined. The physiological mechanisms underlying this pathology are *inflammation, demyelination* and *neurodegeneration*[17, 18]. At first, MS was considered to affect mainly white matter; however, recent studies show the importance and burden of grey matter damages, as well[1].

Traditionally, MS is considered an autoimmune disease driven by activated and autoreactive T-cells. These transmigrate through the blood-brain barrier, and develop *lesions* characterized by a particular inflammatory process. This inflammation triggers demyelination and neural or axonal damage, which might vary in intensity depending on the tissue susceptibility, and the intensity of the autoimmune reaction. The occurrence of these lesions is scattered all over the CNS, and it is characterized by a high inter-subject variability[18, 19]. In figure 1.12, two possible pathways

are shown to explain the possible relationships between different mechanisms producing a lesion. Pathway **A** shows the most traditional causal interactions. On the other side, pathway **B** displays a new perspective, where atrophy and neurodegeneration trigger the autoimmune reaction that causes inflammation. To date, there is no more or less plausible pathway, and the discussion is still open[1].

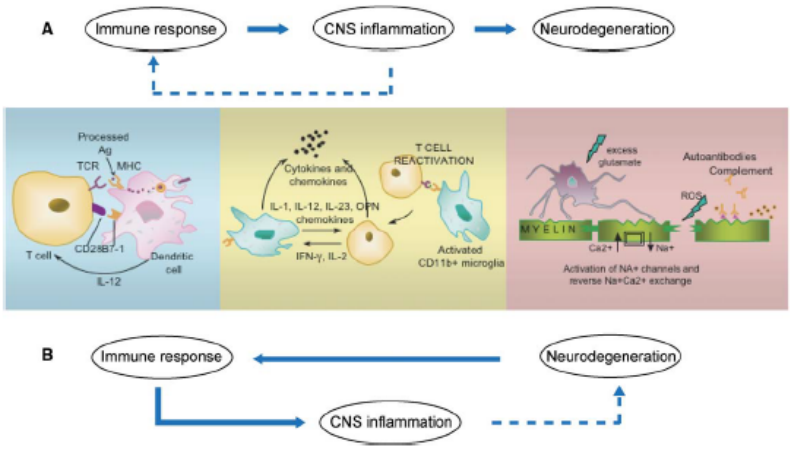


**Figure 1.12:** The three patho-physiological mechanisms are displayed, in the blue block the immune response, in the yellow one the inflammatory process and in the pink block neurodegeneration. Two workflows, A and B, show how these mechanisms interplay and might be related[1].

Each mechanism is characterized by several possible origins and development pathways. Considering inflammation, this impairs myelin sheaths, making the wrapped axonal structure damageable. Furthermore, inflammation can disrupt the metabolism of support-myelin oligodendrocytes, resulting in the same demyelination effect[19]. Despite this general description of demyelination and inflammation, four patterns are identified in which several factors are involved. These are described in figure 1.13. Next to demyelination, remyelination might occur in early stages, however, the healing process becomes more and more partial along the disease progression. The debate is

| Patterns of demyelination | Pathology | Putative mechanisms |
|---|---|---|
| **(I) Macrophage mediated** | Perivenous distribution of lesions;<br>Radial expansion of the lesions;<br>Inflammatory infiltrates composed of T-cells and macrophages;<br>Activated macrophages and microglia associated with degenerating myelin. | T-cell-mediated inflammation with macrophage/microglia activation;<br>Demyelination induced by macrophage toxins. |
| **(II) Antibody mediated** | Similar lesions as in I but additional deposition of immunoglobulin and activated complement at sites of active myelin destruction | T-cell-mediated inflammation with macrophage/microglia activation;<br>Complement mediated lysis of antibody-targeted myelin |
| **(III) Distal oligodendrogliopathy** | Inflammation by T-cells and macrophages;<br>Small vessel vasculitis with endothelial cell damage and microvessel thrombosis;<br>Degeneration of distal oligodendrocyte processes, followed by oligodendrocyte apoptosis and demyelination | T-cell-mediated small vessel vasculitis with secondary ischemic damage of the white matter |
| **(IV) Primary oligodendrocyte damage with secondary demyelination** | Similar lesion as in (I), but prominent oligodendrocyte degeneration in a small rim of periplaque white matter | T-cell-mediated inflammation with macrophage/microglia activation;<br>Demyelination induced by macrophage toxins on the background of metabolically impaired oligodendrocytes;<br>Genetic defect of oligodendrocytes? |

**Figure 1.13:** Four possible patterns for inflammatory processes.

still open on the mechanism underlying the neurodegeneration process affecting grey matter. Due to a shortage in myelin, these regions are more likely to be affected by inflammation, compared to white matter regions. Nevertheless, grey matter damages concern also atrophy, which might be

related to an indirect neuronal degeneration mechanism. Although white and grey matter damaging processes might seem similar, they are found to be independent. Moreover, lesions located in the brain or in the spinal cord are observed to develop independently as well[20]. The proposed considerations refer mainly to an early stage of relapsing MS; however, when a progressive case is evaluated, different characteristics in the neurodegenerative process are highlighted. In fact, neurodegeneration becomes a relentless process of death and decay of neural structures, and autoimmune treatments are less effective. This might be caused by an impossibility to reach the lesion that is chronically active and slowly expanding, due to the blood-brain barrier[20]. This brief overview on the mechanisms underlying MS shows the complexity of this pathology. Each mechanism is associated to the patient's sensitivity and correlated factors, meaning that this mechanisms are extremely individual-dependent[2, 19]. Given these last observations, one can assume the limited efficacy of therapies.

### 1.2.2 Origin and Causes

A unique and certain cause underlying Multiple Sclerosis is not found yet. Nevertheless, several studies show that an interplay of genetic and environmental factors guides the development of this disease[15, 16]. As far as genetics is concerned, MS is not considered a hereditary disease[2, 21]. Despite this, a genetic contribution is strongly increasing with respect to the rest of the involved factors. The evidence supporting this statement concerns the growing risk to develop MS, when it is already exhibited in siblings[1]. Moving to consider the environmental factors, the phenomenon is multifaceted and heterogeneous, which leads to different ways to approach the topic. Some population-based studies show an uneven geographic spread of the disease, supporting the finding for which environmental factors affect MS development. One of the geographic factors is the Latitude[2]. In fact, countries higher in latitude, such as in northern Europe, are more likely to present bigger MS population with respect to country such as central America or central Africa. First, it is observable that the two mentioned regions are very different, both considering the size of the population and the degree of development. Therefore, it is important to take into consideration that the number of identified cases is bigger in much populated areas, and in those countries where there are more resources to detect and monitor this pathology. Nevertheless, intrinsic environmental factors are considered as well. One worth mentioning is the sunlight exposure, and related to this, the Vitamin D concentration. Although the real role of vitamin D is still to be investigated, this is considered an important protective agent against axonal damage[2, 16]. Therefore, in countries where sun exposure is relatively low, the risk of developing MS is higher. Moreover, migrating in these countries before the age of 15, can also be considered an additional risk, which highlights the importance of the time of exposure. Childhood and adolescence are critical time frames, as well as the gestational period[2, 16]. Two more factors are listed: smoking and Epstein-Barr virus[15, 16]. As far as this brief analysis is concerned, one can notice the complexity and heterogeneity of MS in terms of causes and thus, possible prevention strategies[2, 21].

### 1.2.3 Classification

MS can be classified regarding the course observed at disease onset. Two main classes are identified, the relapsing onset MS and the progressive onset MS[2]. Despite this distinction, in some cases, features concerning both domains can appear, especially when the disease enters late stages. Before MS diagnosis, there is a stage defined as *clinically isolated syndrome*, whereby a single relapse occurs. A relapse is an event characterized by an "acute inflammation and demyelination of a specific CNS region, that lasts for at least 24 hours, and in absence of fever and infections"[2, 22]. Afterwards, the probability to develop MS increases with aging and time[15].
The first and most frequent class is *Relapsing/Remitting MS, RRMS*, which occurs in 85% of the MS patients. The onset age is set around 25 years old, and women are twice as likely to be affected as men[1]. A relapse characterizes RRMS onset and its development. This episode occurs with a rate of once every two years, however, the course of this event is random, and unpredictable[15].

After a relapse, a recover period follows over days or weeks, leading to a partial or total recovery. Typical relapses' effects result in optic neuritis, sensory deficits or cerebellar dysfunctions[2, 16]. *Primary progressive MS, PPMS*, is the second most frequent MS class. This condition affects approximately 15% of the MS patients, without gender preference. The age at which the disease onset is observed around 40 years old[1, 23]. In this case no relapses occur, but the pathophysiology is characterized by white and grey matter atrophy, and neuro-degenerative processes take place dominantly. This condition is mainly characterized by spinal symptoms such as gait ataxia, paresis and spasticity. Although in a pure progressive form no relapses are identified, in 40% of the cases relapses occur along the disease progression; this condition is pointed as *progressive relapsing MS, PRMS*[2]. Another progressive form exists, the *secondary progressive MS, SPMS*[2]. This condition is not diagnosed as a primary form of MS. However, it represents the second stage of a RRMS, and it is identified once the disease enters in a stage characterized by a gradual and continuous disease progress and worsening[2]. In certain cases, superimposed relapses can be shown in this stage as well. The following figure 1.14 shows the different MS typologies just described.

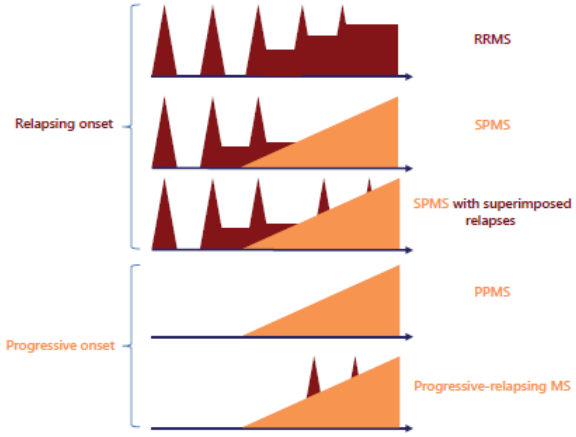


**Figure 1.14:** MS classification[2]

### 1.2.4 Symptoms, Cognitive Impairment and Assessment

Considering MS symptoms, a broad range involves motor, cognitive and neuropsychiatric aspects[13]. Physical and cognitive impairments are totally independent, and this makes the analysis more complicated[13]. In general, symptoms depend on where lesions occur, and how much white and grey matter is involved[15]. Moreover, the stage of the disease must be considered[16].

Multiple Sclerosis entails *Cognitive Impairment* in $40\% - 70\%$ of the MS cases[12, 13]. CI is detected in early stages of the disease, and its progress follows the disease course, yielding a possible marker for both MS detection and tracing of disease progression. Among all the cognitive domains, MS is found to affect only a few of them, and always the same: long-term memory, attention, information processing speed IPS, executive function, and learning[12]. Information processing efficiency and speed, are both impaired and the most disrupted cognitive domains in MS[13]. Information processing efficiency refers to the ability of working and elaborating the information stored in the working memory; whereas information processing speed refers to the velocity of elaboration. In order to assess cognitive impairment, the International Conference of MS Experts proposes a battery of 7 tests. These are referred as BICAMS, allowing to access all the impaired domains involved in MS[13]. Two tests are worth mentioning: the Expanded Disability Status Scala EDSS and the Multiple Sclerosis Functional Composite MSFC. EDSS scores motor or sensory-related performances in a scale with 8 functional systems, each one defined by a different degree of pathological severity. MSFC rates also cognitive performances[24]. The employment of tests in clinical practice entails some drawbacks. Patients tent to improve the performance due to practice-effects[14]. In addition to this, neuropsychological tests are time consuming, and the

performance is operator-dependent. In order to provide more reliable and objective assessments, neuroimaging techniques are more and more employed in clinical practise and research[13, 14]. In agreement with this, McDonald criteria for MS diagnosis have been reviewed in 2017, in order to insert parameters and findings acquired by Neuroimaging Techniques[15]. This new diagnosis approach is driven by two lesion-based criteria: *dissemination in space* and *dissemination in time*: lesions must occur in different CNS regions, and new lesions must be displayed with respect to a baseline scan. Depending on the location and spread of a lesion, different sets of symptoms can arise. This consideration introduces an additional challenge, and a low correlation between the radiological measurements and the actual physical or cognitive impairment is inferred. This phenomenon is addressed as *clinico-radiological paradox*, and it limits the employment of medical imaging techniques in clinical practise[24, 14]. Therefore, to extract useful information by the analysis of neuroimaging results, new *biomarkers* are required.

Among all the features characterizing this complex pathology, this thesis focuses on a specific cognitive domain: the *Information Processing Speed, IPS*. Due to demyelination and neurodegeneration, this cognitive domain is impaired, and a delay is introduced in the process of information transfer. This work aims at finding a biomarker to detect IPS impairment in Multiple Sclerosis.

## 1.3 Neuro-Imaging Techniques

In neuroscience, imaging techniques are employed to investigate the neurophysiology and the neuroanatomy, in healthy and pathological conditions. It is important that both these cases are evaluated, to understand the disease's effects on a healthy brain. In figure 1.15, imaging techniques are grouped into two classes, structural and functional investigation techniques.

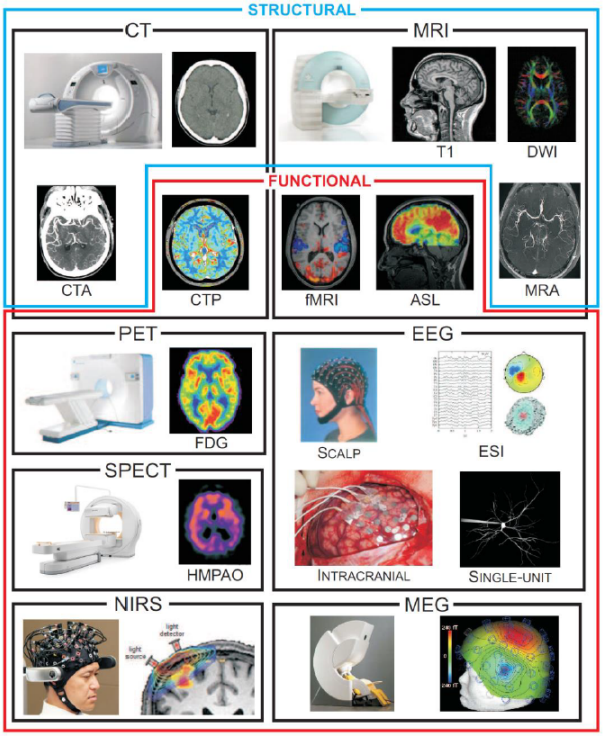


**Figure 1.15:** Imaging techniques are divided in two classes: functional and structural investigation techniques.

Another important classification concerns the *spatio-temporal resolution*, figure 1.16. When designing an experiment, it is very important to choose an investigation technique characterized by a proper spatio-temporal resolution with respect to the aim of the examination. Furthermore,

another set of parameters affecting this choice concerns the technique's sensitivity and specificity for a certain physiological signal, the technique's invasiveness, and possible artifacts.

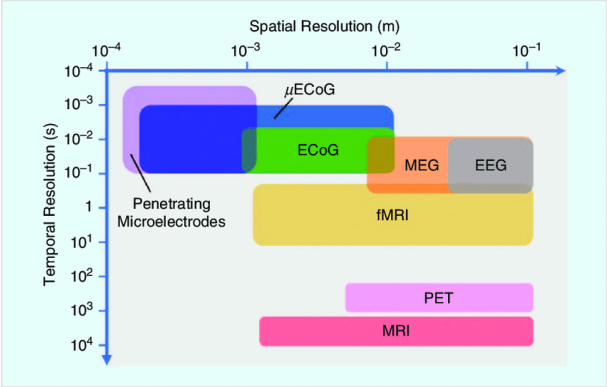


**Figure 1.16:** In this figure, some of the available imaging techniques are located in the spatio-temporal resolution plot.

The following sections aim at providing an overview on the techniques that have been employed to acquire the dataset utilized along this thesis.

### 1.3.1 Structural Investigation

Investigating brain anatomy is a challenge that researchers are pursuing for several decades already. They aim at accessing the brain anatomy in a non-invasive way, and with high spatial resolution[25, 26]. The technique described in this section is *Magnetic Resonance Imaging, MRI*, since it is one of the most employed techniques in neuroimaging, and part of this thesis relies on MRI data. During this last decade, MRI has gained a lot in popularity, especially for its high spatial resolution and the non-ionic physics involved. This technique has lots of potentialities, and enables the investigations of different aspects of the brain anatomy, such as the identification of white and grey matter regions, or the distribution of white matter tracts. Furthermore, MRI can be also employed in functional investigations[25, 27].

#### MRI: Working Principle

The first important quantity to introduce is the *spin angular momentum*, which is an intrinsic property of each atomic particle, proton, neutron, and electron. When it comes to a nucleus, the total spin momentum depends on its composition. In the human body, the atom that is present in the largest quantity is the *Hydrogen*, whose nucleus spin angular momentum is $\pm\frac{1}{2}$. As a proton, Hydrogen is characterized by a *magnetic momentum*[10], and MRI technique exploits this last property to image the protons distribution inside the body. The following steps show the technique's workflow[27, 28]:

1. In normal condition, the total magnetic momentum is equal to zero, since all the spins' magnetizations are randomly distributed, balancing one another. When an external static magnetic field, $B_0$, is introduced, all the spins align to this creating a global longitudinal magnetization, $M_L$, figure 1.17.

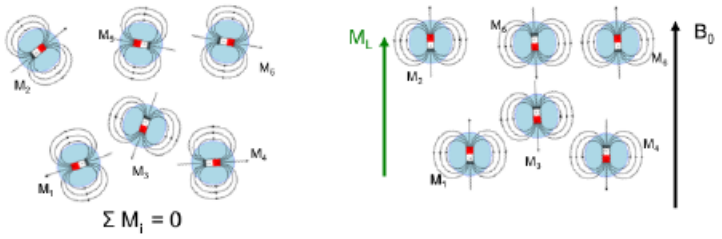


**Figure 1.17:** This figure presents two scenarios: the longitudinal magnetization of a region with and without an external static magnetic field, right and left respectively.

2. The spins and $B_0$ are not completely aligned, and a torque momentum acts on each proton, which rotates around the external static magnetic field axis. This rotation is characterized by an angular frequency, the *Larmor frequency*, characteristic for each atomic species.

3. The following steps aim at disturbing this static condition, and producing a signal that can be detected. In figure 1.18 a basic MRI sequence, the Spin-Echo MRI, is explained.

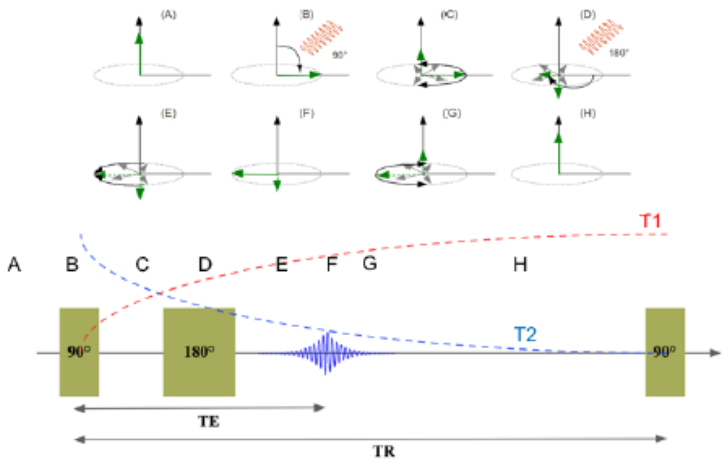


**Figure 1.18:** Steps of a classic MRI sequence.

With a Radio Frequency, RF, pulse (B), the longitudinal magnetization of each proton is bent of 90° with respect to $B_0$; the flip angle depends on the amplitude of the field and the time of exposure. While trying to recover, the spins dephase, because of the different Larmor frequencies (C). A RF pulse that flips the spins of 180° is applied, and the tangential magnetization, $M_T$, is recovered by the run of faster spins catching the slowest ones (D). When $M_T$ is completely recovered (F), the dephasing occurs again (G), and the signal dissolves, recomposing the initial $M_L$ (H). This technique is called *Spin ECHO*, because the measured signal is the echo of the real one. The RF pulses affect the spins only in case the RF's frequency is the Larmor frequency of the selected species to disturb (Hydrogen). The process of dissolution of the tangential magnetization and recover of the longitudinal one is called *relaxation*, and it is characterized by two independent time constants: $T_1$ and $T_2$. $T_1$ is the recovering time of $M_L$, while $T_2$ is the time of $M_T$ relaxation. An additional field is the *Gradient Field*. This is a linear varying magnetic field along each axis, used mainly for space encoding and Diffusion Weighted measurements. In fast scans, strong gradient fields may also affect the signal, thus resulting in gradient echoes.

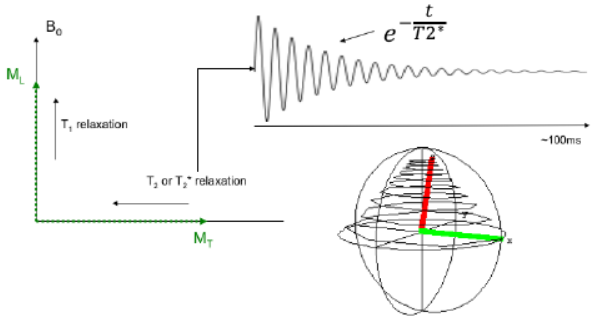


**Figure 1.19:** T1 and T2 time constants are shown with respect to the related mechanisms of relaxation. Moreover, the relaxation process is described as exponentially decaying.

4. The Larmor frequency is the frequency of dephasing when a spin is disturbed and therefore it is defined as:

$$\omega_L = \gamma(B_0 + B_{spins} + \Delta B) \tag{1.1}$$

Where $\gamma$ is the gyromagnetic constant, specific for each element; $B_0$ is the static magnetic field, and $B_{spins}$ is the spin-spin interaction, which depends on the distance and amount of spins in the region. Moreover, $\Delta B$ is the magnetic field distortion caused by the heterogeneity of the body composition, the presence in ferromagnetic atoms/molecules, and microscopic scale changes in permeability of the tissues. The spin-spin interaction causes spins dephasing, and consequently the tangential magnetization relaxation. The magnetic field distortion introduces an additional time constant, $T_2^\star$, bigger than $T_2^\star$, when considered. All the relaxation phenomena are drawn as exponentially decaying.

Depending on the sequence of RF and Gradient fields, different interactions between spins can be induced, and detected. Each body region contains a different concentration of the excited element, H, which causes the basic proton density contrast. This is further modified by different relaxation coefficients, which characterizes the *MRI contrast map*. The type of the MRI image depends on which weighting coefficient, the relaxation time constant, is used to weight the signal.

### Diffusion Tensor Imaging, DTI

Diffusion tensor imaging is a particular MRI sequence that allows to measure the *diffusion coefficient* of water molecules in different brain regions. The diffusion mechanism is described by the following equation:

$$J = -D\Delta C \tag{1.2}$$

where the current of water molecules, J, is driven by a difference in concentration between two areas, and flows in the opposite direction. The constant of proportionality is the *diffusion coefficient, D*, characteristic for each substance. Diffusion can either be free, developed uniformly along every direction, or it can be constrained by external hindrances. For example, myelin sheaths hinder free diffusion in the axon's radial direction. This type of diffusion is defined as anisotropic, figure 1.20.

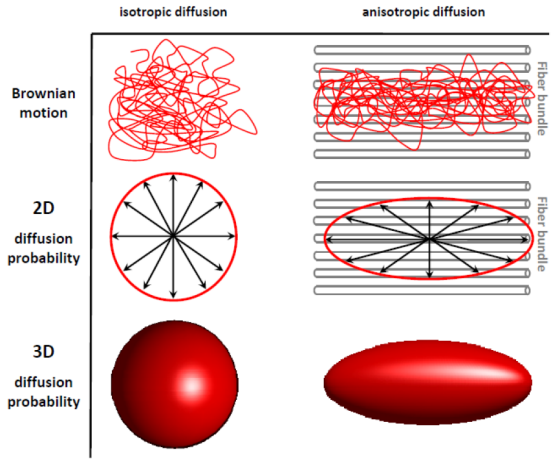


**Figure 1.20:** This figure presents different diffusion conditions which result in either isotropic or anisotropic diffusion. For each row, the diffusion is analyzed at first in 1D, then in 2D and last in 3D.

The MRI sequence used to measure the water diffusion is shown in figure 1.21.

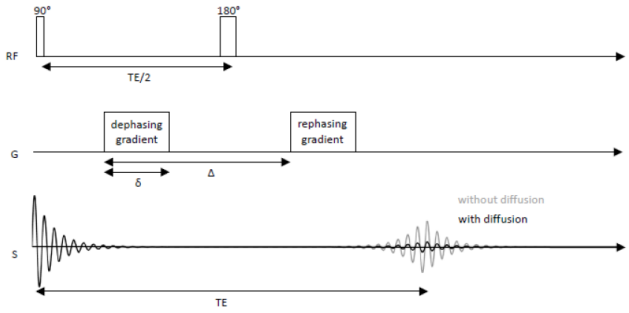


**Figure 1.21:** MRI sequence implemented in DTI measurements.

When acquiring DTI, at first, a simple MRI is measured, by applying only the RF pulse; this image is called $b = 0$. Afterwards, a strong gradient field is applied, for different scans in different directions. In this way, all the water molecules are subjected to the first dephasing field, and the second rephasing field acts to recompose the ECHO signal, after applying the RF 180° field. However, the further a molecule traveled, the less it is rephased, and the weaker the detected signal. The $T_2^\star$ signal related to the molecules' movement, is detected in different directions. Eventually, a combination of the $b = 0$ image and the following scans is computed, and the relationship is proposed in figure 1.22.

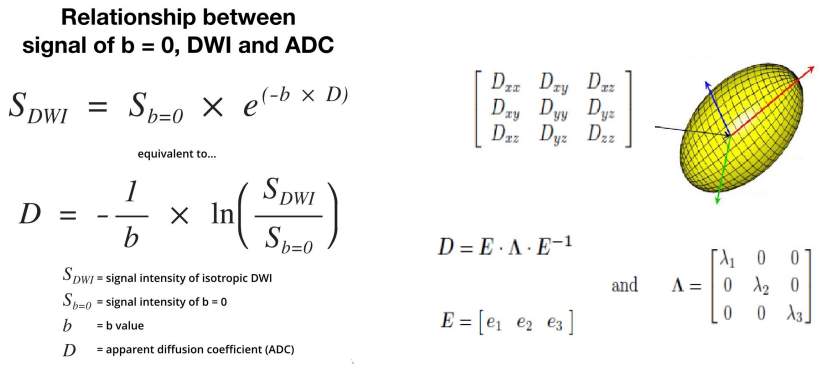


**Figure 1.22:** On the left, the measured DWI signal, and how the diffusion coefficient can be extracted. On the left D, diffusion tensor and its diagonalization are proposed.

**D** is the apparent diffusion coefficient, and **b** is a parameter defining the diffusion weighted strength. First, a few considerations on D follow. This is a 3D tensor, which results to be symmetrical, due to the limitation in measuring the verse of molecules motion direction. The diagonalization of this tensor describes the diffusion process in a single voxel. As shown in figure 1.22, each voxel can be modeled as a 3D ellispoide, and its orientation and eccentricity are related to the diffusion coefficients. The highest eigenvalue is related to the eigenvector along which the diffusion occurs most probably.

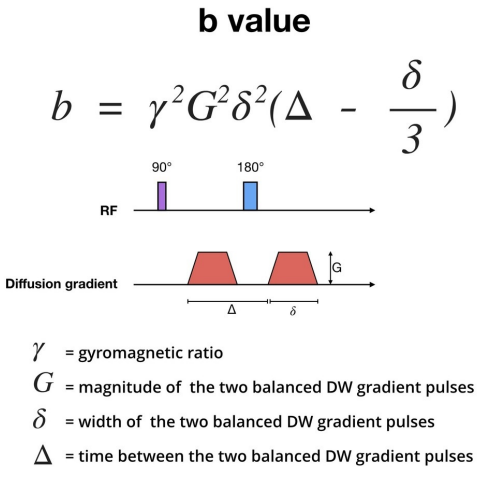


**Figure 1.23:** The b-value is expressed in function of the quantity on which it depends.

Considering the b-value, this is a technical parameter, and its computation is described in figure 1.23. It depends on the amplitude of the gradient field, the time of exposure, and the time gap between the two gradient fields. The highest it is, the strongest the diffusion effect measured. Together with the voxel size, the b-value affects the *signal to noise ratio, SNR*[29]. Therefore, an optimal combination of these two parameters is required for a good signal quality, for a proper investigation of the considered anatomy, and to define reasonable hardware requirements and scanning time[30]. DTI is a technique with several pitfalls. These limitations concern the strong sensitivity to motion artifacts, and the blurring effect due to $T_2^*$ weighting[30, 31]. Another important limitation regards the spatial resolution: the voxel size does not reach the molecular level, and the diffusion process is observed at the fibers bundles scale. However, this flaw respects the feasibility of the investigation. In fact, it would result impossible to manage the huge amount of information acquired by a microscopical investigation of the diffusion coefficient[31, 32].

**Tractography**

Tractography is an implemented algorithm that aims at extracting the *white matter tracks map* from a diffusion weighted image. White matter tracts are composed of bundles of neuronal axons that are arranged in parallel to transfer information from one region to the connected one[31]. There are different algorithms to perform a tractography, however the most commonly used are *deterministic* and *probabilistic* tractography. Despite the differences, a tractography algorithms is generally composed of the following parts[31]:

- *Track Propagation.* This building block characterizes the difference between deterministic and probabilistic tractography. Considering the deterministic tractography, the diffusion tensor is extracted for each voxel composing a tract, and the eigenvector related to the biggest eigenvalue identifies the main direction of flowing. This information can be extracted along the tract step by step, and the information between two steps can be inferred by neighbor-interpolation. Both the interpolation and the step-width definition can vary, considering different algorithms. As far as the probabilistic tractography is considered, the track propagation is not based on the tensor model, instead, it is identified through a probabilistic analysis of Monte Carlo simulations.
- *Seed Points*: definition of the starting point of a tract. Most of the times, this is selected manually, or a region of interest is defined, within which all the voxels are identified as seed points. Another technique is called "brute-force", in which all voxels are pointed as seed points. Yet, another option consists in extracting the information from a functional image, and define the regions of interest, ROIs, as those regions which are activated the most.
- *Tract termination.* There are several approaches to determine the terminal point of a tract. One of the mostly used considers a *fat threshold.* The assumption is that grey matter, the terminal point of a tract, contains less fat than white matter, because of the lower amount of myelin. White and grey matter can be segmented from a classic MRI scan, in which GM and WM result in two different colors, depending on the weighting coefficient considered. Another approach concerns the *local angle of curvature.* The angle is measured between the vectors of diffusion direction of two sequential points. Whether the angle is above or below a defined threshold, the following voxel is considered a terminal point or not.

In this work the tractography is computed by *probabilistic approach*[33]. This method provides a probability distribution of the possible directions of diffusion for each voxel; therefore, the result is a set of most likely directions that can be followed. This approach gives the possibility to grow different tracts from a single seed[31, 33].

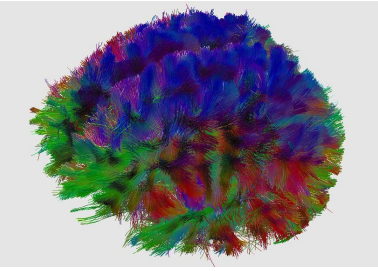

**Figure 1.24:** Whole Brain Tractography.

### 1.3.2 Functional Investigation

This section concerns those techniques employed to detect brain activity. Specifically, the technique described in detail is *magnetoencephalography, MEG.* This is then compared to other functional

investigation techniques, such as *electroencephalography, EEG,* and *functional magnetic resonance imaging, fMRI*, and the advantages and disadvantages of each are addressed[8].

### Brain Activity - The Signal

Brain activity is defined as the simultaneous firing of a defined group of neurons. As a consequence of brain activity in cortical regions, secondary currents are developed extracellularly; for a more detailed explanation of this phenomenon, the reader is sent back to section 1.1.2. Two physical quantities are related to a current: an electrical and a magnetic field. Therefore, neuronal activity develops secondary currents which can be detected at the level of the scalp, by assessing the induced magnetic or electrical field. This allows a *direct* and *non-invasive* measurement of brain activity. As far as the magnetic field is concerned, it diffuses through the skull and scalp without being distorted, despite the discontinuities of the head's tissues and structures. The magnetic field detectable on the scalp origins from pyramidal neurons activity. More specifically, the pyramidal neurons considered are the one located in the sulci, as shown in 1.25. The magnetic field is developed perpendicularly to the running direction of the related current, therefore the detectable field arises from tangential currents with respect to the scalp's surface.

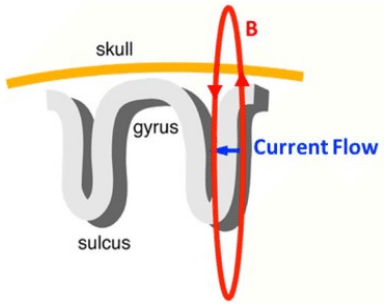


**Figure 1.25:** The magnetic field detectable from the outside is the one resulting from tangential currents.

Concerning a magnetic field, particular attention is given to the signal amplitude and the affecting noise: the signal strength is very small, in the order of magnitude of fT, and it can be distorted and hidden by different physiological and non-physiological noise sources. The most important physiological noises are heartbeat, EMG, eye movements, and motion caused by breathing. Therefore, the subject must lay still during the measurement, and even a small tremor or movement can become source of strong noise. On the other hand, non-physiological noises arise from all the electronic devices and metal objects nearby.

### MEG - Signal Detection

The challenge consists in detecting the described weak and noisy signal, and for this, two aspects must be considered. First, the environment needs to be shielded to reduce the intrusion of external noise, and shielding tactics are implemented throughout hardware and software solutions. Second, very sensitive sensors are required. These factors characterize the biggest drawback in MEG: it is a very expensive technique[8].

In figure 1.26, the general set-up for a MEG measurement is presented. The main block concerns the shielded room, for which magnetically shielding materials are employed, such as Ni-Fe alloys and Aluminum, isolating the room from external magnetic fields; inside, the *Dewar* is shown, the structure containing MEG sensors, and creating the optimal environment for these to work.

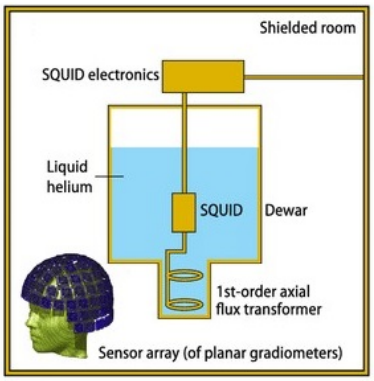


**Figure 1.26:** This picture shows the general scheme of a MEG equipment, and the workflow of a general experiment.

MEG employs specific sensors: the *superconducting quantum interference devices, SQUIDs*. The technology characterizing these sensors is based on superconducting materials. The superconductivity characteristics arise when these sensors are cooled down at their critical temperature, specific for each material, i.e. $9.2K$ for Nb, exploited for this purpose. This temperature is reached by surrounding SQUIDs with liquid He (4 K) or Ni (77 K), contained in the Dewar. These technological aspects contribute to increase the costs.

SQUIDs are defined as converters of magnetic field to electrical voltage. Their structure and working principle are very complex. The steps below try to summarize and display the measurement mechanisms and workflow applied to detect brain activity using a SQUID[10, 8].

1. In figure 1.27, the structure of a SQUID is presented. A SQUID's loop has a diameter of about 0.1 mm, and due to its small dimension, an additional external ring is used to detect the magnetic field, a *pick-up ring*. This has a diameter of 20 mm instead, increasing the field of detection. A pick-up ring can be either a magnetometer or a gradiometer. The first is very sensitive to both deep and shallow sources; however, gradiometers are exploited to delete external noises. The latter ones are composed of two coils arranged in two possible configurations, axial or planar. The detected magnetic field is the gradient between the field acquired by the two coils along the direction characterizing the configuration of the component, figure 1.27.

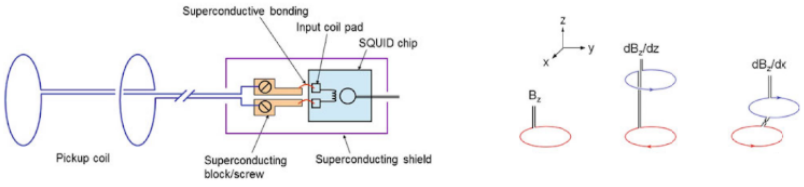


**Figure 1.27:** On the left, a SQUID is shown, where at first the pick-up rings are identified. On the right, the configurations of a magnetometer, and an axial and planar gradiometer are shown.

2. The second step is well pictured in figure 1.28. The magnetic field affects the screening current in the pick-up coil, and a proportional variation of the magnetic flux in the input coil is inferred. This last alter the current running in the SQUID's loop.

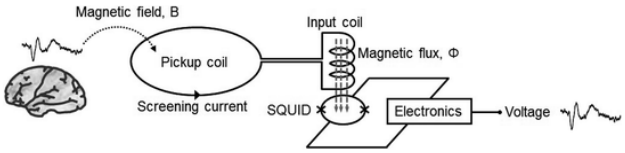


**Figure 1.28:** This figure proposes the design of the conversion process: screening current in the pickup loop, magnetic flux developed in the input coil that is detected by the SQUID's loop, then measurement of the voltage across the Josephson Junctions.

3. A SQUID's loop is characterized by two Josephson's junctions, composed by two thin layers of superconducting materials, separated by a very thin gap of about $30A°$, filled with a very thin non-superconducting material. A bias current, greater than the sum of Josephson's critical currents of the two junctions, is constantly running in this ring, leading to a periodic voltage among the two junctions. This is well displayed in figure 1.29. The magnetic flux period is $\phi_0 = 2.07 \times 10^{15}$ Wb. This last quantity varies when changes in the screening current caused by the detected magnetic field occur. Considering the relationship between voltage and magnetic flux proposed in figure 1.28, changing in magnetic flux are detected by a variation of the output voltage. Eventually, this last measure is the resulting MEG signal.

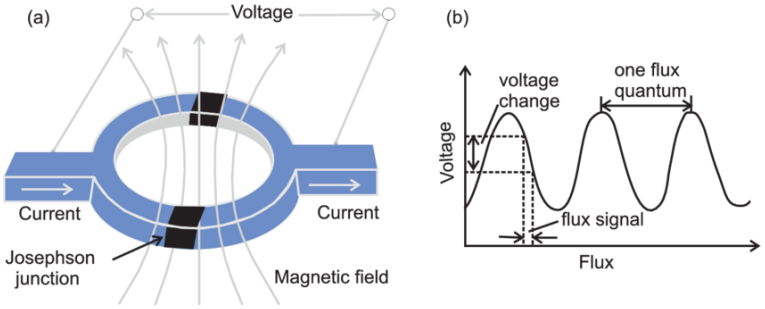


**Figure 1.29:** On the left a SQUID loop is drawn with the two Josephson's junctions (a). On the right, the relationship between magnetic flux and detected voltage is proposed (b).

### Pre-Processing and Source Reconstruction

MEG sensors setup is composed of 306 sensors, among which 102 are magnetometers, 102 planar gradiometers and 102 axial gradiometers[8]. After the signal acquisition, some pre-processing is performed to obtain the MEG dataset employed throughout this thesis.

### First Step: De-Noising

At first, meaningless and noisy components are extracted and discarded from the signals. For instance, ECG, 50 Hz main and EOG are deleted by temporal independent component analysis, ICA, or principle component analysis, PCA. Secondly a visual inspection follows to delete channels or epochs with high variance and artifacts.

### Second Step: Source Reconstruction

This step aims at finding the source distribution of the measured brain activity. The acquired signal is presented in sensor space, and by source reconstruction, the signal is moved to source space. The relationship between sources and sensors is not one to one for different reasons. First, it is not physically and technically feasible to employ as many sensors as number of brain activity sources.

Moreover, due to volume conduction, the activity related to a defined region is detected by different sensors[8]. Therefore, source reconstruction methods allow to associate the detected activity to a defined brain region. To clarify, MEG measurements are able to detect brain activity originating from cortical and sub-cortical regions. However, deeper brain regions activity is not measurable. Despite the existence of different approaches, all the methods require the implementation of two models, the *forward or generative model*, and the *inverse model*, figure 1.30. The forward model aims at creating a model of the brain and possible sources distribution from which the acquired signal could be generated; the inverse model defines the cost function that is optimized to find the optimal solution for the sources distribution.

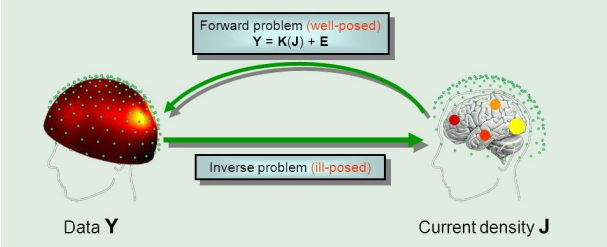


**Figure 1.30:** The general structure of the source reconstruction problem is displayed.

The forward or generative model comprehends the biophysical source model of the brain, and the definition of a source space. Two methods are used to describe the brain activity sources. These are described as current dipoles, or as rigid cubes representing the finite elements of the whole head[10]. The intrinsic spatial resolution of the reconstruction depends on the dimensions or numbers of the finest element, the finite cube or the dipole respectively. MEG spatial resolution is about few $mm^3$. In general, the number of sources modeled is between $10^3$ and $10^6$[10]. To build a whole head model, the head's geometrical and electromagnetic properties are required. These are extracted from an MR image, sometimes combined with a computed tomography image, CT. In order to register this MRI with the MEG sensors distribution, each subjects' head shape is tracked before the measurement. The scalp's shape is recorded with respect to head position indicator, HPI, coils. These last are also used to track small movements during the acquisition. Considering the electromagnetic properties of the head, MEG presents an advantage: magnetic field is not disturbed by brain structural discontinuity and heterogeneity in electrical permeability. Therefore, the head model is simplified[10].

Moving to describe the inverse model, we aim at finding the sources distribution eliciting the measured signal. This is an ill-posed problem, because there are infinite possible sources distributions that can be obtained. However, the problem is confronted by optimizing a cost function that minimizes the difference between the measured MEG and the simulated data, resulting from the forward model. Considering this last observation, two possible approaches are proposed : the equivalent dipole, ECD, and distributed dipoles approach. The former considers a relative small number of dipoles, defining focal sources; the latter counts all the possible source locations simultaneously. The inverse model employed in this work, is a distributed dipoles approach, specifically the *Beamformer* method proposed by Woolrich et Al. 2011[34]. In this model, all the sources must be assumed to be uncorrelated, which means that each source activity is estimated independently. Spatial filters are designed as beamformers, to extract the origin of the measured signal. Advantages of this model are the high focal power, and the absence of a prior assumption on number of sources and location. The beamformer filter is affected by the forward model and the MEG data covariance[34].

### Brain Parcellation and Related Data

After this brief overview on pre-processing and source reconstruction, eventually we define the dataset used to conduct this thesis: this dataset contains as many time series as number of sources,

in source space. As aforementioned, the number of sources can be very big. To cope with this aspect, the data is registered onto a brain parcellation, where the brain is divided into a manageable number of regions. A single time series is assigned to each parcel, and this signal can be inferred by different methods: averaging all the time series gathered in the same parcel, picking the most active source in the region, or applying independent component analysis, ICA, and choose the one with the highest variance. Last step concerns the data *orthogonalization*. Due to volume conduction, MEG measurements are characterized by zero-lag signal overlaps. To discard this effect, orthogonalization is performed to remove the shared signal at zero-lag between parcel's time series[35].

### MEG vs EEG and fMRI

There are two other imaging techniques used to investigate brain functional activity: functional magnetic resonance image, fMRI, and electroencephalography, EEG. fMRI measures the BOLD signal, blood oxygenation level-dependent signal. It is based on the observation that deoxygenated and oxygenated Hemoglobin are respectively paramagnetic, sensitive to external magnetic field, and diamagnetic. Increasing quantity of oxyhemoglobin in a specific region decreases the quantity of deoxyhemoglobin, which in turn changes the local magnetic field. This change is detectable by a particular MRI sequence, fMRI, measuring very fast magnetic field variation, such as the one induced by oxyhemoglobin concentration variation. Changes in oxyhemoglobin are assumed to relate to an increase in neuronal activity, since this requires more ATP consumption, and so, $O_2$ consumption by mitochondria[10]. This very brief explanation shows the *indirect* relationship between the BOLD signal and the real brain activity. Although fMRI has better spatial resolution, low temporal resolution is a significant flaw related to this technique, in comparison with MEG[8]. The second technique considered is EEG. This last is more similar to MEG, since the brain activity is directly assessed[8]. In fact, the signal measured is the electrical signal resulting from secondary currents reaching the scalp. However, electrical signals are distorted by conductivity heterogeneity, and structural discontinuities within the whole head[10]. For these reasons, the spatial resolutions is about 1 cm, whilst MEG spatial resolution is around 1 mm. Furthermore, the head model employed in EEG source reconstruction becomes very complex for the same reason. Another big difference concerns costs, EEG is much cheaper than MEG[8].

# Chapter 2

# Brain Networks

The development of Network Science and the emergent and improved neuroimaging techniques provide new approaches and methodologies to study the complex system of the Brain[36]. In this chapter, we aim at describing the complex and varied Brain Network, its building blocks, and its structural and functional organization. This context of research intends to investigate higher brain functions, such as cognition and behaviour, since these cannot be explained as sum of local activities. Integration and segregation of defined short and long-distance brain regions occur, and the whole brain is found to engage in dynamic systems shaping *Brain Networks*[4, 8, 36].

## 2.1 Brain Connectivity

A Network is generally defined as "a large system consisting of many similar parts that are connected together to allow communication between, and along the parts"[37]. This definition can be employed to examine the brain, both at microscopic and macroscopic scale, where a parallel in network's organization is found[8]. Microscopically, neurons represent either the functional and structural units, among which axons embody their connections. At macroscopic level, grey matter regions are connected by white matter tracks[3]. As mentioned, higher brain functions involve segregated regions mapped over the whole cortex. Therefore, these domains are investigated with a macroscopic perspective, and a *Whole Brain Network model* is defined. This approach allows to focus on long-distance brain regions communication, the arising functional networks, and their role in human behavior and cognition[4, 8, 25].

### Network Analysis

In the late 20th century, Network Science became very popular, since it was able to explain and investigate a broad variety of empirical phenomena. Network science places its roots in the general, and yet powerful, Graph Theory, a study field modelling any set of nodes and their connections as a Network[3]. Watts and Strogatz were the first to apply network model to a simple nervous system, the C. Elegans. This was possible given the reduced dimensions of the system in analysis, composed of only 302 neurons[3]. In the human brain, instead, there are about $10^{10}$ neurons, with a large variety in morphology, but consistent in structure and related functionality. These are connected between each other, by $10^{14}$ links[26]. The huge dimension and complexity of the brain network at the neuronal level, and the technical limitations in acquiring data at microscopic scale, make the analysis computationally very demanding. Therefore, a macroscopic approach is employed[31]. In figure 2.1, the building blocks of a network are shown.

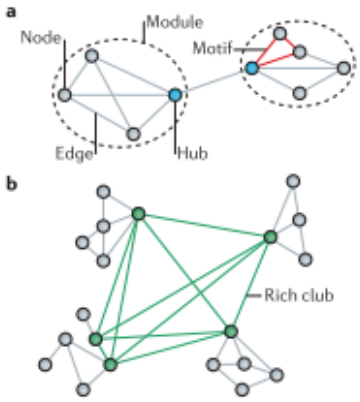


**Figure 2.1:** In this figure, the components of a network in graph theory are shown: **a)** building units of a network, edge, link, node, hub and module, **b)** a characteristic aggregation of elements in a network, the rich club[3].

In Graph Theory, specific networks' architectures are defined, to understand a network's structure and its functional implications. Brain Networks is found to embody the following organizations[3, 4, 36]:

- *Small-World Architecture*: the network is characterized by clusters connected through hub nodes. Therefore, the local connectedness is high when short paths are considered in a module, and efficient long-distance connections are exploited by short paths lengths. This arrangement is shown in figure 2.1.
- *Scale-free Network*: given a node, the probability that it shows k connections (degree k), is inversely proportional to k itself.
- *Hierarchical Modularity architecture*: each network component contains sub-components, and simultaneously, it is part of a higher level component as well.
- *Rich Clubness*: this is an architecture where network hubs are highly interconnected. A hub is a node with high centrality, having an important role in the network connectivity for adjacent nodes, figure 2.1.

Brain Network organization arises during development, and it is well-known to be genetically regulated. Although in some studies the topology results to be slightly different between males to females, this statement is not yet confirmed[38]. Conversely, aging is known to be associated with network changes[3]. The brain network organization is an optimal strategy to minimize wiring costs and to ease the information flow by segregation and integration of brain areas[3].

The presented networks' architectures are found in both structural and functional brain's organization. Brain structural network is found to drive functional interactions, however, some functional patterns do not show underlying direct structural connections[36, 39, 40]. This observation exemplifies the complexity of brain structural and functional networks, and their relationship. Therefore, other study fields included in Network Analysis are employed to face this aspect: *Statistical Mechanics* and *Dynamical Systems Theory*, in which information flow processes within complex systems are studied. These fields provide theoretical and mathematical tools to study brain networks topology and the arising dynamical states, addressed as functional networks. Here, the biggest strength of Network Analysis is carried out: the relationship between calculus and dynamics, whereby any complex physical phenomenon, and its dynamics, can be described mathematically[3]. This approach is a huge step towards understanding biological and physiological systems from the inside, with a bottom-up approach[41]. This is different from the classic

top-down method employed in classic experiments, allowing also to study phenomena for which investigation techniques are not yet developed[41].

Concerning functional networks, the mentioned networks' architectures are found to play a crucial role in cognitive processes. For instance, rich clubs are very important in long-distance interactions, which characterize cognition. Moreover, their hubs seem to represent vulnerable spots in neurodegenerative diseases[36, 42]. Network Science is utilized in neurological disease to track network's damages. This is a promising approach to develop a new *biomarker*: a feature that can be related to diseases' effects or traits. This must be objective, reliable, and reproducible, in order to earn clinical validity[14]. A new biomarker for a pathological condition might lead to early diagnosis or suggest a more efficient approach in treatment plans, by assessing the single subject's condition without referring to a more general class[14]. A new biomarker can be inferred from either functional and structural investigations, therefore assessing neurophysiological or neuroanatomical aspects respectively. As previously mentioned, structural and functional networks are not totally dependent, therefore functional biomarkers can add additional or independent information with respect to the structural ones[40]. Structural and Functional Connectivity, SC and FC, are gaining popularity as biomarkers in assessing brain networks. Recently, these are found to relate with diseases progression and disruptions, moreover the computational ease allows the employment of these features in different fields. To date, an overview on network science is present and the complexity of functional and structural networks is pointed out. Following, functional and structural networks are explained singularly, and the connectivity measures are proposed. Afterwards, the relationship between functional and structural networks is investigated.

### 2.1.1 Structural Network

In this section the Structural Network is described, and the neuroanatomical feature of interest is the *Structural Connectivity, SC*. Recently, a big project, the *Human Connectome*, aims at detecting all the neural connections in the human brain, composing the map of the human brain network[26]. This last is observed from a structural point of view, therefore it is defined as the network of fixed anatomical connections between segregated brain regions. This organization is supposed to remain invariant over a relatively short time scale, for which changes related to aging, learning or neural growth are not observable[4, 36]. Moreover, inter-subjects variability of brain anatomical structure is not taken in consideration in this discussion.
In graph theory, network's connections can either be weighted or unweighted. This last case concerns networks in which a link can be either present or absent. On the other hand, weighted networks have a specific weight assigned to each link[3]. The brain network is a weighted model, in which each link's weight is related to the number of white matter tracts connecting two regions. The description of this weighted network is contained into the Structural Connectivity matrix. This is defined as a squared symmetric matrix in which the dimension is the number of defined brain regions, and each element reflects the strength of connection between a pair of nodes. This matrix results by the combination of *Brain Parcellation* and *Tractography*.

#### Brain Parcellation

The brain's cortex is subdivided into delimited regions, which are thought to be functionally segregated. Several anatomical templates to parcel the whole brain are presented in the literature: the Brain Parcellation Atlases. The subdivision can be very detailed, and a very fine scale of parcels can be inferred, delimiting 241, 483 or even 998 regions, such as the atlas created by Hagmann et Al. (2007)[26]. On the other hand, less detailed parcellations at the hemisphere or lobe level are used for a more general functional brain association study. To determine what is the best choice, the type of acquired data, the goal of the analysis, and the choices made in pivotal studies must be considered. The most common parcellation atlas is the *automated anatomical labelling, AAL*, elicited from a high-resolution MRI of a healthy subject from the Montreal Neurological Institute, MNI[25, 43]. The cortex and subcortex are parcelled into 90 regions, 45 for each hemisphere.

From the parcellation, the distance matrix is computed: a $90x90$ symmetric matrix whose elements measure the distance, as a straight line, between each pair of regions.

#### Tractography

Last step consists in quantifying the amount of white matter connecting two regions, and therefore weighting the strength of each link. This information is extracted from the tractography, a technique explained in section 1.3.1.

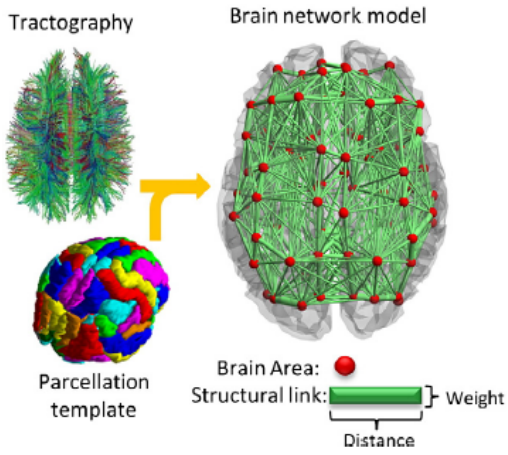


**Figure 2.2:** In figure the structural Network built by Tractography and Parcellation data is presented. Each link is defined by the distance between two regions and weighted by the amount of white matter between the same[4].

First, the number of fibers passing through two voxels, i and j, is quantified, and this information is inferred by tractography. Applying the probabilistic tractography algorithm, the probability distribution of a certain number of fibers passing through each of the selected voxels is computed[31, 33]. Afterwards, the connectivity probability is evaluated by the proportion of the computed number of fibers passing through voxel $i$ and voxel $j$. This calculation is then applied at the region-level, and the number of fibers passing through region $p$ and $n$ is the number of fibers connecting any voxel in region $n$ with any voxel in region $p$[44]. The number of fibers depends on the selected seed point while performing tractography, therefore the computed connectivity between region $n$ and region $p$ can slightly vary from the connectivity between region $p$ and $n$. However, these quantities result to be positively correlated, and the average among the two is defined to be the Connectivity Coefficient between two regions, $C_{np}$[5, 45]. This is how each element of the SC matrix is inferred.

### 2.1.2 Functional Network

In this section, the focus is moved to investigate the functional networks. These describe dynamical processes involving segregated brain regions. Functional patterns can be reconstructed by estimating the statistical interdependence between pairs of time series[36]. As mentioned in the previous section, the network investigation is performed macroscopically, at the system level. Here, the purpose is to study the mechanisms of coherent functional systems formation, and their effects on human behaviour and cognition[8].

To examine functional systems, two quantities are inferred: Functional Connectivity, FC, and Effective Connectivity, EC. The former considers simply the existence of a statistical interdependence

between brain regions activity, whilst the latter aims at finding a direct causal influence of one region activity onto another[36, 8]. In this thesis only FC is discussed; however, one is reminded that FC provides a limited insight in the process, and EC would exploit a better approach. FC limitations depend on the method employed to compute it, and this is sensitive to small variations of the experimental workflow that can affect the signal to noise ratio, SNR. In fields such as data prediction or classification, this can result in increasing of false positives detection, yielding to misinterpretations. Nevertheless, EC is still in a validation phase, and not yet widely utilized[8]. In the following table 2.1, several possible measurements exploited to extract either functional or effective connectivity are presented.

| | Directed Interactions | Freq/Time domain | Multi/Bivarate | Linear | Sensitive to Field Spread |
|---|---|---|---|---|---|
| Amplitude Envelope Correlation | No | F | B | Yes | Yes |
| Coherence | No | F | B | Yes | Yes |
| Cross-Correlations Function | No | T | B | Yes | Yes |
| Cross-Frequency function | No | F | B | No | Yes |
| Directed Transfer Function | Yes | T | M | Yes | Yes |
| Dynamic Casual Modelling | Yes | F/T | M | No | Yes |
| Granger Causality | Yes | F/T | B | Yes | Yes |
| Imaginary part of coherency | Yes | F | M | No | No |
| Mutual Information | No | F/T | B | No | Yes |
| Partial Directed Coherence | Yes | F | M | Yes | Yes |
| Phase Lag Index | No | F | B | No | No |
| Phase Locking Value | Yes | F | B | No | Yes |
| Phase Slope Index | Yes | F | B | No | No |
| Synchronization Likelihood | Yes | T | B | No | No |
| Transfer Entropy | Yes | F/T | B | No | No |

**Table 2.1:** Overview on different connectivity measures and their main characteristics[8].

Before introducing the quantity employed throughout this work, some considerations are proposed. When computing Functional Connectivity, the sought statistical interdependence is defined with respect to a specific quantity, such as the amplitude, or phase. Depending on the addressed quantity, there are several measurements that can be employed, focusing on different aspects and approaching the analysis from different points of view. For example, there are linear and non linear approaches, in time or frequency domain, etc, as shown in table 2.1[8]. In this work, the Pearson's Correlation Coefficient of power envelopes is the quantity employed, and it is computed between time courses of each pair of brain regions. Despite its computational ease, the methods presents some drawbacks: Pearson's correlation coefficient is a sensitive measurement and it decreases with increasing standard deviation, therefore with increasing SNR[26].

### Computation of Functional Connectivity

Given a set of time courses, the below steps present the workflow to extract the Functional Connectivity Matrix.

1. Filtering each time series in the frequency band of interest;
2. Extraction of the amplitude envelope of each signal by the computation of the *Hilbert Transformation*. This last describes the signal in time domain as a rotating vector with an instantaneous phase, $\phi(t)$, and an instantaneous amplitude, $A(t)$:

$$s(t) = A(t)cos(\phi(t)) \tag{2.1}$$

3. The slow amplitude envelope fluctuations, $< 0.1$Hz, are the components of interest, because these contain information regarding brain region coupling, as shown in figure 2.3.

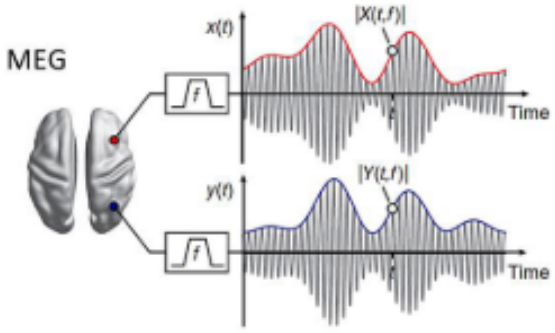


**Figure 2.3:** This figure exemplify the steps that allow to extract the Amplitude Envelopes of two MEG signals related to defined brain regions.

4. The Pearson's correlation coefficient is computed between pairs of amplitude envelope fluctuations. Therefore, Functional Connectivity matrix has the dimension $NxN$, where $N$ is the number of time courses considered, consistently with the number of brain's parcels. Moreover, this approach yields to a symmetric matrix, because Pearson's correlation coefficient is not able to assess the causality of the interactions[8]. In figure 2.4, a FC matrix is present, for each frequency band in which time courses have been filtered in.

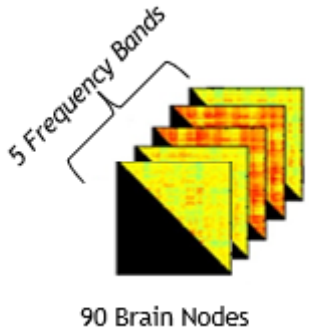


**Figure 2.4:** This figure presents a set of FC matrices, one for each filtering frequency band[5].

### Functional Connectivity Description

Functional networks address all the possible dynamic states detected in brain activity, and their roles in both healthy and pathological cases. Functional brain networks arise from brain regions' synchronization. This last is defined as a mechanism of functional integration between regions, and a long-distance communication process; in addition to this, oscillations synchronization can act as a way of mutual modulating activity[8]. In parallel with these observations, the mechanisms underlying synchronization are considered. This long-distance communication might be driven by common factors that influence contemporaneously all the synchronized regions, or by direct and indirect structural connections[36].

Considering functional networks, in addition to the time window of observation, the paradigm used for the experiment must be defined[4]. At first, the paradigm is considered. Depending on the goal of the experiment, a different paradigm determines the possible dynamical states that the brain network can engage. This is important when there is a target brain region to investigate, as the paradigm concerns a task that allows the activation of the brain region of interest. However, during the last two decades, resting-state measurements gained popularity, since this condition shows brain activity features that are not shown elsewhere[26]. The second factor concerns the time window of analysis. When a task-related paradigm is judged, the time frame of analysis is

dictated by the timing of the task itself. On the contrary, it is important to define the time scale of observation when a resting-state measurement is executed. The time window determines the perspective of the analysis; when a stationary condition is assumed, signals are correlated along the whole recording time. Eventually a single and temporally invariant functional network is extracted, describing a general dynamical state of the brain. This approach is useful to compare FC with SC and to validate computational models.[4] In this dissertation, a stationary approach is employed, in agreement with this last statement. The second approach considers a very short time window of analysis; it is shown that during resting-state different functional networks alternatively arise and dissolve, with a time window of $100 - 200$ms[4]. This is a possible future direction of investigation.

### Resting-State Networks

*Rest* is a condition in which the subject is awake and conscious but is not engaged in any specific cognitive or motor task. In 1929, Berger performed the first EEG during resting-state condition, measuring a brain activity that showed slow spatio-temporally organized neural activities[8]. This observation introduces a challenge in some task-related analyses which might need to be compared to a base-line activity. The problem arises whereby this base-line, resting-state, is unknown and unpredictable[4]. Therefore, this condition is investigated independently, to understand its unknown characteristic dynamics.

Different functional networks are detected during resting-states, the Resting-State Networks (RSNs), shown in figure 2.5. Brain activity during this condition is characterized by alternating activation and deactivation of functional networks. These mostly involve the activation of brain regions which are synchronized also when a task is performed, and for the reason, they are addressed as task-positive RSNs. A particular RSN defined as Default Mode Network, DMN, concerns the activation of regions which are more functionally connected during resting-state than during tasks, and this topology is addressed as task-negative. This network characterizes resting-state activity, and it involves regions usually related to cognitive processes, such as memory, vision, language, etc[24]. From a different perspective, resting-state is described as a condition of indirect wakefulness, in which our mind is ready to engage any possible task. Therefore, it can show different dynamic states, being ready to fully engage one, when an external stimulus occurs[8].

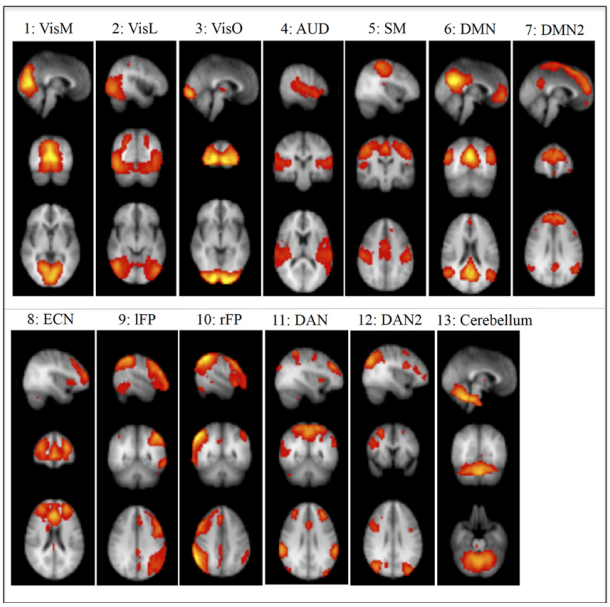


**Figure 2.5:** In this figure the Resting-State Networks acquired by MEG are identified.

### 2.1.3 Resting-State Activity

In general, brain activity is detected in a wide rage of frequencies, from $< 0.1$Hz to 600Hz. Brain activity during resting-state, is particularly detected at low frequencies, and the characteristics rhythms are conventionally split in the following frequency bands: $\delta(1-4Hz)$, $\theta(4-8Hz)$, $\alpha(8-13Hz)$, $\beta(13-30Hz)$, $\gamma(30-48Hz)$, and high $\gamma(52-80Hz)$. Dynamic networks are developed by synchronization of envelope amplitude fluctuations at low frequencies $< 0.1$Hz, related to brain regions whose activity is displayed in the same frequency band[46]. These synchronization patterns describe spatio-temporal organized functional networks. These last alternately activate and dissolve, involving short or long-distance brain regions, but never the whole brain network[4]. This characteristic behaviour is defined as *Chimera-regime*, or *Metastability*[47]. This dynamics discloses brain regions' tendencies to express their specific functionality (segregation tendency), and contemporaneously, to couple and coordinate global functions (integration and modulatory tendencies)[47]. This dynamic regime is fundamental to coordinate brain cognitive, behaviour and social functions[47]. The challenge in investigating Metastability relies on the difficulty to incorporate both spatial and temporal dimensions in a single experimental or theoretical framework[47].

Another characteristics concerning resting-state frequency content concerns the high activity detected in the $\alpha$ band. More in detail, a power $\alpha$ peak, the 10Hz peak, characterizes resting-state brain activity. This parameter has an inter-subjects variability and it is correlated with age[48]. In addition to this rhythm, electrophysiological measurements acquire high resting-state activity also in the $\gamma$ band[8]. The mechanisms underlying these rhythms are different, as well as the role that they cover. Regarding this last aspect, high frequency oscillations seem to coordinate local communication, while long distance communication is yielded by $\alpha/\beta$ oscillations, consistently with MEG and BOLD measurements that detect a decreased collective frequency when defined brain regions synchronize[5, 49]. Oscillations in the $\alpha$ band are shown to correspond to talamo-cortical communication, and this network dynamics has an important role in cognition and perception[8]. Consistently with this last statement, power $\alpha$ peaks are found to correlated with cognitive performance and traits[48, 50]. Therefore, it is of interest to assess this factor when a neurological disease entailing cognitive impairment is investigated. Resting-state condition has initially been investigated by fMRI, and oscillations in BOLD signals were detected at first. Recently, MEG has been employed to investigate this condition, and MEG findings on resting-state activity are consistent with the one gathered by fMRI measurements. The introduction of MEG measurements carries new opportunities in investigating resting-state in multiple temporal and spatial scale, considering its high spatio-temporal resolution[8, 46].

#### Resting-State Network in MS

As introduced in chapter 1, the neurological disease considered along this thesis is Multiple Sclerosis. This pathology yields both structural and functional network disruptions, due to the interplaying mechanisms of demyelination, neurodegeneration, and inflammation[24]. This section aims at discussing functional networks disruption in MS. For this purpose, two aspects are proposed: the $\alpha$-peaks, and functional connectivity disruption.

Starting to consider the power $\alpha$-peak, as aforementioned, this trait correlates with cognitive domains. Consistently, a disruption of this feature is elicited in patients affected by neurological diseases, in which a common pattern of slowed oscillatory activity is detected[6]. As such, this phenomenon is observed also in Multiple Sclerosis, where cognitive impairment is found to correlate with a shift of the $\alpha$ peak towards decreased frequencies[6, 51], as shown in figure 2.6.

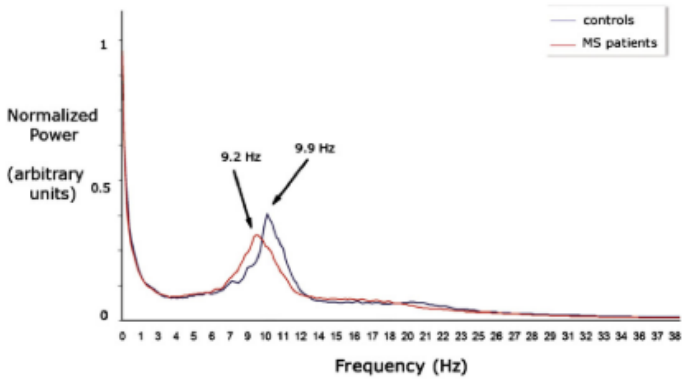


**Figure 2.6:** This plot shows the $\alpha$-peaks in healthy condition and in early MS. It is noticed the shift towards low frequency detected in the pathological condition[6].

Following, the discussion considers the FC disruption. In the past few years, many studies have addressed the FC networks disruption in MS, based on either MEG or fMRI acquisitions. Among all the results, the first important observation concerns the impact of a lesion. This last can affect not only functions overseen by the damaged region itself, but also those driven by functional networks which the disrupted region belongs to[24]. The focus is pointed at the DMN network, involving brain regions related to cognitive domains. Cognitive impairment is diagnosed in a consistent part of the MS population in early stages, and it follows the disease progression. Therefore, studying DMN and resting-state functional networks disruption in Multiple Sclerosis is one of the approaches that are used to assess cognitive impairment. A positive correlation between cognitive impairment and increasing FC in MS is detected mostly in early stages of the disease, whereas decreasing FC is observed later along the disease progression[14, 52]. The mechanism underlying this phenomenon is sought, and different assumptions are proposed. This effect can be either passive, lesion-induced, or active, a brain plasticity mechanism that tries to balance the damage caused by the disease. Many researches suggest the occurrence of active processes of compensation, related to the plastic capability of the brain. Nevertheless, these mechanisms are subject-related, and depend on the region where the damage occurs[24]. Another observation is the following. FC variations are observed to be either *positive adaptations*, or *maladaptations*. In the former case, the brain is noticed to dislocate the damaged domains in different areas, in order to preserve the function. Conversely, maladaptation refers to the increasing activity of certain areas induced by the incapability of switching to different stages[24, 14]. In this last scenario, higher local connectivity hides long-distance connections damages[52].

There is no correct or wrong interpretation of the phenomenon, and both the mechanisms explained are present. Structural and functional networks disruptions are not totally independent, but the relationship is not straight forward, and several factors interplay. Functional damages depend on the addressed region, the involved functional networks, and the spread of the damage[52]. In general, functional disruptions better follow disease progression than structural damages[52]. However, this filed is yet to be investigated, and promising features can be elicited to assess the pathology.

### 2.1.4 Relationship between SC and FC

One of the most interesting challenges in brain connectivity studies consists in eliciting the relationship between SC and FC; how functional networks arise with respect to the underlying structural connections. However, there are no investigation techniques that allow to detect the mechanisms of arising functional networks[36]. Considering different observations proposed in the literature, structural connections are always found to guide functional interactions. However, functional networks, are not always carried by underlying structural connections, and a different approach is

employed to investigate this context, by using graph theory descriptors. For instance, it is elicited that the probability of arising of a functional network is directly proportional to the degree product of the involved regions[39, 40]. Another study proposes the difference between FC and EC with respect to SC, for which FC would resemble SC in most cases, whereas EC does not; however, concerning EC, a relationship between the connectivity weight and the structural degree product is obtained, in both connected and non-connected regions[36].

Despite the findings and observations, an intrinsic limitation concerns the impossibility to investigate combined functional and structural dimensions, by only considering neuroimaging investigations. Therefore, a different approach is implemented, and the employment of a neurocomputational model is considered. This method is utilized by many studies, since it allows to simulate brain activity, given in input a defined structural brain network. A model defines a scenario that describes brain regions dynamics. The elicited simulated FC is correlated with the empirical FC to verify the model's performances, and information on the relationship between SC and FC can be inferred[26, 39]. This topic is discussed in detail in the following chapter.

# Chapter 3

# Neurocomputational Models

In the previous chapter, it is presented the idea underneath the *Multi-Modal Human Connectome Project*, *HCP*. This aims at characterizing the pathways underlying human brain functions[7]. However, the presence of different techniques to assess human brain investigation introduces a challenge in building this collection. By employing neuroimaging techniques such as MRI, only the anatomical brain network is investigated, as presented in the previous chapter. On the other hand, MEG and fMRI measurements of resting-state brain activity detect functional brain networks[7], which not always overlap the underlying anatomical connections. Nevertheless, from a static perspective, Functional Connectivity observed in a relatively long timescale resembles the underlying SC[4, 52]. Therefore, starting from the defined anatomical connectome, the investigation aims at going beyond this structural architecture to understand the brain functions resting upon it[7]. Neuroimaging techniques are limited in this perspective, since these allow only to assess either the functional or structural aspect separately; furthermore, the underlying brain activity mechanisms are yet unknown. Therefore, an intermediary that allows to infer functional maps in function of the underlying topological structure is proposed: a neurocomputational model[36].

## 3.1 General Aspects

### 3.1.1 Bottom-Up Approach

The method utilized to conciliate the structural and functional information concerns the employment of a *Biophysical Model*. This approach allows to fuse functional and structural connectivity data, and express their relationship mathematically. As such, the employment of the biophysical model provides a *Bottom-Up* approach[7, 41]: brain activity is simulated by designing a possible scenario that describes the physiological origin of brain activity itself, instead of extrapolating the mechanism from the acquired data.

### 3.1.2 A Biophysical Model: Neurophysiological Realism

The real physiological mechanisms underlying functional networks are yet unknown, as well as their functional roles; however it is possible to define a possible physiological scenario[4]. When picturing a plausible contexts, observations on the real biophysical phenomenon must guide the definition of the model itself. This last must be designed consistently with the context of analysis: the physiological and anatomical characteristics of the system under investigation, *the brain*. Another important aspect is the physics behind the neuroimaging technique employed to acquire empirical data. Each neuroimaging technique has a specific spatio-temporal resolution, and sensitivity to certain physiological signals. The computational model must be consistent with these aspects, in

order to assure the same perspective of analysis[7]. This whole set of considerations stresses on the neurophysiological realism and complexity that must be respected by the designed scenario[7].

## 3.2 Components of a Biophysical Model

A Neurocomputational model is built upon two models: the anatomical model of the brain, the structural network, and the computational model describing the dynamical interactions within and between brain regions. This approach aims at reproducing the spatio-temporally organized functional patterns detected by neuroimaging techniques[7]. The model's performances are investigated by correlating simulated with acquired data[7]. In figure 3.1, the main characteristics of a biophysical models are shown: the brain is partitioned in nodes, and these are structurally connected by direct links. Moreover each node is described by a scenario that mimics the mechanism underlying each node's activity.

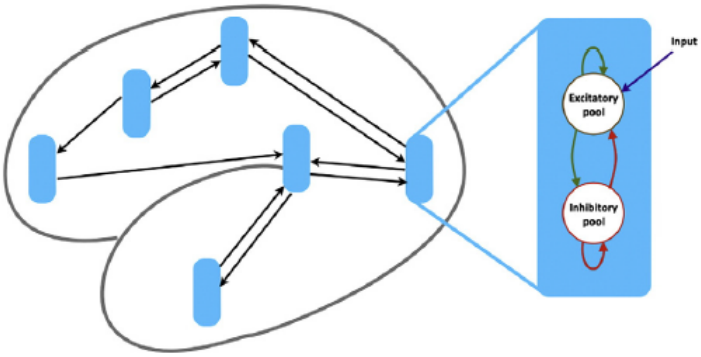


**Figure 3.1:** In this figure the main aspects presented in a biophysical model are shown: the brain in subdivided into regions modeled as nodes, which are structurally connected. Moreover, each node's dynamics is characterized by a biophysical scenario, that defines the mechanism underlying node' activity. In this picture each node is composed of two subpopulations that determines the regional activity[7]. The dynamics of each node depends also on the inputs coming from the environment.

There are different approaches utilized to delineate each node's activity. For instance, realistic models describe the system's dynamics with state variables that are deduced by the physiology of the system, such as the membrane conductance. On the other hand, there are models that approach the dynamic via a mechanistic perspective, such as the Kuramoto Model. The model choice depends on the purpose of the analysis and the aspects under investigation[4, 26].

### 3.2.1 Whole Brain Network Model

As stressed along the whole dissertation, it is very important to define the scale of observation. Although computation of detailed models at the cellular level are becoming feasible, i.e. the *neuronal models*, in this work a *whole Brain Network model* is employed. As far as M/EEG measurements are concerned, direct neural activity is detected with high temporal resolution, at milliseconds scale, the timescale of neuronal dynamic interactions[7]. However, these techniques accomplish high spatial resolution, reaching few mm with MEG. This resolution doesn't allow to acquire single neuron's activity, and an approximation at the population level is pursued: neurons belonging to a dense ensemble are reciprocal interconnected, sharing the same physiological behaviour[26]. Each node of the network represents a population of neurons, modeled as *mean-field* or *neural mass*[8]. This ensemble has an intrinsic characteristic dynamics, and its description depends on the scenario designed by the chosen model. Instead, white matter tracts between two regions characterize the network's links. The structural network is in general provided to the model as input,

the SC matrix. In most of the brain network studies, networks' nodes are described as isolated points in space *point-masses*[26]. However, new and more elaborated networks' models propose to shape each neural population as *neural field*, describing its state in function of both time and position, to include the whole cortical sheet in the analysis[26].

### 3.2.2 Neuronal Population: Dynamic Model

Once the structural network is defined, the second component of a model is presented: the brain regions' dynamics. At this point, we aim at describing neural population's behaviour, characterized by the probability distribution of the neuronal state variables[7, 8, 53]. This last quantity depends on the chosen scenario, and in this dissertation, each mean-field is described as a system of coupled-oscillators[53].

#### Coupled-Oscillators

In many natural systems, the interactions between entities require timing, and occur by synchronization of entity activities. In order to attain a global coherent activity, each entity is characterized by an oscillatory activity, and the quantity introduced to describe each entity's behaviour is the *phase*, a measure of the periodic activity in time[53]. In neuronal populations, each neuron is referred as an entity, and the synchronization of these entities refers to the simultaneous firing of a group of neurons, to accomplish a single function. As such, these populations mimic functionally segregated brain regions.

The oscillatory activity of a population can origin from two biophysical mechanisms. The first one considers each entity's activity evolving regularly in time, and when beyond a certain threshold, a pulse is emitted affecting neighbors' activity. The interaction depends on the neighbors' state, and the synchronization is defined in function of the phase-shift between two entity activities[53]. The second approach refers to a group of entities as an ensemble of *nonlinear coupled oscillators*, belonging to a globally attracting limit cycle of constant amplitude; the entities are coupled to avoid disturbances to disrupt the cycle[53]. This mechanisms can be used to describe the electrophysiological observations at the level of neuronal population[4, 8, 54]. Within each brain region, three neural sub-populations can be identified: excitatory pyramidal neurons, excitatory spiny stellate neurons and inhibitory brain neurons, each with a different firing rate. The global firing rate results from the balancing between the three just mentioned, describing a periodic trajectory. This limit cycle characterizes the intrinsic oscillatory activity of neuronal populations[5, 53]. In figure 3.2, the population dynamics is shown.

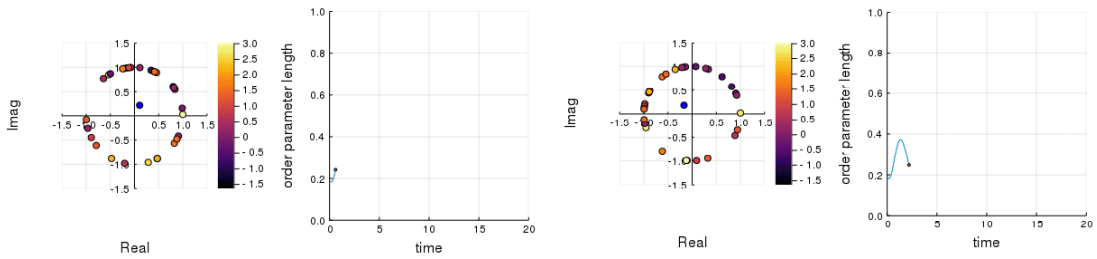


**Figure 3.2:** This figure proposes two time frame of a neuronal population's activity, when it is described as a system of coupled-oscillators. Each oscillator works at a different frequency, and the result is the total phase of the system, the middle point. On the right graphs, the oscillatory activity of the resultant phase is observable.

All the oscillators composing a single neuronal population, are defined as *self-sustained* oscillators. This is an assumption proposed by this specific scenario, that cannot be related to a physiological aspect. Despite this, the described scenario models very well the brain regional activity.

## 3.3 Nodes Interactions: Dynamic Causal Model

The dynamical model of interaction between regions in a network should fulfill the following requirements, with respect to the biophysical realism of the context of investigation[4, 7, 8]:

1. The characteristic trend should be cyclic;
2. Each connection should be reciprocal, bi-directional;
3. The interaction between regions cannot be instantaneous, due to conduction delay.

Given these guidelines, a *Dynamic Causal Model* can be defined. This model is a general expression for brain regions' interactions:

$$\dot{x} = f(x, \theta, u) + _x \tag{3.1}$$

where $\theta$ is the state variable defined by the model, the *phase* in coupled oscillators model; $x$ is $P \mathrm{x} T_x$ matrix of $P$ hidden neuronal states and $T_x$ time points. $\dot{x}$ is the time derivative, $u$ are the unknown external inputs, and $e_x$ the stochastic neuronal noise. In case $e_x = 0$ the equation corresponds to a deterministic case. Moreover, $u = 0$ when resting state condition is investigated[7, 8].

### 3.3.1 Kuramoto Model

In the specific case where each population is described by coupled oscillators, one of the expressions of the dynamic causal model is the one proposed in 1975 by Kuramoto[53]. This model describes each brain region as a system of phase oscillators running at arbitrary intrinsic frequency, and coupled by the sine of their phases difference, with a constant amplitude[53]. This model has been employed successfully in neurological science to model and study brain networks[5, 53, 55]. Despite the fact that this scenario implies a high level of abstraction, since the neuronal state variable is not related to any physiological quantity, this model is mathematically approachable, and dynamically rich enough to be adaptable to different context and to display most of the systems' synchronization patterns[4, 54]. The following equation 3.2 is the expression of the dynamic causal model's general equation 3.1 in case of coupled-oscillators systems, and it shows the dynamic regime for a single entity $n$ of the system:

$$\frac{d\theta_n}{dt} = \omega_n + \sum_{p=1}^{N} K_{np} sin(\theta_p(t) - \theta_n(t)), n = 1, ..., N \tag{3.2}$$

where $\omega_n$ is the intrinsic frequency of the entity, $K_{np}$ is the coupling strength connecting each pair of units related to the structural connection, and $\theta_n$ and $\theta_p$ are the entity phases. The proposed Kuramoto formulation is the most general one. However, in different applications some extensions of the model are introduced, to fulfill requirements related to the context of analysis[53]. In the following sections, specific model's features are shown, as well as variations to assess neurophysiological aspects.

### 3.3.2 Model Characteristics

The following discussion concerns the model parameters that allow the model to respect the neurophysiological and anatomical realism[7]. Three sections are proposed: the first one considers the structural constraints, secondly the introduction of the noise and time delay is discussed, and the last part focuses on the metastability.

### SC Constraints

As stressed at the beginning of the chapter: a biophysical model provides an insight to dynamical mechanisms in function of the structural organization. The Kuramoto model embodies this approach, by strictly constraining the development of functional interactions, to the underlying structural connections[56]. This is expressed in the Kuramoto equation 3.2 by the coupling strength coefficient, $K_{np}$, extrapolated by the network's structural connectivity. This elicits an observation: the development of nodes interactions depends on the resolution and detail level of the considered SC. The quality of the SC and the chosen parcellation affect the model's performance, and therefore, this limits the fitting with empirical data. The more detailed the scale of investigation is, the more relevant this issue becomes. This flaw of the approach could be solved by introducing a generative model for the structural connectome, or by allowing possible variations considering the underlying structure[4, 7].

### Noise and Time Delay

Noise and Time Delay are always considered in a neuro-physical model. Regarding time delay $\tau_{np}$, this quantity relates to a defined pair of regions, $n$ and $p$. It embodies the concept of finite information conduction velocity, $v$, belonging to all the study fields regarding information transmission and information processing. In this specific context, the finite conduction velocity is determined by the distance between two regions, the myelination level of the considered tract, and the slow information transmission in the synaptic cleavages. It is computed as:

$$\tau_{np} = D_{np}/v \tag{3.3}$$

where $v$ is the conduction velocity, and $D_{np}$ the distance between two regions, $n$ and $p$. For simplification, in network model studies the conduction velocity $v$ is considered homogeneous for all the connections, and time delay is also considered uniform over the whole brain network: $\tilde{\tau} = \tilde{D}/v$, where $\tilde{D}$ is the average of the distance matrix.

Moving to consider the second factor, the noise, $\psi_n$, refers to the stochastic neuronal noise resulting from neighboring activity. Most of the brain network models require this factor to induce transition among available dynamic patterns. The following equation 3.4 proposes the adjustment of the general Kuramoto, considering the factors just described:

$$\frac{d\theta_n}{dt} = \omega_n + k\sum_{p=1}^{N} K_{np} sin(\theta_p(t-\tau_{np}) - \theta_n(t)) + \psi_n, n = 1, ..., N \tag{3.4}$$

The effect of noise and time delay on brain dynamics depends on the model chosen to describe the local dynamic neural activity. Regarding the Kuramoto model, it is observed that both noise and time delay prevent global system synchronization by preserving phase heterogeneity. Time delay results very important when its scale has the same order of magnitude of the oscillatory timescale[44]. This parameter is also shown to affect global dynamics, playing a role in shaping spatio-temporal connectivity patterns, and reducing mean firing rate of synchronized regions[44]. Therefore, the frequency suppression with respect to the intrinsic frequency of each brain region is found to be caused by time delay[4, 44]. Furthermore, specifically in the Kuramoto Model, once time delay is introduced, noise doesn't seem to play a major role anymore, and in many cases it is discarded to simplify the analysis[5, 44]. However, an additional parameter is added: $k$, the global coupling strength, whose role aims at assuring phase interactions[5]. In case where the noise is included, the higher the noise, the stronger k must be, in order to allow phases synchronization[53].

### Metastability and Bifurcational Point

This paragraph discusses the core properties of brain network's dynamical states. As explained in the previous chapter, resting-state brain activity is characterized by activation and dissolution of

different dynamic patterns. From a static perspective, resting-state FC is shaped by the underlying Structural Connectivity. However, it is observed that alternation in dynamical states occur, and that the whole network never fully synchronizes. This condition is defined *Chimera regime*[4]. This reflects the integrative and segregating tendencies characterizing brain activity, optimizing the mechanism of information processing[57]. In order to reproduce this peculiar dynamic regime, a neurocomputational model must work nearby its *Bifurcational Point* when simulating resting-state brain activity[4, 8, 57]. This point represents the critical point of transition between equilibrium and the repertoire of activation patterns available. For the Kuramoto model, this critical point refers to the intrinsic frequency of each brain region, which is set at 40Hz, related to the brain $\gamma$ rhythms[5, 55].

After all these observations, an overview on the brain rhythms displayed by the Kuramoto Model is proposed[4]:

- $\gamma$ oscillations in the intrinsic frequency of brain regions;
- $\alpha$ and $\beta$ rhythms displayed during sub-networks synchronizations:
- Ultra-slow aperiodic envelope fluctuations induced by alternation of dynamical states: chimera regime.

These rhythms are identified in fMRI and MEG resting-state brain activity measurements, explained in section 6.1. Therefore, the Kuramoto model with time delay proves to be a good biophysical model to study brain dynamic resting-state networks.

## 3.4 Neurocomputational Model Applications

Neurocomputational models can be employed to pursue different goals. The most straightforward consists in reproducing empirical data by means of functional network patterns. From this perspective, once correlating simulated and acquired data, the model's optimal parameters are extracted, and these characterize the brain dynamic with the model's dynamic state. Another interesting employment, concerns simulating brain functional networks in neurological disease where the anatomical connectivity is damaged. If the model is able to detect variations in functional networks given the disrupted structural connectivity, an insight in the relationship between functional and structural network disruption is elicited[56]. This aspect is very interesting in pathologies where diagnosis only relies on symptoms and the underlined physiological disruption is unknown. However, an important consideration is proposed: the mechanisms underlying the functional disruption depends on the chosen model. Neurocomputational model implementation is a promising approach also for disease where there is a strong inter-subjects variability. If the model was reliable at the subject level, a new approach in diagnosis and treatment planning would be introduced[4, 7]. However, the feasibility of implementing a model at the subject level is a complex and long process. In this context, the big challenge concerns the model's validation: the model must be able to recognize a certain physiological condition starting from a ground truth. Moreover, the validity must be related to a quantitative measure that can be useful in clinical decision-making.

One last observation on the employment of a neurocomputational model arises from the concept of model itself. First, by definition a model does not describe a phenomenon in all its characteristics; however it shows a possible abstraction and simplification of the investigated mechanisms. Depending on the level of precision required, it can be considered a good approximation or a rough one. In neuroscience, there are several different model describing neuronal dynamic interactions. Each one capturing a different aspect of the mechanism. These are not in competition, but in a collaborative effort to explain the complexity and variety of interplaying mechanisms underlying Brain Functionality[4].

# Chapter 4

# Research Objectives

In Multiple Sclerosis, about 40% to 70% of the patients develop cognitive impairment, CI, and one of the most impaired cognitive domains is the *information processing speed, IPS* [12, 13]. The disruption of this domain is related to a decreased conduction velocity of information transfer, due to demyelination. This is assessed in clinical practice by neuropsychological tests, which, however, present several drawbacks [14]. To overcome this aspect, a more reliable and objective measure is sought, and one approach would concern the extrapolation of a *biomarker*, by the employment of neuroimaging techniques and neurocomputational models. This thesis is developed in this research context; we aim at finding a quantitative measure that can be related to IPS impairment. Within the literature, there are neurophysiological markers, such as Functional Connectivity or the power $\alpha$-peaks, that are found to be altered in MS, and correlated to CI [51, 52]. These quantities are deduced by neuroimaging techniques, whereas in this work, a neurophysiological feature is extrapolated by the implementation of a neurocomputational model. The simulated brain activity is matched with the MEG resting-state data, and the optimal correlation is achieved when the model is set to specific, *optimal*, model parameters. These provide a certain description of the brain's condition in terms of the characteristics tackled by the chosen model. In figure 4.1, we provide and interesting representation of the pipeline that permits to extract the optimal descriptors.

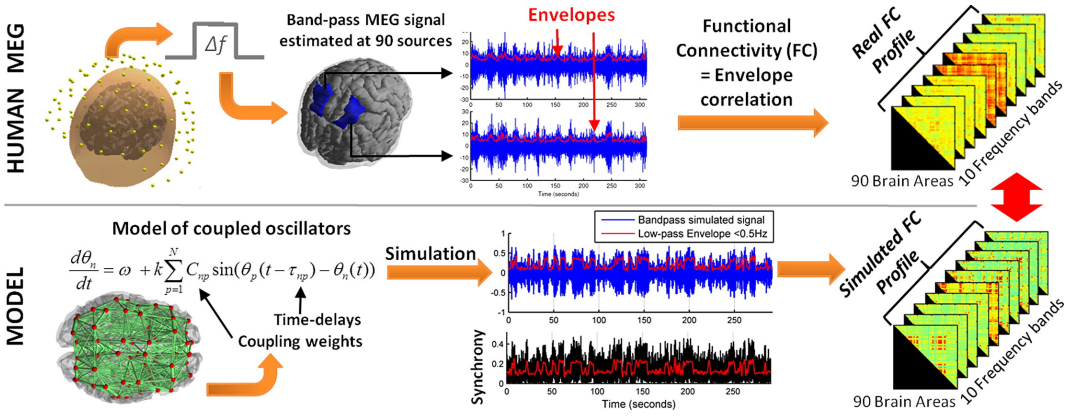


**Figure 4.1:** This figure proposes the workflow followed to extract simulated and empirical FC[4]. This figures is adapted from the correspondent in the reference paper [5]

An additional innovative aspect introduced by this work concerns the implementation of the model at the subject level, to verify the model's capability to capture variation of a physiological process at this scale. To pursue this final investigation, three steps are conducted, and each part of the work is guided by a specific hypothesis. Following, the three research objectives are presented.

## 4.1 Objective I

The neurocomputational model employed along this thesis is a variant of the original Kuramoto Model: the time-delayed coupled oscillators. This has already been successfully implemented in several studies, to simulate resting-state brain activity [5, 55, 57]. For example, Cabral et al. have correlated empirical static Functional Connectivity, FC, obtained by resting-state MEG data, with simulated FC. In particular, a strong correlation is inferred in the $\alpha$ and $\beta$ frequency bands, where resting-state activity shows characteristic power peaks. Moreover, the model was able to recreate the brain network's metastability regime observed in resting-state measurements. Before employing the model to pursue the ultimate goal of this thesis, its performances must be validated, and compared with the literature findings. To conduct this analysis, the following research question is proposed:

**Hypothesis I**: Reproducing the analysis proposed by Cabral et al. 2014a [5] employing the available dataset, the model validation is deduced when consistent results are obtained.

## 4.2 Objective II

After proving the model reliability, the following investigation concerns the analysis of the model performance, when groups of subjects characterized by different health and pathological conditions are considered. The model optimal parameters, k and $\tau$, are inferred whereby the Pearson's correlation coefficient between simulated and empirical FC is the strongest. This combination of parameters is expected to adapt when groups of subjects with different neurological conditions are involved. More specifically, the time delay, $\tau$, is defined in function of the conduction velocity, and the decreasing conduction velocity detected in MS is expected to reflect an increasing time delay in the same condition. As such, the second research hypothesis can be formulated as follows:

**Hypothesis II**: The Kuramoto model performances vary among groups of subjects concerning different neurological conditions, HC, MS and MSB.

## 4.3 Objective III

When the model is found to detect variation between groups of subjects concerning healthy controls and MS patients, the following step of analysis consists in validating the model at the subject level. Starting from a common SC matrix considered as ground truth, the simulated FC is correlated with each subject's empirical FC. Within the literature, different studies examine the alteration of FC in MS [24]. Therefore, the model's parameters related to the strongest FC correlation are expected to vary case by case, depending on the pathological condition presented by the subject. The parameter of interest, time delay, is determined in function of the conduction velocity. In Multiple Sclerosis, CI is associated with disruption of conduction velocity. However, this last is not directly measurable, and an intermediate parameter is required to correlate time delay variations, related to conduction velocity, with IPS impairment. Other physiological traits are affected in MS, such as the power $\alpha$-peak, detected during resting-state measurements. This parameter is found to correlated with cognitive impairment in MS [52]. Therefore, the last hypothesis of research is presented:

**Hypothesis III**: By applying the model at the subject level, the model's parameter time delay varies with respect to the subject-specific pathological condition, correlating to IPS impairment. To detect this adaptation, $\tau$ is correlated with another neurophysiological feature, related to CI. This last is the power $\alpha$-peak, detected in resting-state measurements.

# Chapter 5

# Methods

In this chapter, the analyses conducted throughout this thesis are introduced and explained. Starting from the presentation of the dataset, afterwards, the employed model is described, and its parameters are defined. Furthermore, the statistical analyses are presented. To pursue the investigations, the programming languages used in this thesis are MATLAB and Statistics Toolbox Release 2017b (The MathWorks, Inc., Natick, Massachusetts, United States); and Anaconda environment version 3.1, Python Language Reference.

## 5.1 Dataset Analysis

The original dataset includes 150 subjects, among which there are Healthy Controls and a heterogeneous group of Multiple Sclerosis patients, with different MS typologies, at different disease stages, and treatments plan. The detailed composition of the dataset is presented in the following paragraph. For each subject, the related data includes subjects' structural and functional information, consisting of structural connectivity, SC, and functional connectivity, FC, respectively. In the following sections, the methods to extract SC and FC matrices from the empirical data are explained.

### 5.1.1 Structural Connectivity

Each subject undergoes MRI and DTI measurements for a structural investigation. MR imaging was performed on a 3T Achieva scanner (Philips Medical Systems, Best, The Netherlands). The relevant information, concerns the parameters related to the DTI - sequence: $b = 0$ volume, TR/TE = 8500/65 ms, FOV = $128 \times 128$, voxel resolution: $1.78 \times 1.78 \times 2.2mm^3$, 32 different directions, b-value$_1$ = $800s/mm^2$ and b-value$_2$ = $1000s/mm^2$ after upgrade. Afterwards, tractography is inferred via probabilistic tractography[33], from which the local probability distribution of fibers per voxel is computed, and then extended to the regional level, proceeding as explained in section 2.1.1 [5]. The subject's anatomical MRI is coregistered to the MNI space, and parceled using the automated anatomical labelling atlas, AAL[25, 43]. Brain cortex is parceled in 90 regions, 45 for each hemisphere. Each region is represented by a node, and the distance between each node, considered as a straight line, is computed to infer the *Distance Matrix*, $D$.

The analyses concerning SC matrices, are driven by two motives: findings in the literature concerning differences between groups of SCs, and the employment of the *average SC* as main quantity. This last is affected by outliers, which can mislead data interpretation. Therefore, a careful examination is conducted. At first, subjects' SCs are examined visually, to recognize and discard outliers; in figure 5.1, the difference between a normal SC and an outlier is shown.

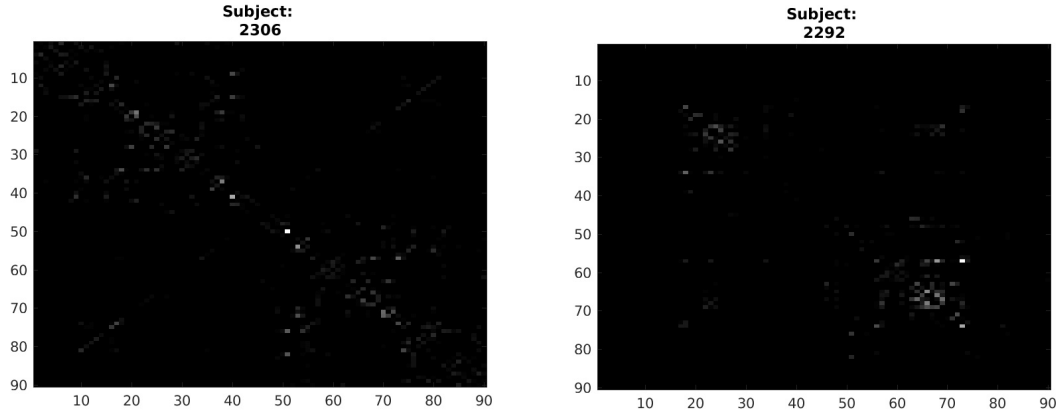


**Figure 5.1:** On the left, a normal SC is displayed; instead, on the right, an outlier SC is present.

Once the dataset is examined, the differences between sub-populations of subjects are investigated. The first comparison concerns two groups of subjects, BRUMEG1 and BRUMEG2, identified by the different scanner's parameter, b-value, that was used during DTIs, as mentioned in the previous paragraph. This b-value reflects the timing and strength of the gradient field used for DTI acquisitions, and it affects the measurement itself, as explained in section 1.3.1 [29]. The compositions of BRUMEG1 and BRUMEG2 datasets are presented in tables 5.1 and 5.2. These tables consider the dataset already visually examined, therefore the total number of subjects results 118. A characteristic that is worth mentioning follows: BRUMEG1 contains only female subjects, whereas BRUMEG2 gathers both male and female subjects. In each dataset, three subgroups are identified, based on the neurological condition: healthy controls, HC, Multiple Sclerosis subjects, MS, and Multiple Sclerosis patients undergoing Benzodiazepine treatment. This last group is analyzed separately, because this drug is found to affect FC with respect to the average MS population, and this might influence the following results.

| **BRUMEG1** | Numer of Subjects |
|---|---|
| HC | 14 |
| MS Benzos Negative-MS | 21 |
| MS Benzos Positive-MSB | 8 |
| Max Age | 69.5 |
| Mean Age | 46.7 |
| Min Age | 27 |

**Table 5.1:** This table shows the composition of dataset BRUMEG1, characterized by b-value= $800 s/mm^2$.

| **BRUMEG2** | **Numer of Subjects** |
|---|---|
| HC | Male 14 |
| | Female 13 |
| MS Benzos Negative-MS | Male 22 |
| | Female 26 |
| MS Benzos Positive-MSB | Male 1 |
| | Female 9 |
| Max Age | 68.9 |
| Mean Age | 47.9 |
| Min Age | 26 |

**Table 5.2:** This table shows the composition of dataset BRUMEG2, characterized by b-value= $1000 s/mm^2$.

Considering the groups of subjects identified in tables 5.1 and 5.2, the following comparisons between SCs are conduceted:

1. BRUMEG1 vs BRUMEG2;
2. BRUMEG1: MS vs HC;
3. BRUMEG1: MSB Benzdiazepine-Positive vs MS Benzdiazepine-Negative vs HC;
4. BRUMEG2: MS vs HC;
5. BRUMEG2: Males vs Females. This comparison is conducted for the whole dataset, and then separately for MS and HC subgroups.

To investigate the presence of a significant difference between two groups of SCs, the following null-hypothesis is formulated:

$$H_0\text{: There is a significant difference between the two groups' average SC, } \Delta\mu_0 \neq 0$$

The employed statistical test is the Mann–Whitney–Wilcoxon (MWW)[58], a non-parametric test, since the data distributions are unknown, for upaired groups, considering that each group contains different subjects. The null-hypothesis is applied region by region, resulting in $90 \times 90$ tests to perform for each comparison. Considering the huge amount of trials, the possibility to reject a false positive increases, therefore, the Bonferroni correction is utilized, to balance this effect. A significance threshold of $\alpha = 0.05$ is defined, and the number of significant tests is considered 4050, half of the total size of the SC matrix, due to its symmetry, as explained in section 2.1.1. Consequently, p-values are considered significant when the order of magnitude is lower than $-5$, or $-\log_{10}(\text{p-values}) > 5$.

### 5.1.2 Empirical Functional Connectivity

The neurophysiological information is investigated by the employment of MEG data. This was collected at the ULB Hopital Erasme (Brussels, Belgium) on an Elekta Neuromag Vectorview scanner for the first 30 multiple sclerosis patients and 15 HCs, and on an Elekta Neuromag Triux scanner for the remaining cohort, due to the aforementioned upgrade. Both the MEG scanners share the same sensors layout, composed of 102 triples of sensors, each consisting of one magnetometer and two orthogonal planar gradiometers. Moreover, they are both placed in a lightweight magnetically shielded room (Elekta Neuromag & MaxshieldTM, Elekta Oy, Helsinki, Finland). MEG signals were recorded at 1 kHz sampling rate with a $0.1 - 330$ Hz band-pass filter. Subjects' head position inside the MEG helmet was continuously monitored using four head-tracking coils. The location of these coils and at least 400 head-surface points (on the nose, face, and scalp) were determined with an electromagnetic tracker (Fastrak, Polhemus, Colchester, Vermont, USA). The paradigm designed for the experiment is: 10 minutes eyes-closed resting-state. MEG data is preprocessed and transferred in source space using a beamformer algorithm[34, 59]. Given MEG time courses in source space, the following steps propose the development of the algorithm implemented to extract the quantities utilized in the further analyses:

1. The frequency content related to each time course is extracted by calculating the *Power Spectral Density*, employing the MATLAB function *pwelch()*. The frequency content related to each source is averaged over all the network's nodes. Moreover, for each subject, findpeak() function is employed to infer the power $\alpha$-peak, within the frequency window of $7 - 12$ Hz.

2. The second step consists in filtering time courses in 4 or 5 frequency bands, including brain rhythms displayed during resting state: $\theta$ $1 - 4$ Hz, $\delta$ $4 - 8$ Hz, $\alpha$ $8 - 12$ Hz and $\beta$ $12 - 20$ Hz. Depending on the analysis performed, the $\alpha$ band is spit in lower $\alpha$, $8 - 10$ Hz, and upper $\alpha$, $10 - 12$ Hz. The frequency bands of interest regard those that are altered in MS subjects. Therefore, the investigation focuses on the $\alpha$ and $\delta$ power bands.

3. During brain activity, functional networks are detected, by means of synchronization of amplitude envelope fluctuations between different regions. One of the methods to extract the amplitude envelopes consists in computing the Hilbert Transformation. The analytic signal $R_n(t)$, where $n = 1, ..., N$ and $N = 90$ brain parcels, can be described as a complex number:

$$R_n(t) = A_n(t)e^{i\phi(t)} \tag{5.1}$$

   where $A_n(t)$ is the amplitude of the analytic signal and $\phi_n(t)$ the related phase. In order to extract the amplitude envelope, MATLAB function *hilbert()* is utilized and the module is elicited. The *phase* of the signal, $\phi_n(t)$, is calculated by extracting the *angle()* of the Hilbert Transformation.

4. The envelope is a low frequency signal compared to the measured data. Therefore, it is downsampled to a lower frequency, 250 Hz. This step includes an additional band pass filter in a low frequency band, $0.01 - 0.1$ Hz, to extrapolate the envelope fluctuations. Moreover, the averaged signal among all the time series is extracted, and subtracted to each node, to discard the common line.

5. *Functional connectivity, FC* computation. The following step consists in computing the Pearson's correlation coefficient between each pair of amplitude envelope fluctuations. Therefore, a FC matrix is computed in each frequency band independently[34].

The main outcome of the algorithm is the *Empirical Functional Connectivity*, a matrix with dimension $N \times N$, where $N = 90$, number of brain's parcels. This is a symmetric matrix, since the Pearson's correlation coefficient does not allow to deduce causal interactions.

## 5.2 Model Implementation

The work of this thesis focuses on the implementation of a neurocomputational model to simulate brain activity. The model implemented is the Kuramoto model, which is employed also in several other studies [5, 55].

### 5.2.1 Coupled-Oscillators Model with Time Delay

The Kuramoto model employed in this work is a variant of the original Kuramoto Model, and *time delay* is the additional parameter. The following equation presents the mathematical description of the network's nodes intrinsic dynamic:

$$\frac{d\theta_n}{dt} = \omega + k \sum_{p=1}^{N} C_{np} sin(\theta_p(t - \tau_{np}) - \theta_n(t)), n = 1, ..., N \tag{5.2}$$

where $N$ is the number of parcels depending on the implemented brain parcellation atlas[43]. Going through the model's characteristics, the first one concerns the nodes' angular frequency, $\omega_n = \omega$. This is the same for each node, and it is characterized by the nodes' intrinsic natural frequency $f_n$, $\omega = 2\pi f_n$. This natural frequency is $f_n = 40Hz$, a value consistent with electrophysiological measurements[8, 26]. Additionally, $C_{np}$ is the coefficient weighting the connection between a determined pair of nodes $n$ and $p$. Following, two model's parameters are presented: $k$, global coupling strength of the model, and $\tau_{np}$, the time delay introduced in the interaction between two nodes. This last parameter depends on the actual distance between two regions, and it is computed as $\tau_{np} = D_{np}/v$, where $v$ is the conduction velocity between two regions. A simplification in modelling this last parameter must occur, defining a homogeneous time delay, $\tilde{\tau} = \tilde{D}/v$, where the ratio is computed between the average distance matrix $\tilde{D}$, and the conduction velocity, v, considered homogeneous all over the brain network. This model is implemented in the *Network-Kuramoto()* function[55], used along this thesis for every simulation. Among the inputs to this function, three are worth mentioning: SC, structural connectivity matrix from which the $C_{np}$ coefficient is extracted, and the two model's parameters k and $\tau$. Therefore, the only measurement that can really affect the model's performances is the SC. The other two parameters are assumed to belong within a range of values, $k \in 1, 2, .., 15$ and $\tau \in 1, 2, .., 30$. Depending on the analysis to conduct and its goal, the ranges themselves and the incremental step within these ranges slightly vary, i.e increment of 1 or 0.5.

After focusing on the model's dynamics at the node level, the dynamics of the entire system is considered, and the coefficients used to describe the network's dynamics are inferred. Two aspects must be highlighted: the achievable synchronization level, and the possible synchronization pattern

of the whole network. The quantity used to investigate this aspect is the *order parameter,* $R(t)$:

$$R(t)e^{i\Phi(t)} = \frac{1}{N}\sum_{n=1}^{N} e^{i\theta_n(t)}, N = 90 \tag{5.3}$$

where $R(t)$ measures the phase uniformity among the whole system. When it is equal to 0 there is no synchronization, while if it is equal to 1, the whole system is synchronized. Moreover, $\Phi(t)$ is the global phase[4]. To measure the occurrence of slow fluctuations in the synchrony degree, the standard deviation of $R(t)$ is computed, $\sigma_R = std(R(t))$, measuring the level of metastability of the system; slow amplitude fluctuations appear when sub-networks synchronize temporarily and then dissolve, displaying alternating meta-stable activity patterns, and $\sigma_R \neq 0$. These coefficients can also be inferred by the MEG time courses, since in the previous section, all the necessary inputs to compute the empirical synchrony degree are presented. However, along this dissertation, the metastability analysis remains focused on the model's simulations.

### 5.2.2 Simulated Functional Connectivity

Once brain signals are simulated, the simulated functional connectivity is computed. The algorithm to infer simulated functional connectivity follows the one proposed for the empirical FC; however, one step must be explained. As it can be observed from equation 5.2, the simulations outcome is a matrix of *phases*, since this is the model's state variable. The simulated matrix has dimensions $N$x$T$, where $N$ is the number of parcels considered in the model, and $T$ is the number of simulated time points. However, the first simulated 20 sec are discarded, representing a transient period that is not considered. Afterwards, the real simulated data are computed by extracting the *sin()* of the phases matrix; a sinusoidal regime with constant amplitude is assumed[5]. Eventually, the Pearson's correlation coefficient is computed to deduce the *Simulated Functional Connectivity.* Following, the synchrony degree and metastability are also inferred.

Concerning the model's parameters k and $\tau$, a simulation is run for each combination of parameters. Therefore, every simulation includes itself 15x30 simulations. The output related to an entire simulation are: simulated frequency content, synchrony degree, R(t), metastability, $\sigma_R$, and simulated functional connectivity, FC. Given the big computational demand required for each simulation, the algorithm includes a parallel pool that allows to recruit contemporaneously a certain number of cores, and for each, running a simulation concerning a pair of parameters. Along the development of the thesis, the algorithms were adapted and slightly modify with respect to the obtained results. The code related to the algorithm presented in this section is proposed in the appendix A, and the workflow is schematized in figure 5.2.

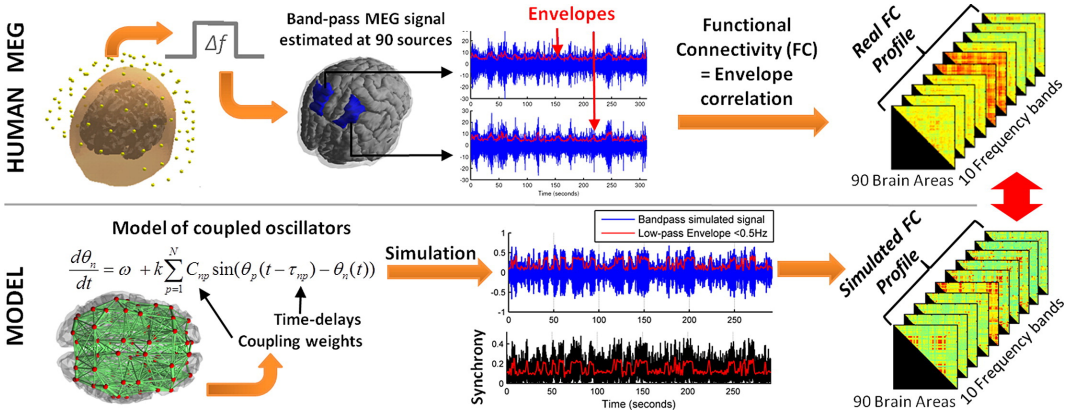


**Figure 5.2:** This figure proposes the workflow followed to extract simulated and empirical FC[4]. This figures refers to the reference paper, in which the frequency bands of filtering are 10. In this work, instead, these are only 4 or 5, depending on the analysis[5]

### 5.2.3 Model Optimization

Depending on the part of the work considered, this crucial step of the pipeline is conducted exactly in the same way. Hence, either for the simulations at the population level or at the subject level, the empirical and the simulated functional connectivity are matched so the extract the optimal model parameter that permits the achievement of the best model simulation.
To verify the model's performance, the Pearson's Correlation Coefficient is computed between simulated and empirical FC matrices. This is the following step of the workflow shown in figure 5.2. This comparison is performed in each frequency band, and for each pair of model's parameters $(k, \tau)$. Eventually, the outcome is a 3D matrix, $M \in R^{15x30x5}$, where the first dimension refers to the range of values assumed by $k$, the second one to $\tau$, and the last one to the frequency bands in which the correlation is executed. In figure 5.3, the model's performance grid is exemplified.

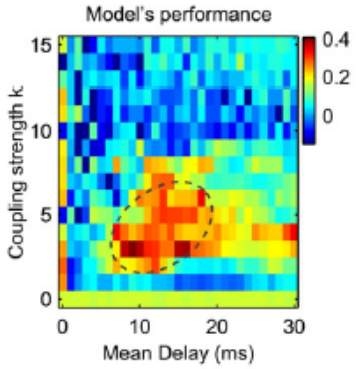


**Figure 5.3:** This plot shows the model's performance grid, where on the y and x-axes the model's parameters, k and $\tau$ respectively, are displayed. Each element of the grid represents the Pearson's correlation coefficient between the empirical FC and the simulated FC referred to that specific combination of parameters[5].

The real model optimization step entails the extraction of the pair of parameters for which the correlation coefficient between simulated and empirical FC is the best. For this step, the center of mass, *com*, of the model's performance matrix $M$ is computed as follows:

$$com(k, \tau) = \frac{\sum c(k, \tau) s(k, \tau)}{P} \tag{5.4}$$

where, $c(k, \tau) \in M$ refers to the model's performance matrix of correlation coefficients, $s(k, \tau)$ is the scale factor referring to the increasing step of each parameter, and $P$ is the total size of the performance matrix $M$. A different optimal pair of model's parameters is extracted in each frequency band. Again, depending on the part of the work, the pair of optimal parameters is acquired for each population under investigation, as in the first analysis, or for each subject, as in the last part of the work.

## 5.3 Simulations

In this section, it is described how the analysis is conducted in each of the three parts of this thesis. Although the crucial point remains always the implementation of the neurocomputational model, there are aspects of the analysis that change, such as the cohort of selected subjects, and the goal of the investigation itself.

### 5.3.1 Model Validation

This investigation aims at reproducing the findings present in Cabral et al. 2014[5]. The analysis conducted in this work tries to resemble as much as possible the one proposed by the reference study, in order to delete any possible factor that could affect the results and mislead the outcomes' interpretation. For instance, the dataset used for this analysis is selected consistently with the dataset composition of the reference paper in age, gender and pathophysiological condition of the included subjects. Therefore, among the two groups BRUMEG1 and BRUMEG2, only females, healthy controls and under 40 years old subjects are extracted, and the composition of the dataset used in this analysis is shown in table 5.3.

| | **BRUMEG1** | **BRUMEG2** |
|---|---|---|
| Female HC | 6 | 4 |
| Average Age | 32 | 31.5 |

**Table 5.3:** This table proposes the composition of the two groups of subjects extracted because fulfilling the requirements of being HC, female and $< 40yo$.

This analysis is conducted at the group level, therefore the SC in input is the *average* SC matrix, computed by averaging region by region the SC matrices of the included subjects. Considering the ranges of model's parameters, the grid of values that they assume is the following: $k = [1, 2, ..., 15]$, and $\tau = [0, 1, ..., 30]$. Furthermore, the frequency bands considered are 4: $1-4$ Hz, $4-8$ Hz, $8-12$ Hz, and $12-20$ Hz. Eventually, the quantity that are relevant for the results and further analysis are:

- The matrix of correspondence, $M \in R^{15x30x4}$, where the dimensions corresponds to $k$, $\tau$, and the number of frequency bands;
- The synchrony Degree, R, and the relative standard deviation, $\sigma_R$, measure of Metastability;
- The simulated Frequency Content.

### 5.3.2 Group Level Simulations

In the second part of the work, the Kuramoto Model is applied to groups of subjects with different neurological conditions, and 9 groups are identified. Concerning BRUMEG1 only HC, MS and MSB are observed, and the composition of each group is shown in table 5.1. Focusing on BRUMEG2, each sub-group (HC, MS and MSB) is split considering the the difference in gender, male and female, as shown in table 5.2. The analysis at the group level relies on the average SC matrix in input, and the simulated FC is then correlated with the average empirical FC, extracted by averaging region by region the FC of each subject. Among the model's parameters, k, coupling strength, changes with respect to the previous analysis, therefore $k \in [0.5, 1, ..., 10]$; whilst time delay, $\tau$ remains the same. Another difference with the previous investigation regards the filtering frequency bands: here 5 bands are proposed, where the $\alpha$ band is split in low $\alpha$, $8-10$ Hz and high $\alpha$, $10-12$ Hz. At this level of analysis, considerations on the results are qualitative and based on a visual inspection. The reason relies on the employment on the *mean*, a quantity susceptible to outliers.

### 5.3.3 Subject Level Simulations

The last part of the analysis conducted along this thesis, resembles the simulations at group level. For each dataset BRUMEG1 and BRUMEG2, the model is given in input the average

structural connectivity of the healthy controls, disregarding the age or gender. Following, the simulated functional connectivity is correlated with each single subject's FC matrix. Therefore, 5 pairs of optimal parameters are extracted for each subject, each one related to a single frequency band. As it can be noticed, the computational demand becomes unsustainable for a common CPU. To be able to perform the simulations in a reasonable amount of time, these are submitted to a remote supercomputer, *Hydra*. This cluster allows to compute simulations with an intense parallel pooling, decreasing drastically the computational time to few days. To visualize the results, different methods are utilized. Scatterplots are used to investigate possible correlations, while kernel density distribution graphs aim at moving the attention on the parameters' distributions. Furthermore, boxplots are employed to visually identify variation of parameters' means regarding different groups (HC, MS and MSB). This last examination is also deduced quantitatively, and the following null-hypothesis is proposed:

$H_0$: There is no difference between the averages model parameters referred to the following groups of subjects: MS, HC and MSB.

To verify this hypothesis, the MWW test is employed.

The last analysis performed on these outcomes aims at finding a correlation between the subject's $\alpha$-peak extracted from the frequency content of the MEG data, and the model's parameters. The correlation is always computed by means of Pearson's correlation coefficient. Following, the outcomes of the analyses are proposed.

# Chapter 6

# Results and Observations

This chapter presents the results obtained conducting the previously described analyses in chapter 4. The work of this thesis starts from the already extracted empirical functional connectivity and structural connectivity, which are given in input to the pipeline that then develops the Kuramoto model and the empirical and functional connectivity matching analysis, and the script is reported in A. This refers to the available scripts provided by Cabral et al. 2014a. Therefore, all the results and the analyses performed throughout this thesis starts from the performance matrix. The dissertation is developed in three sections, each one concerning one of the research objectives proposed.

## 6.1 Model Validation

The first part of the work aims at validating the performances of the Kuramoto model. To pursue this goal, the analysis proposed by Cabral et Al. 2014[5] is reproduced on a small part of the dataset described in table 5.3, which includes only healthy subjects that match by age and gender the population involved in the reference study. The comparison between the obtained results and the reference study is conducted by investigating two aspects: the *model performance* and the *metastability*.

### 6.1.1 Model Performance

After running a simulation for each pair of parameters (k, $\tau$) in the chosen grid $15 \times 30$, the model performance matrix, $M$, is computed by evaluating the Pearson's correlation coefficient between empirical and simulated Functional Connectivity matrices. $M$ is extracted in the following frequency bands $1-4$ Hz, $4-8$ Hz, $8-12$ Hz, $12-20$ Hz, and the outcomes are plotted in figures 6.1 and 6.2, regarding BRUMEG1 and BRUMEG2 datasets respectively.

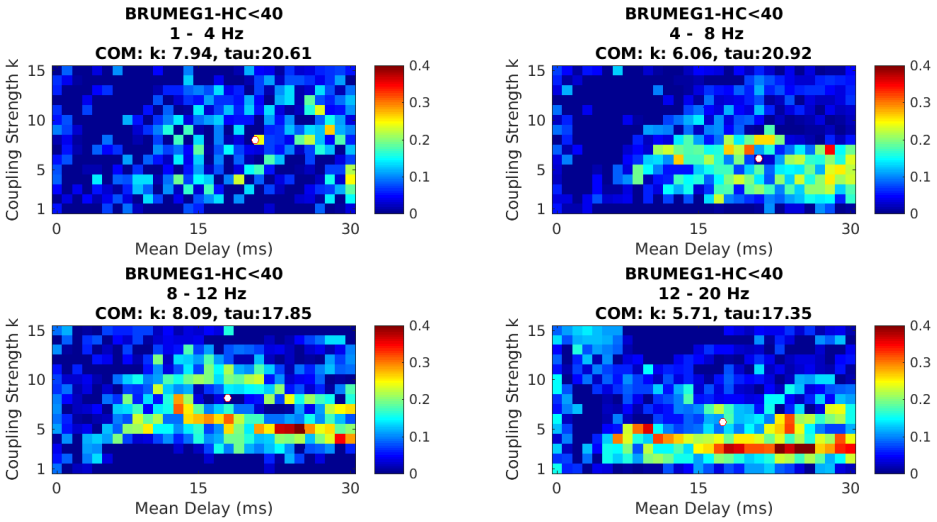


**Figure 6.1:** These graphs show the model's performance matrix regarding the simulation in which the employed dataset is composed of BRUMEG1 healthy female subjects, under the age of 40 years old.

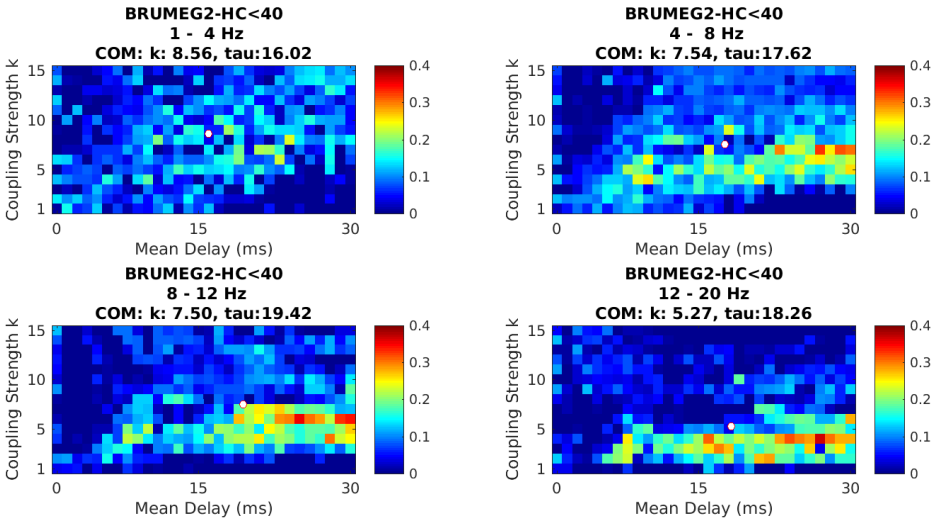


**Figure 6.2:** These graphs show the model's performance matrix regarding the simulation in which the employed dataset is composed of BRUMEG2 healthy female subjects, under the age of 40 years old.

In figure 6.3, the model performance proposed by the reference study is shown. An important observation follows; the reference study has conducted the analysis in 10 different frequency bands( $2-6$ Hz, $4-8$ Hz, $6-10.5$ Hz, $8-13$ Hz, $10.5-21.5$ Hz, $13-30$ Hz, $21.5-39$ Hz, $30-48$ Hz, $39-66$ Hz, $52-80$ Hz), whereas the proposed analysis only focuses on 4 bands. Nonetheless, the comparison is performed only in the frequency band $10.5-21.5$ Hz, as this presents the most interesting traits.

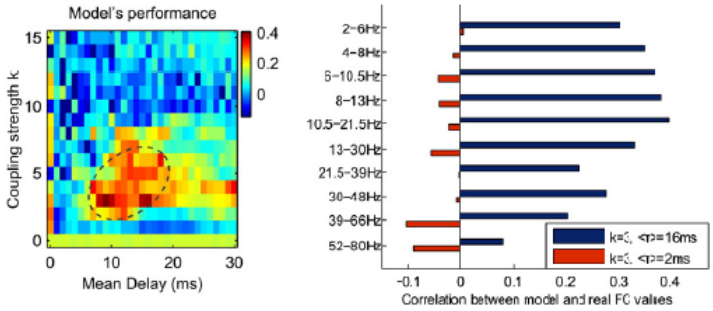


**Figure 6.3:** On the left, the figure shows the model's performance regarding the results obtained by the reference paper[5], only in the freq. band $10.5 - 21.5$. On the right, the Pearson's correlation coefficient between simulated and empirical FC matrices is extracted for the selected optimal pair of parameters $k = 3$ and $\tau = 16ms$, in each frequency band[5].

The optimal parameters elicited in our analysis are compared to the combination proposed by the reference study in the following table 6.1.

| | **BRUMEG1** | | **BRUMEG2** | | **Reference Study** | |
|---|---|---|---|---|---|---|
| | k | $\tau$[ms] | k | $\tau$[ms] | k | $\tau$[ms] |
| 1-4 Hz | 7,94 | 20,61 | 8,56 | 16,02 | 3 | 16 |
| 4-8 Hz | 6,06 | 20,92 | 7,54 | 17,62 | 3 | 16 |
| 8-12 Hz | 8,09 | 17,85 | 7,50 | 19,42 | 3 | 16 |
| 12-20 Hz | 5,71 | 17,35 | 5,27 | 18,26 | 3 | 16 |

**Table 6.1:** This table presents the optimal pairs of model's parameters (k,$\tau$) extracted in each frequency band, for BRUMEG1 and BRUMEG2 datasets, and the combination proposed by Cabral et Al. 2014a.

In the reference study, the model optimal parameters are defined as $k = 3$ and $\tau = 16$ ms. For this combination, the model performance in each frequency band is extracted, and gathered in figure 6.3.

Analyzing table 6.1, a mismatch is noticed between the optimal parameters inferred by this analysis, average $k = 7$ and $\tau = 19$ ms, and those proposed by the reference study, $k = 3$ and $\tau = 16$ ms. The factors that might affect these results are the following. First, one can notice the different DTI b-values characterizing the measurements in the two studies. In the reference paper, this parameter is set at b-value$= 1200s/mm^2$, whilst in this study the two coefficients are b-value$_1 = 800s/mm^2$ and b-value$_2 = 1000s/mm^2$, for BRUMEG1 and BRUMEG2 DTI-measurements respectively. Furthermore, there is a slightly different composition in the dataset: the average age of the cohort of subjects in [5] (mean$=$ 29 years old, 10 subjects) is younger than the group of subjects chosen for this analysis (mean$=$ 32 years old). In addition to this, in Cabral's study, three out of ten subjects are males, whereas only females are selected in this work, where the number of subjects is smaller, 6 and 4 subjects for BRUMEG1 and BRUMEG2 dataset respectively.

Despite the results concerning the model's parameters, other important outcomes can be inferred. In figures 6.1 and 6.2, the model's performance achieves the strongest correlation, about $\rho = 0.3 - 0.4$, in the carrier frequency bands of $8 - 10$ Hz and $12 - 20$ Hz. These represent the filtering frequency bands in which both simulated and empirical FCs are extracted, and then correlated. These results are consistent with the $\alpha$ and $\beta$ rhythms detected in resting-state MEG measurements, as explained in section 2.1.3. Furthermore, this consideration is in agreement with Cabral's outcomes, where the strongest correlation is observed in the frequency band $10.5 - 21.5$ Hz.

### 6.1.2 Metastability

The next analysis concerns the evaluation of the *metastability*. The results elicited by the simulations performed throughout this thesis are shown in figure 6.4 and figure 6.5, related to BRUMEG1 and BRUMEG2 dataset respectively.

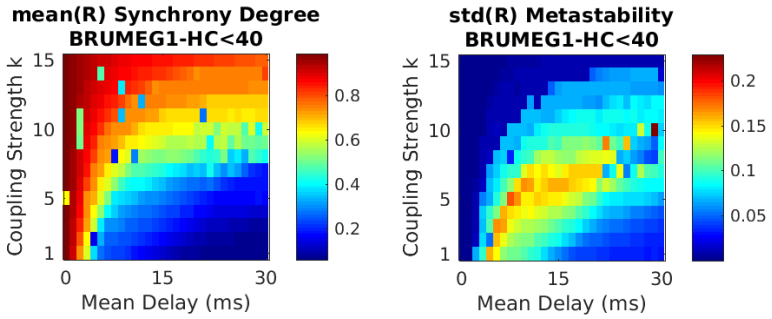


**Figure 6.4:** This figure shows the metastability regarding the group of subjects selected from BRUMEG1 dataset. On the left, the synchrony degree/order parameter is plotted, on the right the standard deviation of the order parameter is present: the metastability.

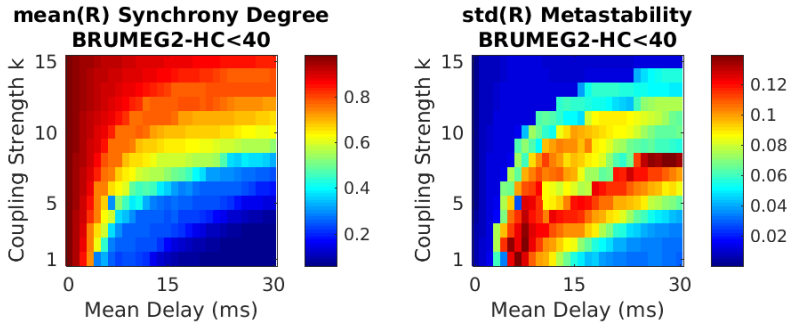


**Figure 6.5:** This figure shows the metastability regarding the group of subjects selected from BRUMEG2 dataset. On the left, the synchrony degree/order parameter is plotted, on the right the standard deviation of the order parameter is present: the metastability.

In figure 6.6, the results concerning the metastability proposed by the reference paper are shown.

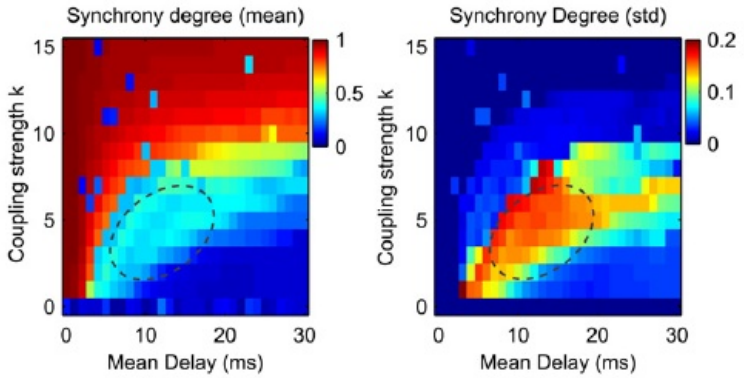


**Figure 6.6:** This figure shows the Metastability proposed by the reference study[5]. On the left, the synchrony degree is plotted, on the right the metastability is present.

Considering these results, one can notice two aspects. First, we remind that metastability is computed as the standard deviation of the order parameter, $R(t)$, measuring the system's degree of synchronization, as explained in chapter 5. Considering the optimal parameters combination, $k = 7$ and $\tau = 19$, the obtained order parameter, $R \approx 0,3$, is consistent with respect to the reference study outcome of $R \approx 0,4$. The metastability also agrees with the reference outcome, $0,1 < \sigma_R < 0,2$.
A closer inspection on the metastability results discloses a characteristic double-tail trend in the metastability plot related to BRUMEG2 simulation, 6.5. This effect is characterized by the splitting of the region of high correlation coefficients in the metastability plot; therefore, a larger range of model parameters seem to permit simulations that accomplish high metastability. To investigate this aspect more in detail, simulations are run for the 4 subjects included in the BRUMEG2 subgroup, and the results are proposed in the following paragraph.

### Single Subject Investigation

Before presenting the results concerning this analysis, an important consideration must be introduced. The metastability is inferred by the analysis of simulated data, therefore only the model and its inputs are involved in this analysis. The only input required by the Kuramoto model, except for its parameters, is the SC matrix. It is reminded that the SC matrix is extracted from DTI-based tractography, and the only difference between BRUMEG1 and BRUMEG2 SC matrices is based on the different DTI scanner's parameter set during the measurements. Consequently, the double-tail effect might be related either to the model intrinsic mechanisms, or to the SC matrix. Following, the metastability results obtained by the 4 subjects simulations are plotted in figures 6.7 - 6.10. The correspondent subject's SC is shown next to each simulation's result, to verify whether the double-tail trend is related to a particular trait in the subject's SC matrix.

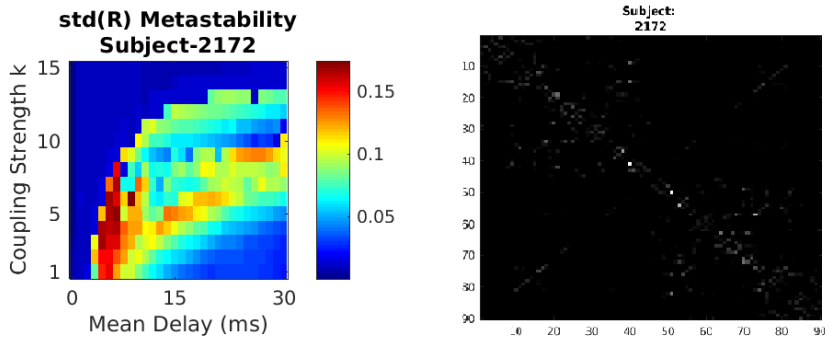


**Figure 6.7:** In this figure, the metastability results concerning subject 2172 are shown on the left. On the right, the subject's SC matrix is proposed.

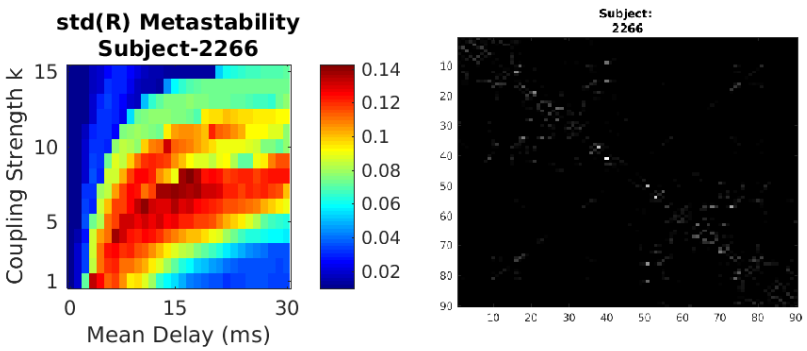


**Figure 6.8:** In this figure, the metastability results concerning subject 2262 are shown on the left. On the right, the subject's SC matrix is proposed.

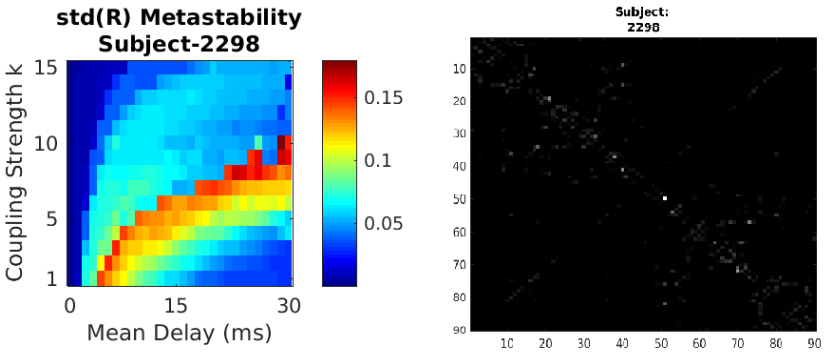


**Figure 6.9:** In this figure, the metastability results concerning subject 2298 are shown on the left. On the right, the subject's SC matrix is proposed.

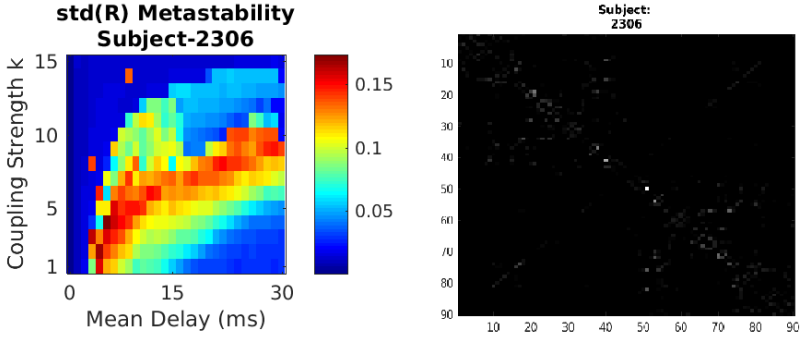


**Figure 6.10:** In this figure, the metastability results concerning subject 2306 are shown on the left. On the right, the subject's SC matrix is proposed.

The double-tail trend is obtained in three out of four simulations. However, a global observation of the subjects' SCs do not disclose any particular feature in these matrices. Therefore, this trend cannot be related to a SC trait, and a different perspective of investigation is proposed.

Another characteristic that marks the selected subjects is the age range. Only subjects under the age of 40 years old are considered. Therefore, a new analysis examines the possible relationship between age and SC matrix within the BRUMEG2 dataset, by means of the Pearson's correlation coefficient.

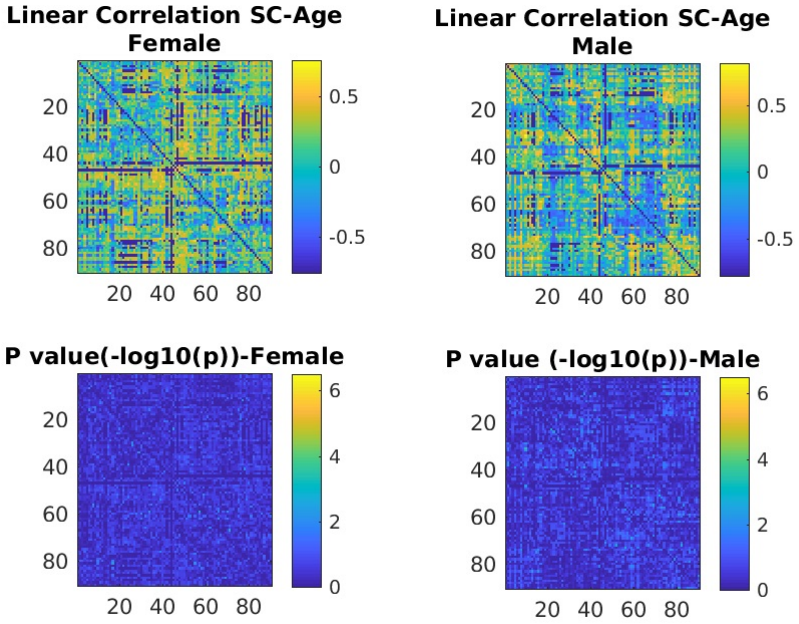


**Figure 6.11:** This figure shows the results of the correlation between SC and age in BRUMEG2 dataset. On the left, the p-values are plotted, whereas on the right, the $-log_{10}(p-value)$ is displayed for a better visualization of the outcomes

As displayed in figure 6.11, no correlation is obtained between age and structural connectivity, since the p-value presents values $> 10^{-2}$ over the whole SC matrix.

### Finer Simulations

A simulation on a finer grid of model's parameters is proposed, where the model parameters ranges are $k = 1, 1.5, ..., 10$ and $\tau = 5, 5.5, ..., 30$. Two simulations are run, to verify that this characteristic double-tail trend appears constantly in different simulations, and the results are shown in figure 6.12.

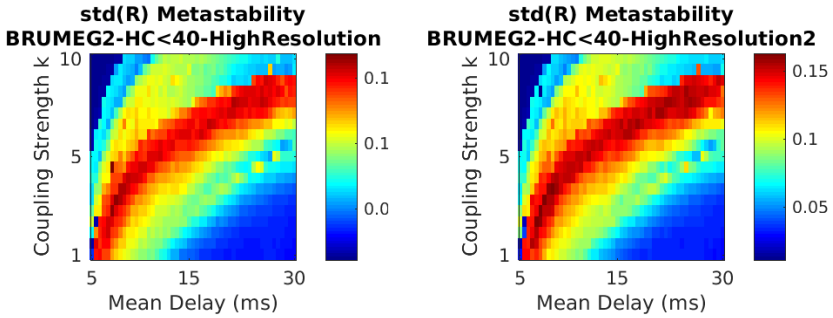


**Figure 6.12:** These plots show the metastability results of two high resolution simulations. Two identical simulations are run with a smaller incremental step for both the model's parameters $k$ and $\tau$.

The metastability results of the two high resolution simulations, do not show the double-tail trend displayed in figure 6.12. To conclude the investigation of the metastability behaviour, the results at first have shown a peculiar double-tail effect which must be related to the model itself or its inputs, which are basically the structural connectivity matrix and the pair of simulation parameters k and

$\tau$. When thinning the grid of the model parameters, the trend disappears, and thus, the grid of values employed for the model parameters is considered to cause the observed double-tail trend.

## 6.2 Group Level Simulations

As presented in the previous section, the first analysis succeeds in reproducing Cabral's results[5], therefore, the model is validated on the available dataset. Following, the core analyses of this thesis are exposed, with the related results.

At first, the model is run considering groups of subjects that present different conditions: healthy controls, HC, Multiple Sclerosis subjects, MS, and Multiple Sclerosis-Benzodiazepine positive patients, MSB. Several studies have shown a disruption of the FC matrix in MS patients [24, 52]. Therefore, to achieve the strongest correlation between simulated and empirical FCs, we expect the model optimal parameters to adapt to different cases, and this is .

Before running the model, an additional analysis is conducted, to investigate possible differences between the average structural connectivity of different groups of subjects identified by gender, pathological condition, and belonging dataset, BRUMEG1 or BRUMEG2. One is reminded that the average of the SC matrix of the subjects belonging to the group identified is provided to the model as input, and this constrains the possible functional interactions between distinct brain regions. Therefore, changes in model performances could be led by structural connectivity features which differ between different groups (HC and MS subjects), and this could alter the results and mislead their interpretation. The following paragraph provides the results of the investigation that aims to identify significant differences between the average SC matrices referred to different groups. This is important not only to identify possible structural connectivity variations among populations, but also to conduct the discussion of the model simulations results.

### 6.2.1 Structural Connectivity Analysis

To investigate SC differences among groups of subjects, 7 comparisons are performed, herein Mann-Whitney U test is employed[58]. The results concerning the comparisons are shown in the following figures 6.13 - 6.19, where both the p-values and $-log_{10}(p-value)$ are displayed, for a better visualization of the results. The significance threshold is set at p-values $< 10^{-5}$.

- BRUMEG1 vs BRUMEG2.

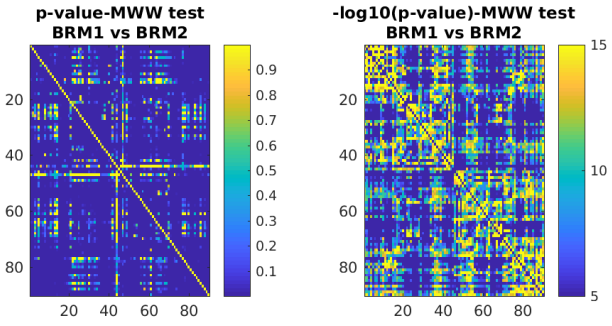


**Figure 6.13:** In this figure, the comparison between BRUMEG1 and BRUMEG2 subjects' SC matrices is shown. On the left, the p-values are plotted, whereas on the right, the $-log_{10}(p-value)$ is displayed for a better visualization of the outcomes.

- BRUMEG1: MS vs HC.

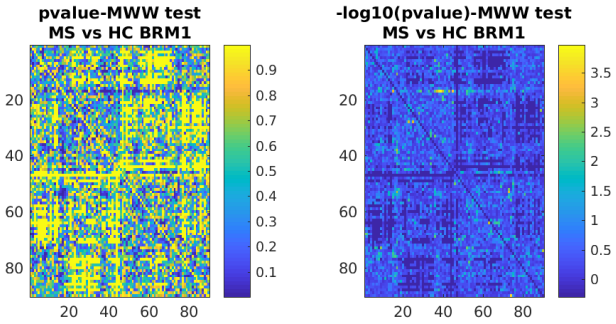


**Figure 6.14:** In this figure, the comparison between BRUMEG1 HC and MS subjects' SC matrices is shown. On the left, the p-values are plotted, whereas on the right, the $-log_{10}(p-value)$ is displayed for a better visualization of the outcomes.

- BRUMEG1: MS vs HC vs MSB

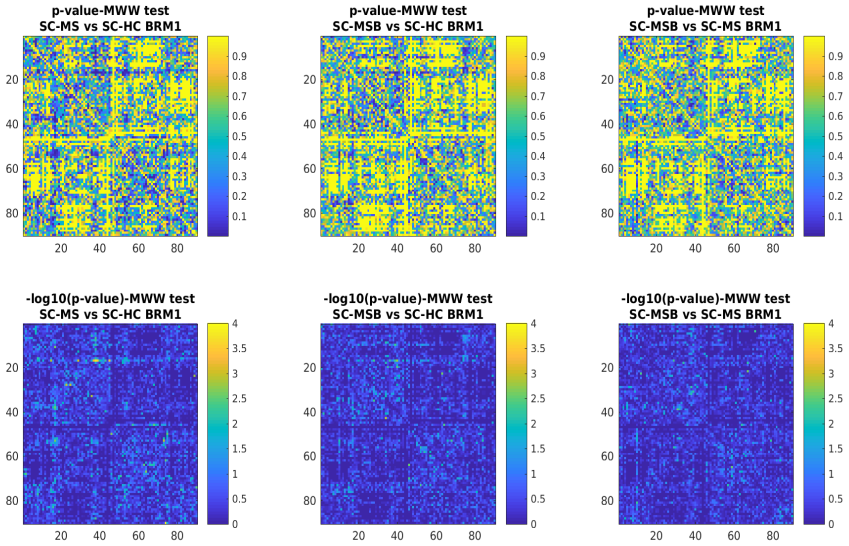


**Figure 6.15:** In this figure, the comparison between HC, MS and MSB subjects' SC matrices is shown, concerning BRUMEG1 dataset. The first row shows the plots considering the p-values results, whereas the $-log_{10}(p-value)$ results are displayed on the bottom row, for a better visualization of the outcomes.

- BRUMEG2: Male vs Female

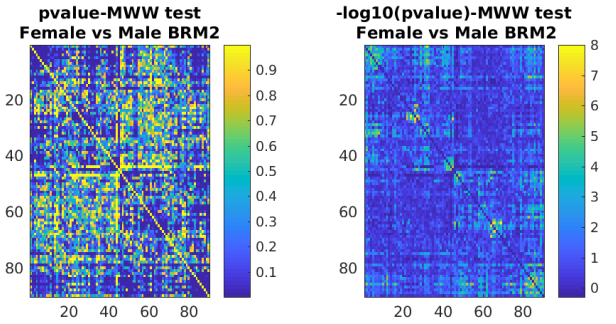


**Figure 6.16:** In this figure, the plots show the comparison that is performed within BRUMEG2 dataset, between Male and Female subjects' SC matrices. On the left, the p-values are plotted, whereas on the right, the $-log_{10}(p-value)$ is displayed for a better visualization of the outcomes.

- BRUMEG2: MS vs HC

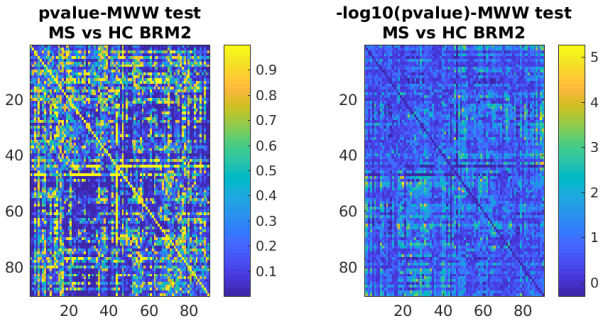


**Figure 6.17:** In this figure, the comparison between BRUMEG2 MS and HC subjects' SC matrices is shown. On the left, the p-values are plotted, whereas on the right, the $-log_{10}(p-value)$ is displayed for a better visualization of the outcomes.

- BRUMEG2 HC: Male vs Female

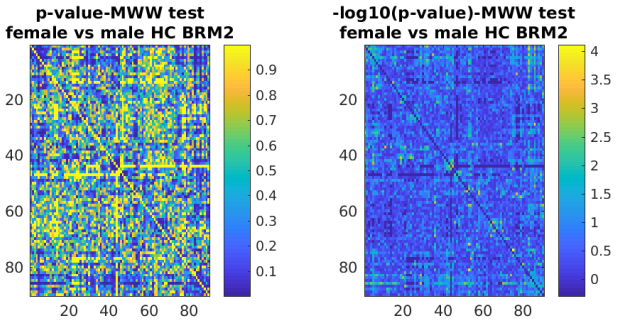


**Figure 6.18:** In this figure, the comparison between BRUMEG2 HC Male and Female subjects' SC matrices is shown. On the left, the p-values are plotted, whereas on the right, the $-log_{10}(p-value)$ is displayed for a better visualization of the outcomes.

- BRUMEG2 MS: Male vs Female

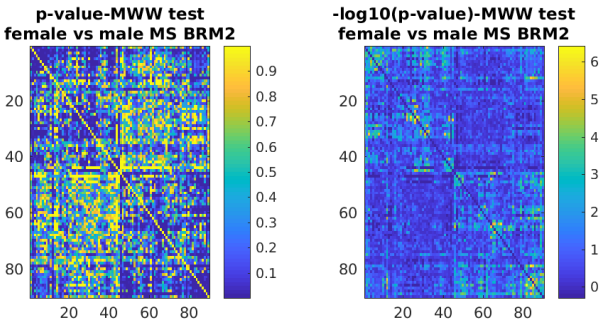


**Figure 6.19:** In this figure, the comparison between BRUMEG2 MS Male and Female subjects' SC matrices is shown. On the left, the p-values are plotted, whereas on the right, the $-log_{10}(p-value)$ is displayed for a better visualization of the outcomes.

Among all these comparisons, only the one regarding BRUMEG1 versus BRUMEG2 shows significant results. As aforementioned, the SCs of these two groups are acquired with two different DTI b-values. As a result, the SC matrices extracted from DTI-based tractography show significant differences, and figure 6.13 displays that the MWW-test yields p-values $< 10^{-5}$ almost all over the

SC matrix. Conversely, comparisons between HC and MS subjects, with or without MSB cases included, do not exhibit interesting differences. This statement can be referred to both BRUMEG1 and BRUMEG2 datasets' analyses. The MWW-tests between MS and HC SCs obtain p-values $> 10^{-2}$ over the whole SC matrix, as shown in figures 6.14 - 6.17. Within BRUMEG2 dataset, there are both female and male subjects, and a comparison between SCs related to the two populations is pursued. However, figures 6.16, 6.18 and 6.19, show p-values $> 10^{-3}$ considering the whole SC matrix. Despite the proposed results, the literature presents findings that highlight some differences between SC matrices between genders, and pathological conditions. Nevertheless, this is a research field yet under investigation[38]. The model simulations are run for each one of the identified group in this section.

### 6.2.2 Model's Performance

After the analysis concerning SC differences, the model is applied to different groups of subjects, following the different populations identified in the previous section 6.2.1. Therefore, 9 simulations are run; the identified BRUMEG1 groups are: HC, MSB-MS Benzodiazepine positive and MS- MS Benzodiazepine negative; whereas BRUMEG2 subdivision consists first in male and female cohorts of subjects, afterwards in each of these, HC, MS and MSB groups are split.

For each simulation, the average SC matrix of the group is provided as input for the model, and the simulated FC is then correlated to the average empirical FC. The quantity which the analysis relies on, is the *average*, and due to its susceptibility to outliers, only a qualitative examination of the results is entailed.

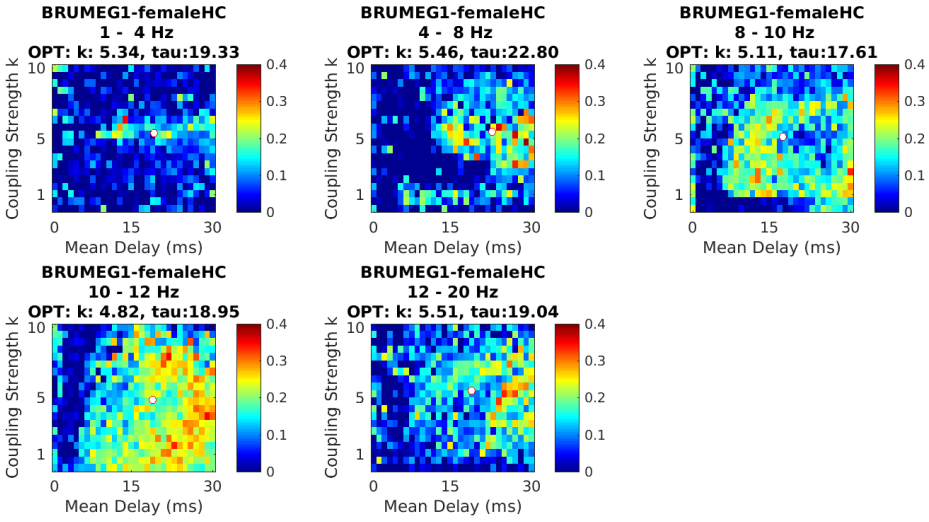


**Figure 6.20:** The model's performance for the BRUMEG1 HC simulation is plotted, for each frequency band independently. The optimal pair of parameters is pointed by the white dot, and the combination is printed in the title.

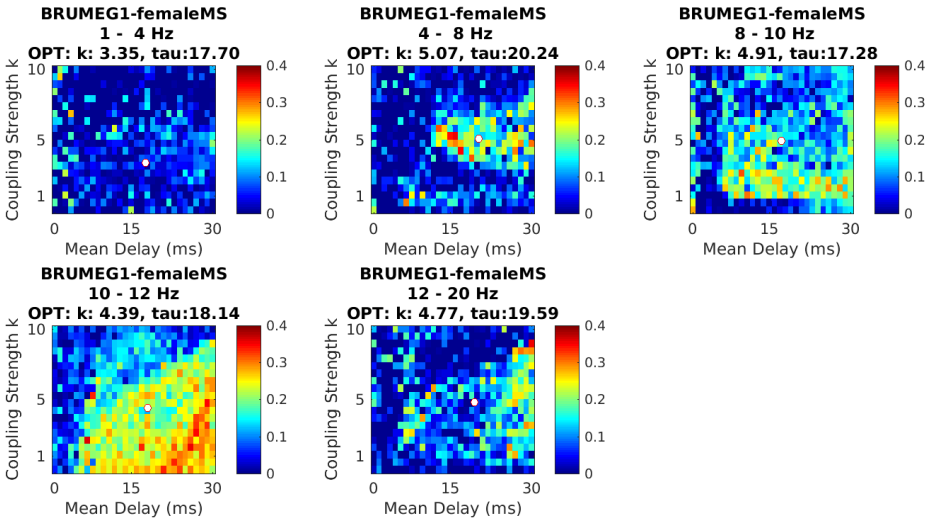


**Figure 6.21:** The model's performance for the BRUMEG1 MS simulation is plotted, for each frequency band independently. The optimal pair of parameters is pointed by the white dot and the combination is printed in the title.

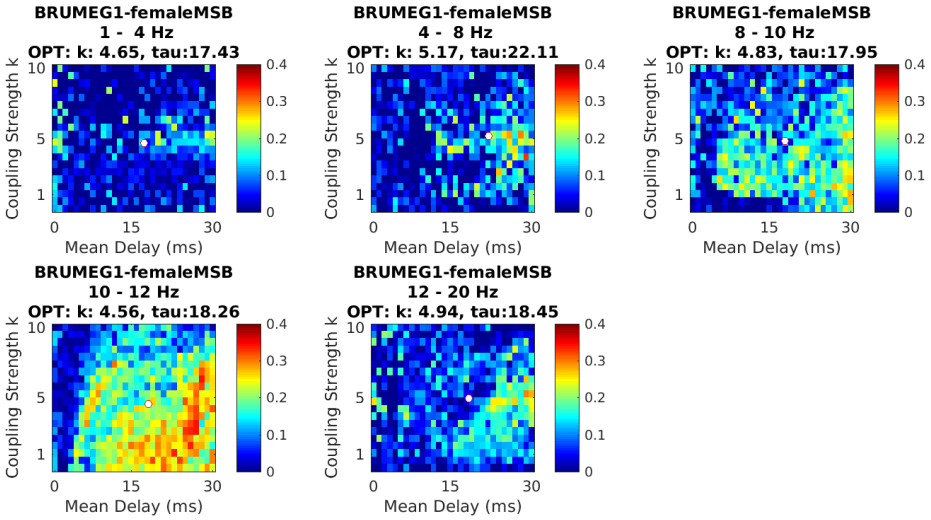


**Figure 6.22:** The model's performance for the BRUMEG1 MSB simulation is plotted, for each frequency band independently. The optimal pair of parameters is pointed by the white dot and the combination is printed in the title.

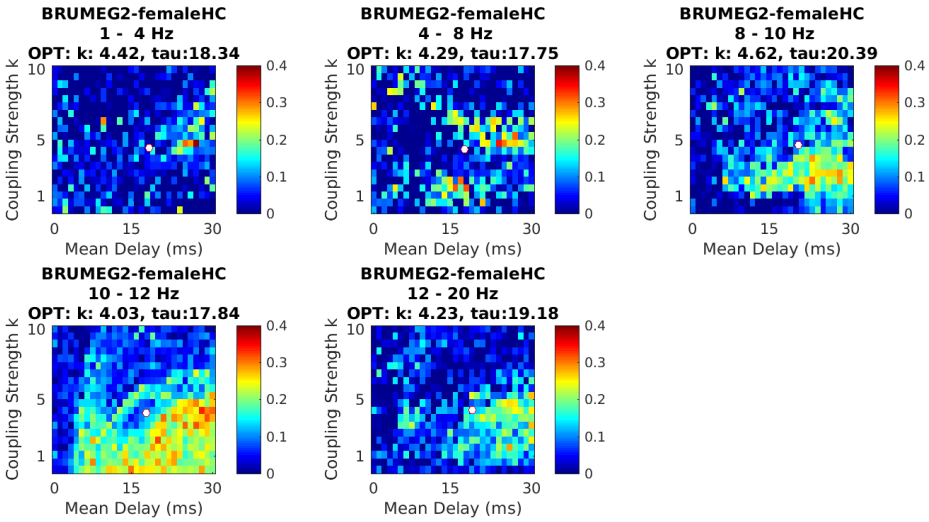


**Figure 6.23:** The model's performance for the BRUMEG2 female HC simulation is plotted, for each frequency band independently. The optimal pair of parameters is pointed by the white dot and the combination is printed in the title.

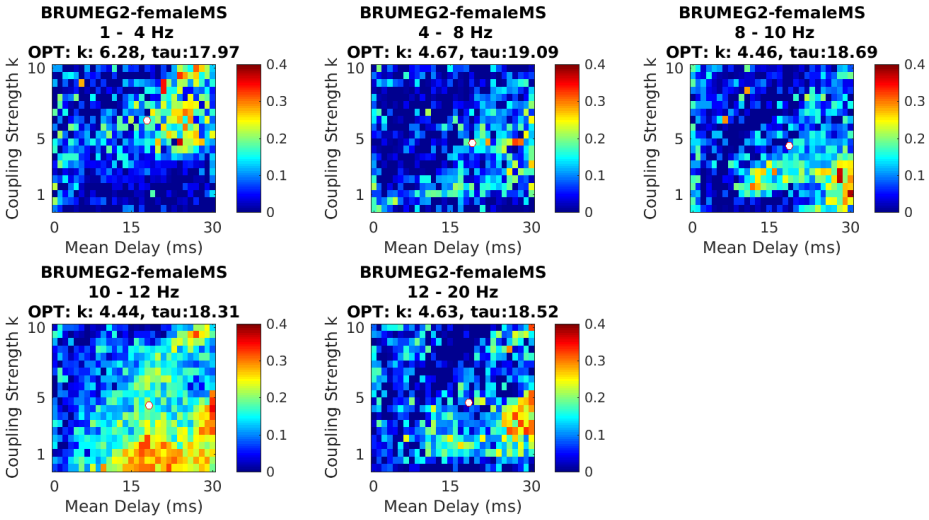


**Figure 6.24:** The model's performance for the BRUMEG2 female MS simulation is plotted, for each frequency band independently. The optimal pair of parameters is pointed by the white dot and the combination is printed in the title.

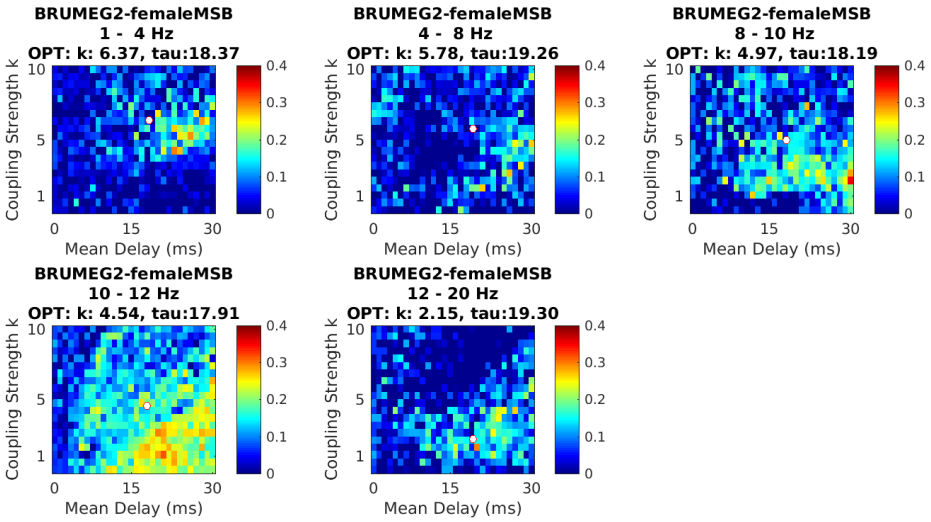


**Figure 6.25:** The model's performance for the BRUMEG2 female MSB simulation is plotted, for each frequency band independently. The optimal pair of parameters is pointed by the white dot and the combination is printed in the title.

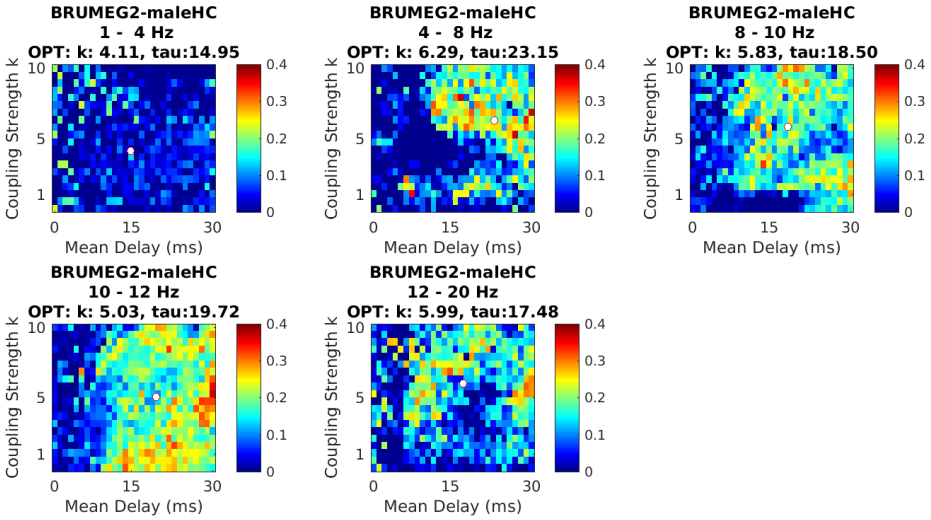


**Figure 6.26:** The model's performance for the BRUMEG2 male HC simulation is plotted, for each frequency band independently. The optimal pair of parameters is pointed by the white dot and the combination is printed in the title.

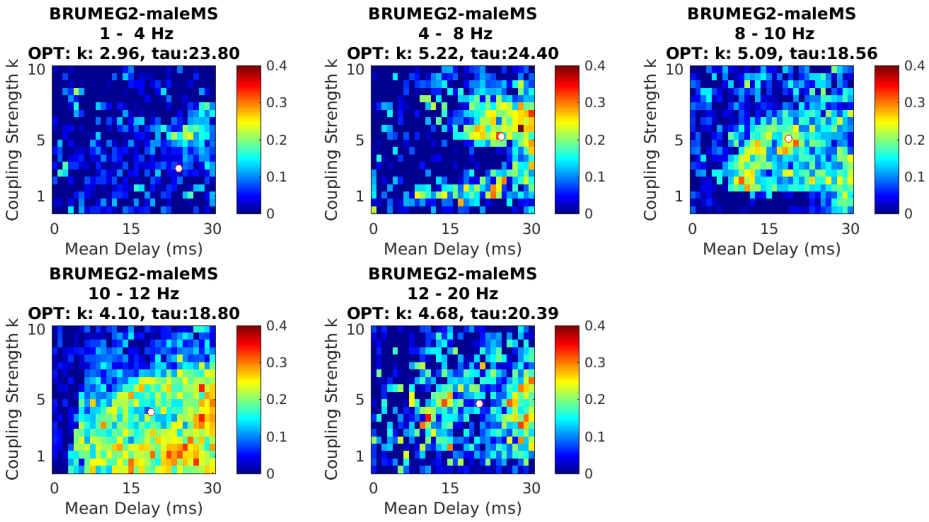


**Figure 6.27:** The model's performance for the BRUMEG1 male MS simulation is plotted, for each frequency band independently. The optimal pair of parameters is pointed by the white dot and the combination is printed in the title.

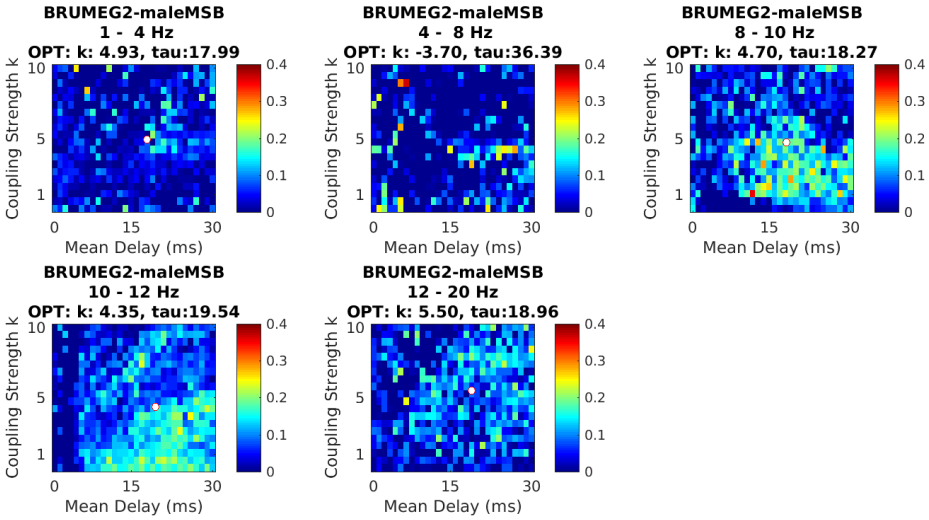


**Figure 6.28:** The model's performance for the BRUMEG2 male MSB simulation is plotted, for each frequency band independently. The optimal pair of parameters is pointed by the white dot and the combination is printed in the title.

Despite the qualitative observations, several interesting considerations can be inferred by these results. First, the implementation of the Kuramoto model in groups of MS patients display the same characteristics exhibited in HC simulations, consistently with the reference study[5]. In fact, in both groups, the correlation coefficients, *rho*, achieves the highest value in the $\alpha$ frequency band, and in this specific analysis in the $8-10$ Hz and $10-12$ Hz bands. In tables 5.1 and 5.2, the sizes of the different populations are displayed, and an interesting observation regards the slightly weaker correlation coefficients, $\rho \approx 0.2$, in simulations considering smaller populations, as can be inferred by the results considering BRUMEG2 male MSB simulation, which is performed only considering a single subject, figure 6.25. Another important aspect regards the distribution of the strong correlation coefficients in the model's performance matrix. Focusing on the frequency band $10-12$ Hz, we observe the results of the simulations regarding MS and HC groups, disregarding

of the belonging dataset. The area where the correlation coefficients attain the highest values, is centrally located and homogeneously distributed in the model's performance grid, concerning the HC simulations, figure 6.26; whereas it is shifted in the bottom right corner of the matrix when observing the simulations regarding MS groups, figure 6.27.

As last observation, one can recognize the slightly different behaviour between male and female groups, visible in particular in the $10-12$Hz. The strong correlation region in the model's performance matrix is shifted between HC and MS groups, considering both male and female simulations' results. However, the effect is more pronounced in males, and this is consistent with literature results that report stronger FC alteration effects in male than in female patients [24]. In this part of the work, the model is proved to reflect variation in the FC matrix between groups of subjects with different pathological conditions. Given these observations, the course of the analysis moves to implement the model to simulate single subject resting-state activity, and investigate the model capability to tune its parameters to detect FC differences between subjects, which would allow to identify a possible biomarker. Before stepping into this critical analysis, the metastability of the model simulations at the group level is investigated.

### 6.2.3 Metastability

The second part of the analysis at the population level concerns the examination of the metastability results. In figures 6.29 and 6.30, we exhibit the results for BRUMEG2 Male groups, HC and MS respectively.

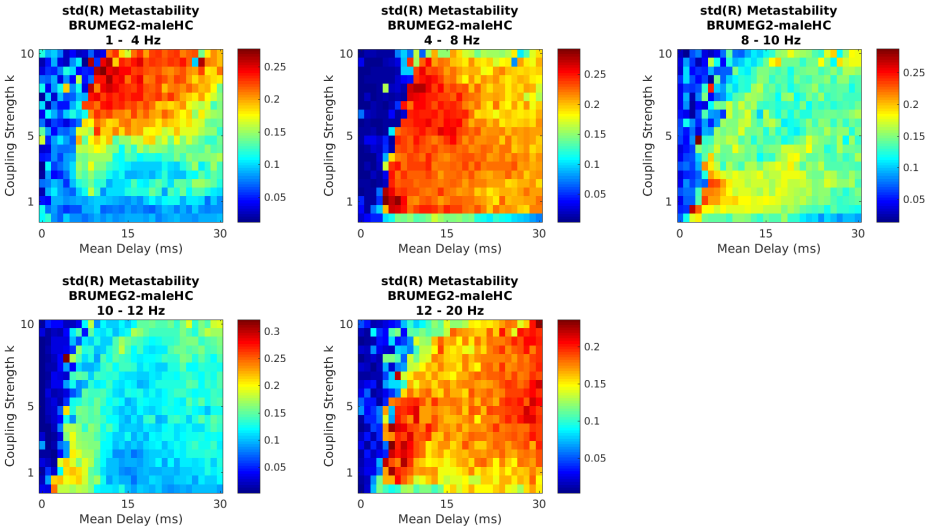


**Figure 6.29:** The metastability results are shown, regarding BRUMEG2 male HC dataset.

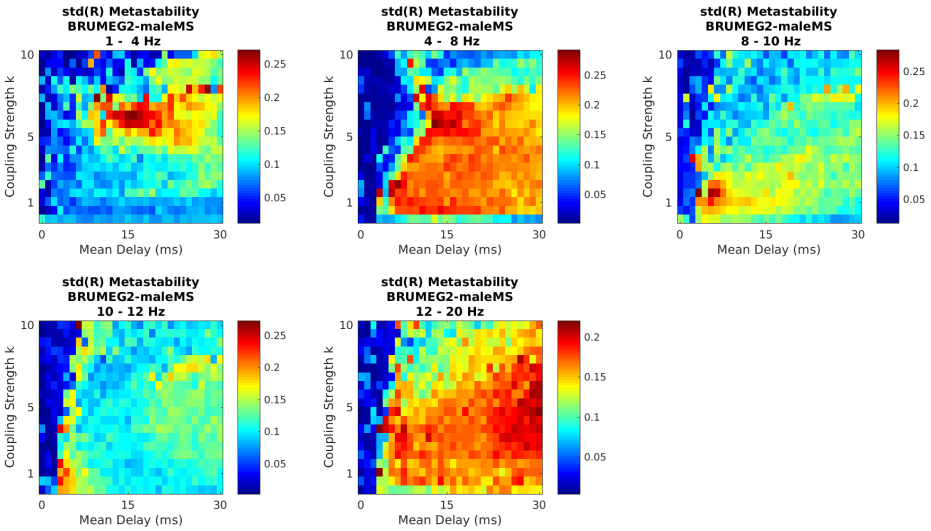


**Figure 6.30:** The metastability results are shown, regarding BRUMEG2 male MS dataset.

The metastability is extracted in each frequency band separately, to highlight its different trend concerning different frequency bands. Considering the $\alpha$ band, the metastability results $0.1<\sigma_R<0.2$ when the optimal model parameters are $k = 5$ and $\tau = 18$. However, the expected trend of this quantity is different from the analysis proposed in section 6.1 where the validation of the model was pursued. Although detailed examination of the metastability deviates from the ultimate goal of this thesis, the metastability pattern among the different frequency bands is an important aspect to take into consideration, and a further investigation of the phenomenon should be pursued.

## 6.3 Subject Level Simulations

The implementation of the Kuramoto model at the group level reveals the model's capability to detect differences in FC matrices when groups of subjects with different health or pathological conditions are considered. The following step aims at investigating the model's performance in detecting FC variations at a lower scale, the subject level.

### 6.3.1 Model's Performance

For each subject's simulation, the healthy controls average SC is given in input to the Kuramoto Model. As the whole analysis proposed so far, the average SC of the HC subjects is computed for BRUMEG1 and BRUMEG2, independently. Eventually, the simulated FC is correlated with the subject-specific FC. In figure 6.31, the results concerning the model's performance for the specific subject 2164 is presented, for each frequency band separately.

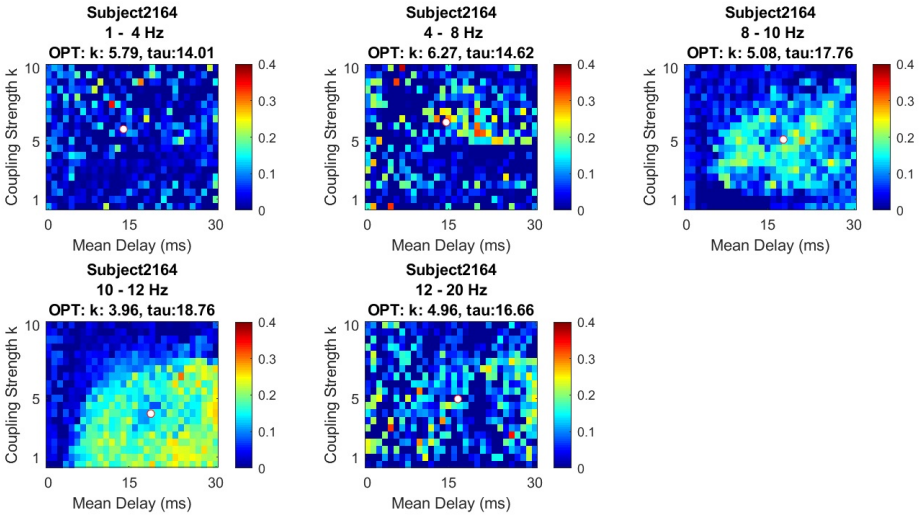


**Figure 6.31:** This figure displays the model's performance obtained for subject 2164 simulation, in each frequency band.

Consistently with the observation proposed in the previous section, the obtained Pearson's correlation coefficients are slightly weaker compared to the results at the group level proposed in section 6.2.2.

### 6.3.2 Subject-Specific Simulations Analysis

Although the analyses are performed in all the frequency bands defined in the methods, the most meaningful data are obtained in the $\alpha$, $8-10$ Hz and $10-12$ Hz, and $\beta$, $12-20$ Hz, frequency bands; therefore, we propose the results regarding these specific frequency bands. The first outcomes are displayed in the scatterplots in figures 6.32 and 6.33, for BRUMEG1 and BRUMEG2 datasets respectively. Each point represents the optimal pair of model's parameters extracted for each subject in each frequency band. Next to each scatterplot, a kernel distribution graph shows the density distribution of the optimal parameters. Each graph concerns a specific frequency band and the three conditions (HC, MS and MSB) are highlighted in three different colors.

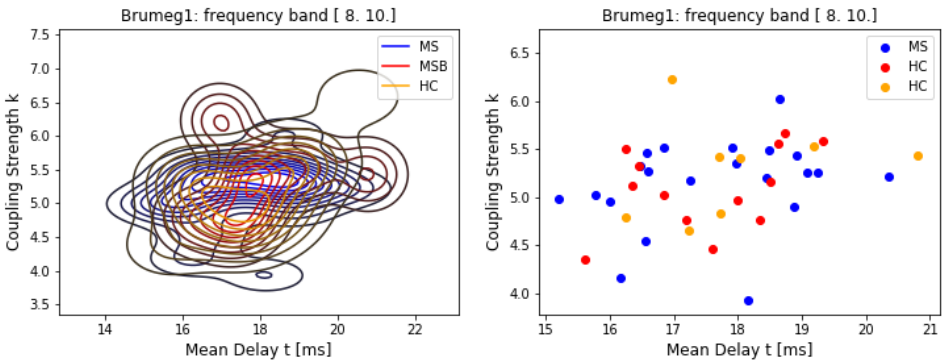

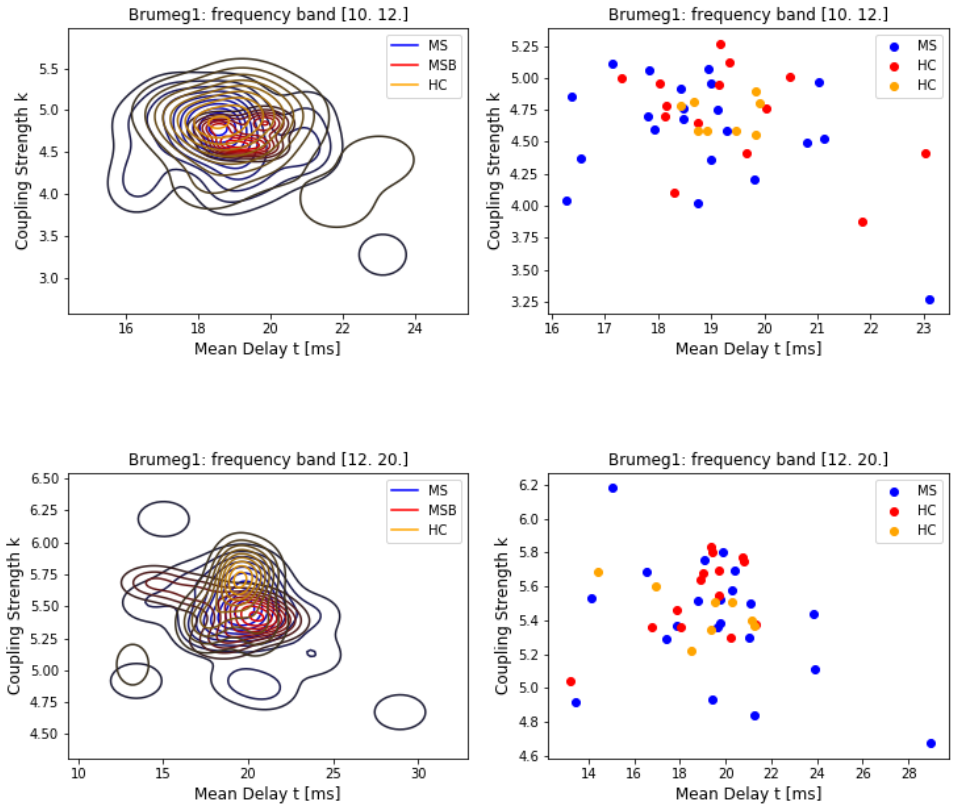


**Figure 6.32:** This graphs show results concerning BRUMEG1. On the right the scatter plot of the optimal pairs of model's parameters extracted for each subject, therefore the plot shows coupling strength k versus mean delay, $\tau$. The three groups of HC, MS and MSB are highlighted in different colors. On the left, the same results are proposed, however a kernel density plot is shown to focus the attention on the distribution of the parameters related to different groups (HC, MS, MSB). Each row presents the results related to a specific frequency band, following $8-10$ Hz, $10-12$ Hz, $12-20$ Hz.

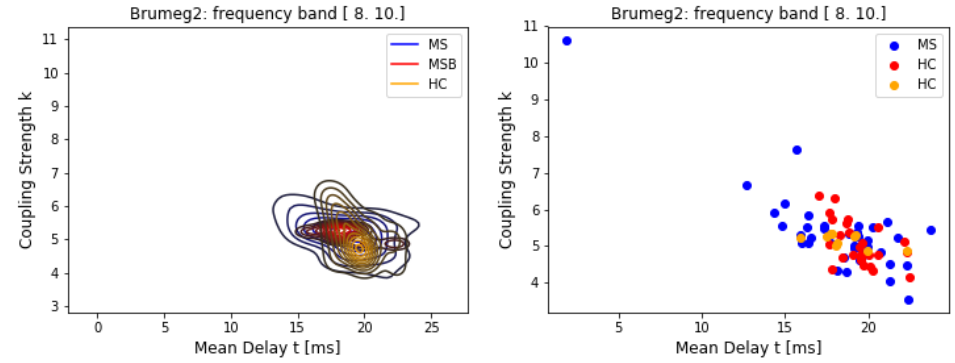

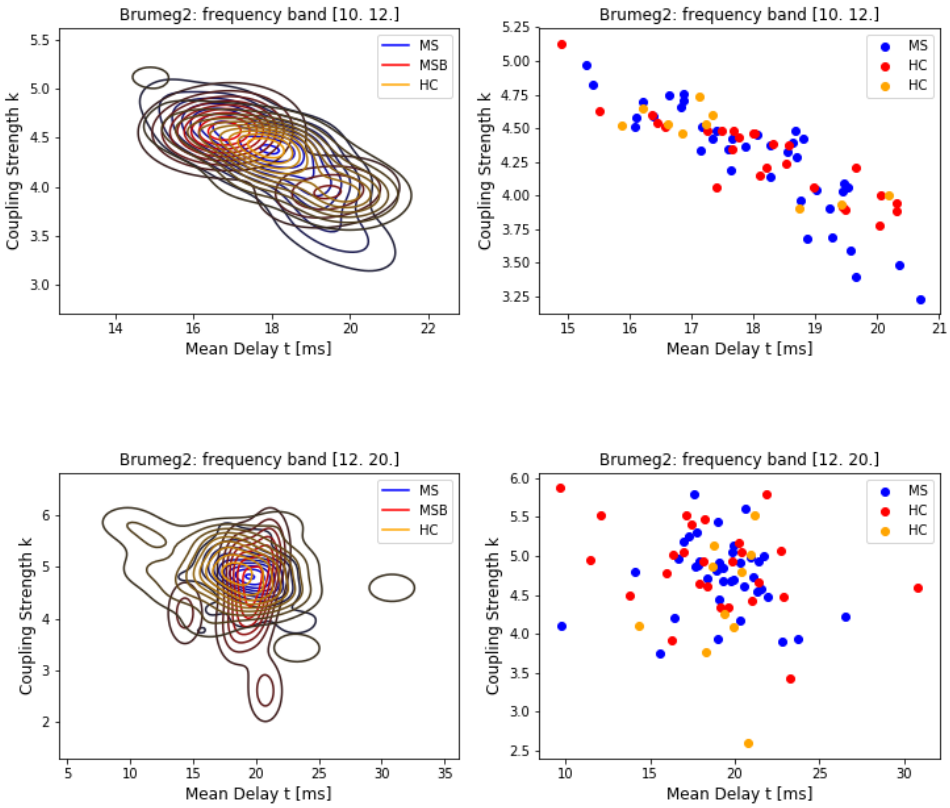


**Figure 6.33:** This graphs show the results concerning BRUMEG2. On the right the scatterplots display the optimal pairs of model's parameters extracted for each subject, therefore the plot considers coupling strength k versus mean delay, $\tau$. On the left the same results are proposed, however a kernel density plot is shown to focus the attention on the distribution of the parameters related to different groups(HC, MS, MSB). Each row presents the results related to a specific frequency band, following $8-10$ Hz, $10-12$ Hz, $12-20$ Hz.

A visual examination of these sets of graphs elicits two observations. First, the density distributions plot does not reveal a significant difference in the mean parameters between different groups (HC, MS and MSB). This is also visible in the boxplots proposed in figures 6.34 and 6.35, concerning BRUMEG1 and BRUMEG2 respectively. To confirm the proposed assumption, the results of the MWW test are shown in table 6.2. The comparison is performed only between the two groups of interest HC and MS. Setting a significance level of $\alpha = 0.05$, all the comparisons yield p-values above the significance threshold. This analysis is performed to investigate whether the model's adaptation capability that is observed qualitatively in section 6.2.2 is elicited also at the subject level.

| **BRUMEG1** | **k** | $\tau$ |
|---|---|---|
| | **HC-MS** | **HC-MS** |
| 8-10 Hz | 0.99 | 0.85 |
| 10-12 Hz | 0.35 | 0.29 |
| 12-20 Hz | 0.17 | 0.51 |

| **BRUMEG2** | **k** | $\tau$ |
|---|---|---|
| | **HC-MS** | **HC-MS** |
| 8-10 Hz | 0.27 | 0.16 |
| 10-12 Hz | 0.93 | 0.71 |
| 12-20 Hz | 0.33 | 0.36 |

**Table 6.2:** This table presents the results of the MWW tests performed to compare model's parameters averages between different groups of subjects, HC, MS and MSB, for BRUMEG1 and BRUMEG2.

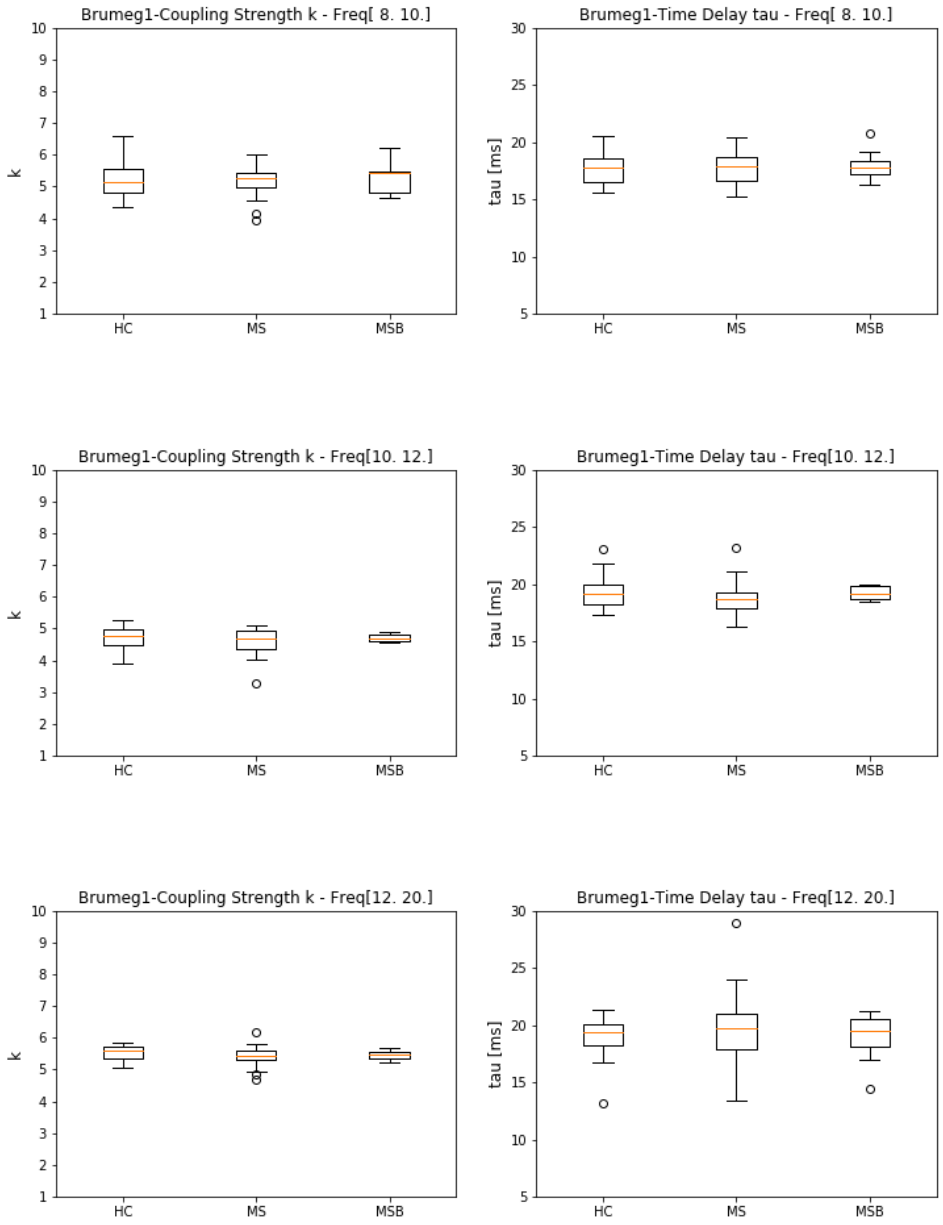


**Figure 6.34:** These boxplots show the results concerning BRUMEG1. The comparison focuses on the three groups of subjects, HC, MS and MSB. The graphs on the left present the results regarding k, whilst on the right the results regard $\tau$. Each row presents the results related to a specific frequency band, following $8-10$ Hz, $10-12$ Hz, $12-20$ Hz.

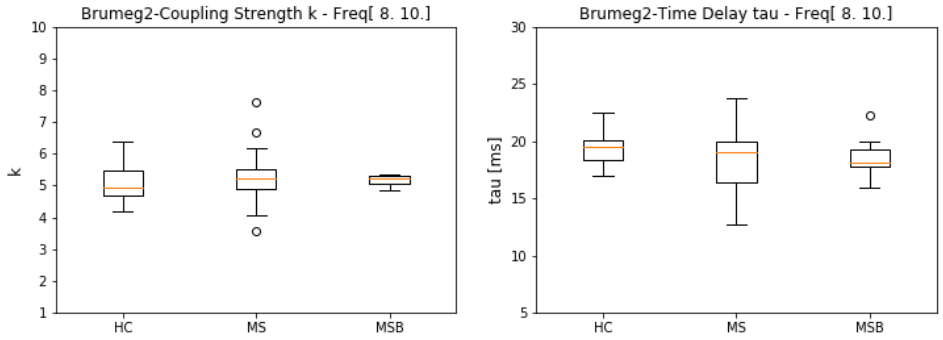

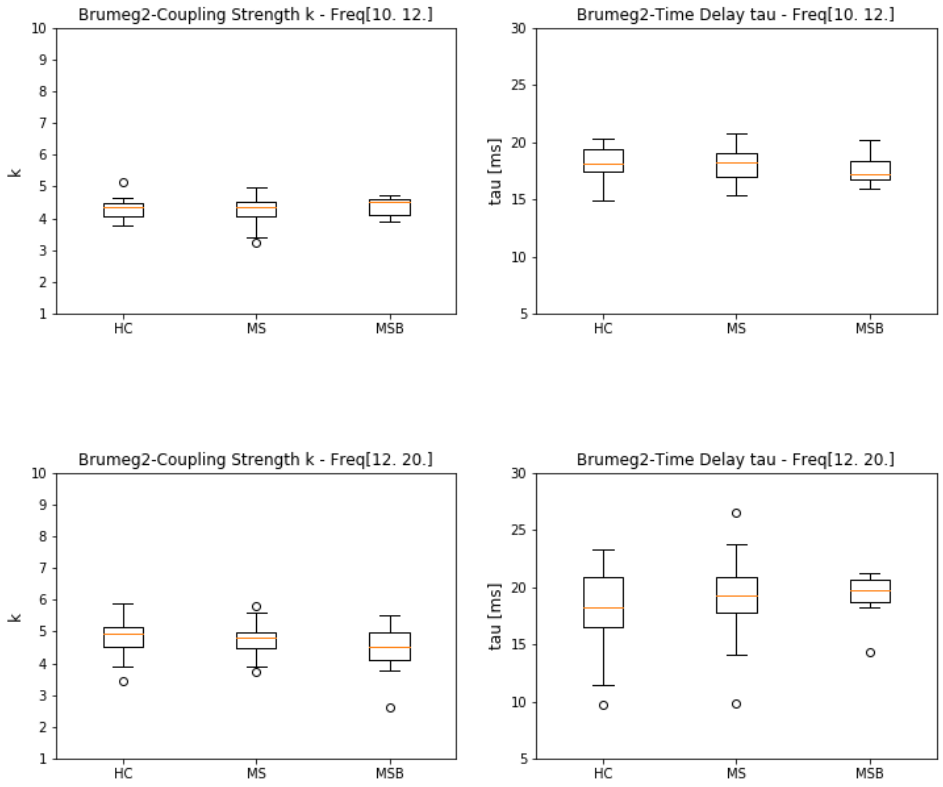


**Figure 6.35:** These boxplots show the results concerning BRUMEG2. The comparison focuses on the three groups of subjects, HC, MS and MSB. The graphs on the left present the results regarding k, whilst on the right the results concern $\tau$. Each row presents the results related to a specific frequency band, following $8-10$ Hz, $10-12$ Hz, $12-20$ Hz.

The second observation inferred from figures 6.32 and 6.33, concerns a possible correlation between the two model's parameters k and $\tau$. This consideration is further investigated in the following section.

### Correlation k and $\tau$

To explore a possible correlation between the two model's parameters, the Pearson's Correlation coefficient is computed between k and $\tau$, and this analysis is performed in each frequency band, considering each condition (HC, MS, MSB) separately. The results are shown in table 6.3, for BRUMEG1 and BRUMEG2 independently.

| BRUMEG1 | HC | MS | MSB |
|---|---|---|---|
| 8-10 Hz | 0.66 | 0.26 | 0.22 |
| 10-12 Hz | -0.42 | -0.35 | 0.06 |
| 12-20 Hz | 0.63 | -0.44 | -0.62 |

| BRUMEG2 | HC | MS | MSB |
|---|---|---|---|
| 8-10 Hz | -0.54 | -0.81 | -0.64 |
| 10-12 Hz | -0.89 | -0.88 | -0.85 |
| 12-20 Hz | -0.35 | -0.03 | 0.14 |

**Table 6.3:** Pearson's correlation coefficients extracted from the correlation between the model's parameters k and $\tau$. On the right results concern BRUMEG1, and on the left BRUMEG2.

The focus is set on the frequency bands $8-10$ Hz and $10-12$ Hz. In table 6.3, BRUMEG2 parameters show a moderate to strong negative correlation consistently in all the proposed frequency bands. This trend involves a decrease in global coupling strength, when the time delay is increased. Conversely, BRUMEG1 shows only a moderate positive correlation in HC in the $8-10$Hz band,

and for the rest, mild positive and negative correlations are displayed without a consistent pattern among different groups and frequency bands.

### 6.3.3 Model Performances and Cognitive Impairment

As mentioned along the dissertation, the ultimate goal consists in detecting a possible model parameter that can be tuned to the patient specific cognitive condition, and thus, become a biomarker to assess the patient's condition. However, there is no possibility to directly observe the model performances in function of the cognitive impairment level of a subject, and an intermediate parameter is required. The power $\alpha$-peak has shown a correlation with cognitive impairment, and thus, with FC disruption, in early MS[52]. More specifically, a $\alpha$-peak shift towards lower frequency is detected in early MS[51]. Therefore, this quantity can be utilized to investigate a possible correlation between the model parameters, k and $\tau$, and cognitive impairment.

#### $\alpha$-peaks test

Before correlating the $\alpha$-peak with the model parameters, a comparison between averages $\alpha$-peaks concerning different groups is conducted. Consistently with all the dissertation, the analysis is developed for BRUMEG1 and BRUMEG2 independently, by employing the MWW test. Three comparisons are performed, as shown in table 6.4.

| **BRUMEG1** | **p-values $\Delta\alpha$-peak** |
|---|---|
| **HC-MS** | 0.05 |
| **HC-MSB** | 0.52 |
| **MS-MSB** | 0.05 |

| **BRUMEG2** | **p-values $\Delta\alpha$-peak** |
|---|---|
| **HC-MS** | 0.48 |
| **HC-MSB** | 0.21 |
| **MS-MSB** | 0.23 |

**Table 6.4:** This table shows the result of the MWW test to determine a significant different in average $\alpha$-peak between different groups, HC, MS, and MSB.

Setting a significance threshold of $\alpha = 0.05$, none of the results obtained can be considered significant, since all the inferred p-values are $\geq 0.05$, as shown in table 6.4. Following, the correlation of the $\alpha$-peaks with the model parameters is investigated.

#### $\alpha$-Peaks vs Model Parameters

The last step of the analysis concerns the investigation of a possible relationship between model parameters and the $\alpha$-peaks extracted from the empirical MEG data. The power $\alpha$-peak has been proven to correlate with cognitive impairment, and therefore with FC disruption, in early MS[52]. Consequently, it is utilized to investigate a possible correlation between the model's parameters, k and $\tau$, and cognitive impairment. First, the scatterplots showing $\alpha$-peaks versus optimal model's parameters are presented in 6.36 and 6.37, for BRUMEG1 and BRUMEG2 respectively. In agreement with the previous analyses, only three frequency bands are considered, $8 - 10$ Hz, $10 - 12$ Hz, and $12 - 20$ Hz.

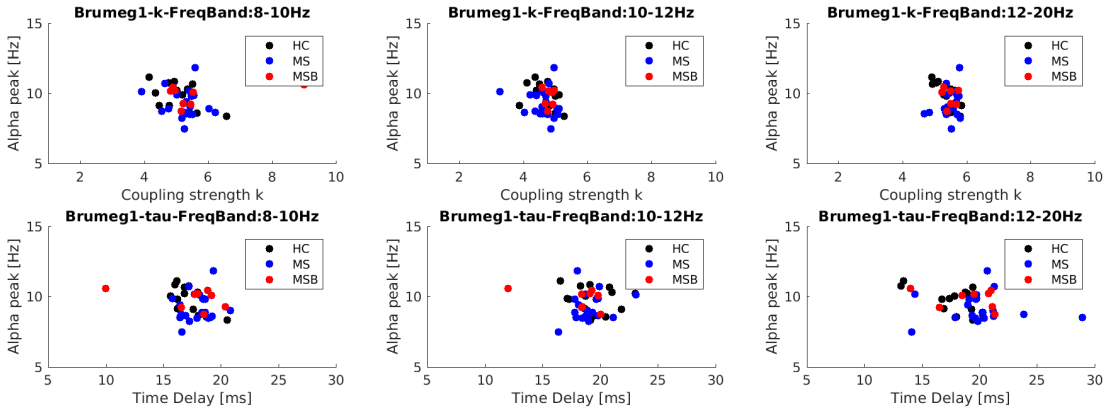


**Figure 6.36:** These plots show the results concerning BRUMEG1. The set of graphs present the $\alpha$-peak extracted from the empirical frequency content for each subject, versus the model's optimal parameters, k in the first row and $\tau$ in the second one. The three columns relate to the three frequency bands that are considered, $8-10$ Hz, $10-12$ Hz, $12-20$ Hz.

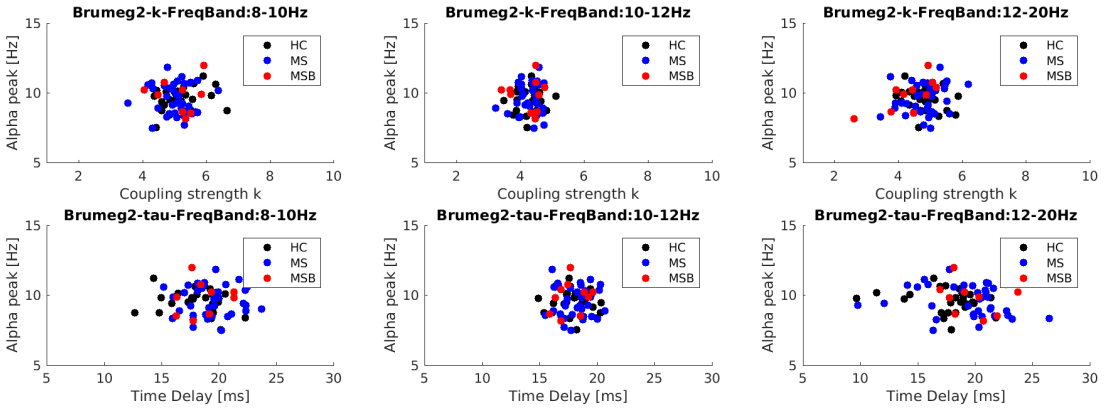


**Figure 6.37:** These plots show the results concerning BRUMEG1. The set of graphs present the $\alpha$-peak extracted from the empirical frequency content for each subject, versus the model's optimal parameters, k in the first row and $\tau$ in the second one. The three columns relate to the three frequency bands that are considered, $8-10$ Hz, $10-12$ Hz, $12-20$ Hz.

A shallow observation of these plots does not allow to elicit the presence of a relationship between these variables, because data appears to spread uniformly. Therefore, a more detailed investigation is performed, computing the Pearson's correlation coefficient between subject specific $\alpha$-peaks, extracted from MEG measurements, and model's parameters, k and $\tau$, in each frequency band and for each group in analysis, separately.

| **BRUMEG1** | **k vs $\alpha$-peak** | | | **$\tau$ vs $\alpha$-peak** | | |
|---|---|---|---|---|---|---|
| | HC | MS | MSB | HC | MS | MSB |
| 8-10 Hz | -0.53 | 0.10 | 0.38 | -0.65 | -0.09 | -0.42 |
| 10-12 Hz | -0.35 | 0.21 | 0.45 | -0.19 | -0.04 | -0.46 |
| 12-20 Hz | -0.74 | 0.29 | 0.45 | -0.23 | -0.10 | -0.33 |

| **BRUMEG2** | **k vs $\alpha$-peak** | | | **$\tau$ vs $\alpha$-peak** | | |
|---|---|---|---|---|---|---|
| | HC | MS | MSB | HC | MS | MSB |
| 8-10 Hz | 0.25 | 0.08 | 0.15 | -0.18 | -0.07 | -0.11 |
| 10-12 Hz | 0.11 | -0.01 | -0.07 | -0.06 | -0.002 | 0.23 |
| 12-20 Hz | -0.23 | 0.29 | 0.71 | -0.08 | -0.21 | -0.16 |

**Table 6.5:** Pearson's correlation coefficients between $\alpha$-peaks and model's parameters, concerning BRUMEG1 and BRUMEG2 datasets, on the left and on the right respectively.

The obtained correlation coefficients are shown in table 6.5. Observing BRUMEG1 results, as far as MS subjects are concerned, no correlation is noticed, whereas a mild to moderate negative correlation is obtained for healthy controls. This parallel trend between k and $\tau$ is inconsistent

with the correlation between the two parameters found in the previous paragraph. On the other hand, considering BRUMEG2, almost no correlation is observed in any population, for the most interesting frequency bands $8 - 10$ Hz and $10 - 12$ Hz.

# Chapter 7

# Discussion

In this chapter, we aim at providing an overview and an interpretation of the obtained results, considering similar studies and related findings present in the literature. We accentuate the step forward of the conducted analyses, but also the flaws and possible improvements. The development of this chapter follows the same structure proposed in the previous two, Methods and Results. Therefore, three main sections are discussed, presenting the conclusions on the research questions proposed in chapter 4.

## 7.1 Implementation of Kuramoto Model

The Kuramoto model is a neurocomputational model already successfully implemented in many studies to simulate resting-state brain activity[5, 55, 57]. This model is used to simulate whole-brain network activity, in which each node is described as a system of coupled-oscillators. The state variable describing each node dynamics is the *phase*, and a sinusoidal regime is inferred[4, 53]. An important parameter must be introduced in the original model, to assure that the model performances resemble resting-state brain activity: the *time delay,* $\tau$. This factor brings in a delay in the interaction between phases. Physiologically, this delay between brain regions communication is caused by a finite conduction velocity, which depends on the myelination level of the communication pathway, and the delay introduced by the information transfer occurring in the synaptic cleavages[45]. Eventually, the model parameters are two: k, global coupling strength, and $\tau$, time delay.

### Model Performance

In MEG studies, resting-state brain activity is observed to display power peaks in the $\alpha$ frequency band, $8 - 12$ Hz: the 10 Hz peak[48, 50]. Furthermore, in $\alpha$ and $\beta$ frequency bands, brain regions interactions occur by synchronization of slow amplitude envelope fluctuations, $< 0.1$ Hz. The long distance brain regions interactions occur at low frequencies, $\alpha$ and $\beta$ bands, and hence, the analyses are focused in these ranges. The amplitude envelopes are computed by employing the Hilbert Transformation, and extracting the related amplitude. The Pearson's correlation coefficients is computed to correlate the amplitude envelope fluctuations between each pair of brain network nodes, and therefore, the empirical Functional Connectivity matrix is carried out[5]. The last, but not least, observation considers the intrinsic characteristic of the brain network to develop temporally functional patterns. This particular dynamic regime is defined as *metastability*[5, 47]. Specifically, in resting-state activity different networks, RSNs, are detected. These never involve the whole brain network but subsystems, that are temporally activated, and then dissolve[26].
This paragraph summarizes the main features that characterize the acquired MEG resting-state

measurements, from which this thesis starts. The goal of this work is to investigate the model performances in comparison with the empirical MEG data by means of functional connectivity matching in different cases, rather than having a deep understanding of the model intrinsic mechanisms. For this reason, the results proposed start always from the evaluation of the performance matrix, which permits to extract the model optimal parameters.
To verify that the Kuramoto model can reproduce the experimental measurements, empirical and simulated FCs are correlated, by means of Pearson's correlation coefficient. In this work, the strongest correlation coefficients are inferred in the $8-12$ Hz and $12-20$ Hz frequency bands, consistently with experimental MEG acquisitions and parallel studies[5, 55]. However, it is worth recalling that the intrinsic frequency of oscillation, common to all network nodes, is set at $f_n = 40$Hz, the factor that yields to a recessing oscillation frequency is the time delay. This allows the oscillator subsystems to synchronize in a more stable state, characterized by a reduced collective frequency, in the $\alpha$ and $\beta$ rhythms[5, 45]. In this statement, we extract the crucial role of time delay, which is shown by the presented results. Moreover, the results point at another aspect: the whole network never fully synchronize, but subsystems, which are structurally interconnected, do. This result is evidenced by the order parameter $R(t)$, which is never bigger than 0.4. In addition to this, the standard deviation of the synchrony degree, $0.1 < \sigma_R < 0.2$, infers the existence of different subsystems within the network, that temporally synchronize and then dissolve, resembling the metastability regime characterizing resting-state brain networks.

### 7.1.1 Considerations on the Model Parameters

As proposed in section 6.1, there is a mismatch between the optimal model parameters obtained in our analysis, and the optimal combination inferred by Cabral et Al. 2014a. To explain this result, a few considerations are proposed. Concerning k, the observation focuses on the different *b-values* characterizing DTI measurements. This coefficient affects the strength of the applied gradient field: the higher the b-value, the stronger the measured diffusion effect, and the lower the signal to noise ratio. Therefore, the detectable strength of connection between pairs of brain regions decreases with low b-values. This observation might refer to the detected alteration of the parameter k that is observed in this analysis, with respect to [5]. However, the relationship between k and b-value has never been investigated, and further analyses are required to understand what is the effect of one parameter on the other.

Second, a consideration on the model parameter $\tau$ is proposed. This parameter is defined in function of the conduction velocity, $\tilde{\tau} = \tilde{D}/v$, from which we can extract the average conduction velocity simulated by the model. The average Distance Matrix, D, is an underestimation of the actual distance between brain regions, since real anatomical communication pathways never resemble a straight line as they are modeled when designing the structural connectivity matrix. For example, axonal tracts connecting regions in different hemispheres pass through the corpus callosum, drawing a curve that is longer than the straight line between the two regions, assumed by the distance matrix. Therefore, the conduction velocity, v, is expected to be higher than the one simulated by the model. The average velocity extrapolated by the optimal average time delay resulted from this analysis is about 4 m/s, that, with respect to the considerations proposed, can be included in the average range of physiological plausibility for conduction velocity in myelinated neurons, $5-20$ m/s[57]. To conclude, the mismatch with the reference paper could be related to a difference in the employed distance matrix, D.

## 7.2 Objective II: Group level Simulations

After proving that the Kuramoto model successfully reproduces experimental observations and the literature findings, the model is applied to simulate brain network activity, considering groups of subjects with different pathological conditions. In this thesis, the condition in examination is Multiple Sclerosis, MS, and the results concerning this condition are compared to those related to the healthy control population. In Multiple Sclerosis, cognitive impairment, CI, is assessed in

more than 50% of the MS population[13]. In MS research, it is of main interest to find a reliable and objective parameter to assess CI[14]. The cognitive domain which this thesis focuses on is the information processing speed, IPS, whose impairment is related to a decreased conduction velocity. The Kuramoto model parameter $\tau$, time delay, is defined in function of the conduction velocity, as shown in the previous section. Therefore, we want to observe the capability of the model to adapt its parameters depending on the group in analysis. Eventually, this property could further be exploited to assess IPS impairment.

The first step of the analysis is performed at the population level. The average SC of the considered group is given in input to the model, and the simulated FC is correlated with the average empirical FC. The pair of model parameters that yields the strongest correlation coefficients is expected to vary case by case, by relating the model dynamics to the brain network dynamics. This part of the work is an intermediate analysis, that provides the observations required for the further step. However, interesting conclusions can be inferred.
The strongest correlation coefficients are obtained in the $8-10$ Hz and $10-12$ Hz frequency bands, consistently with the previous results. Furthermore, considering HC and MS simulations, the region of strong correlation coefficients is observed to vary its distribution in the model performance grid between the two cases. More specifically, this area is shifted toward an increased time delay in the MS population, and this is displayed in figure 7.1. Physiologically, this trend is consistent with the decreasing conduction velocity and information processing speed, detected in MS.

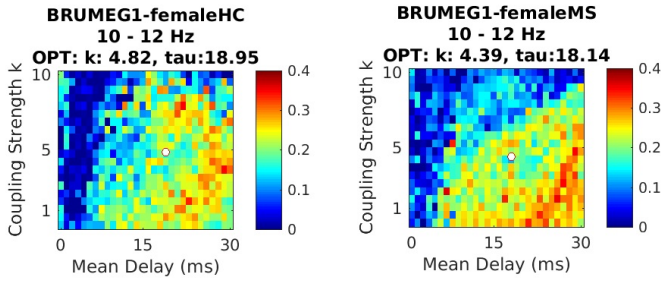


**Figure 7.1:** The figure proposes the comparison of the model performances between HC and MS, in the $8-10Hz$ frequency band. The aim is to observe the distribution of high correlation coefficients region.

A last observation concerns the difference between the simulation results regarding male and female populations. As shown in section 6.2.2, the shifting effect mentioned above, is more pronounced in male than in female groups. These results are consistent with a recent study that observes a stronger FC disruption in male than in female patients[24]. These results accentuate the good performance of the Kuramoto model in detecting pathological conditions at the population level. Given this promising observations at the group level, the next step regards the implementation of the model at a finer scale, the subject level.

## 7.3 Objective III: Subject Level Simulations

The results concerning the model implementation at the subject level elicit conclusions on two different aspects. Therefore, two separate sections are proposed to analyze the results obtained in this part of the work.

### 7.3.1 Model Parameters Correlation

The first conclusions are inferred from the plots global coupling strength, k, versus mean time delay, $\tau$, shown in figures 6.32 and 6.33. As shown in table 6.3, moderate to strong negative correlation is observed between the model parameters in the simulations regarding BRUMEG2 dataset, mainly in the $\alpha$ frequency band. This trend infers an increasing $\tau$, time delay, when the global coupling strength, k, decreases. Considering the physiological implications of this observation, an increment in time delay corresponds to a decreased conduction velocity, for the relationship expressed in equation 3.3, which might be related to damages of the communication network tracts, or a disruption of the FC matrix. The correlated behaviour of the two model parameters can be related to the scenario described by the Kuramoto model. The time delay affects the interactions between two nodes, whereas the coupling strength, k, weights the global interactions. This last parameter is inserted to maintain the whole system coupled. Therefore, a possible conclusion refers to the decreasing coupling strength required to maintain the whole system coupled, when the time delay between phases increases. However, the relationship between these two model parameters is not investigated in detail within the literature, and further analysis might be interesting to pursue.

It is very important to link the results elicited by the simulations to the physiological context of analysis. This is because the model is implemented to simulate a neurophysiological system, and outcome variations can be related to changes in a neuroanatomical or neurophysiological aspect. The simulation results concerning BRUMEG1 do not find the same correlation pattern between the model parameters, and one is reminded of the difference in the DTI b-value concerning the two distinct datasets, BRUMEG1 and BRUMEG2. Different DTI b-values show a relevant effect in these results.

### 7.3.2 Correlation $\alpha$-peak and Model Parameters

A further step in the assessment of IPS impairment, consists in observing the conservation of the model capability to adapt to different conditions, when the simulations are performed at the subject level. Therefore, the last part of this thesis aims at finding a possible correlation between $\tau$, time delay, and IPS. Since it is impossible to directly measure IPS and conduction velocity, a third measure that is found to correlate with CI is employed: the power $\alpha$-peak, a parameter that is detected in resting-state brain activity measurements. In this study, we extract the frequency content of the MEG signal, a frequency window is selected, i.e. $7-12$ Hz, and the peak within this band is elicited, which is assumed to be the power $\alpha$-peak. This parameter is found to correlate with CI in early MS[51]. More precisely, slowing down of $\alpha$-peak frequency is detected in MS population. Therefore, a correlation between $\tau$ and $\alpha$-peak is investigated.

A shallow observation of the scatterplots, where the empirical $\alpha$-peaks are plotted in function of the model parameters, does not allow to infer a correlation between these variables, as shown in figure 6.36 and 6.37. The Pearson's correlation coefficients obtained in table 6.5 support this statement. This thesis' results do not prove the assumption of a correlation between an increasing conduction delay due to demyelination, and the shifting $\alpha$-peaks detected in MS. There are several aspects that could affect these outcomes, and here only the most relevant ones are pointed out.

First, an observation on the $\alpha$-peak: this parameter shows an inter-subjects variability in HC subjects, and the actual peak can be slightly moved nearby the assumed 10 Hz. This is affected by different aspects, such as education, IQ, etc[14, 35]. In addition to this, the $\alpha$-peak shift detected in MS is relatively subtle and the model parameters adaptation might not be able to follow the fine $\alpha$-peak variation. Possibly for this reason, the analysis on the correlation of the time delay $\tau$ parameter with the $\alpha$-peak was not found significant. Consistently with these observations, the complexity and heterogeneity characteristics of Multiple Sclerosis must be taken into account. The MS population included in our analysis comprehends patients in different stages of the disease, and with different disease onset. In the literature, $\alpha$-peak shifts correlated with CI are detected in early MS[6], and further researches are required to assess the possible development of the $\alpha$-peak variation along the disease course, and among different disease typologies.

Another observation concerns the computation of the FC. The employed Pearson's correlation coefficient does not allow to detect direct functional interactions, whereby a causal relationship occurs. There are other methods to compute FC, other approaches mentioned in section 2.1.2, which might be employed to assess FC from different perspective, leading to a better performance of the model. Moreover, a stationary perspective is utilized throughout this thesis, which captures the connectivity over the whole recording time, as an overview of all the brain activity. From these observations, it is noticeable how several aspects can be improved in the investigation workflow.

The last step of this work concerns the investigation of a significant difference between $\alpha$-peak averages related to the following groups: HC, MS, and MSB. The results shown in table 6.4 do not confirm what is present in the literature, and differences between groups are not elicited. Concerning BRUMEG1, the p-value related to the most interesting comparison, MS vs HC, results exactly on the significance threshold. On the other hand, BRUMEG2 results do not infer a significant difference for any comparison. A possible explanation of these results concern the wide variety of MS subjects considered. The available dataset includes patients affected by PRMS, PPMS, and other typologies. Furthermore, the pathology is assessed in different stages. As explained in section 1.2 and 2.1.2, the pathology presents different phato-physiological characteristics and effects, depending on the onset and the stage of the disease. This complexity, characterizing Multiple Sclerosis, in addition to the inter-subjects variability of the $\alpha$-peak parameter, display a context of investigation that contains several factors that can alter and affect the results. This last consideration entails the necessity to narrow the analysis to a more homogeneous and consistent dataset. For example, the reference paper where the $\alpha$-peak shift is detected, considers only early MS patients[6].

# Chapter 8

# Conclusions and Future Developments

The background knowledge of this thesis is very broad and varied, including many concepts gathered from different study fields, such as neuroimaging techniques, neurocomputational model and network science. In some parts of the analyses, it may prove difficult to maintain the focus on the ultimate goal. Nevertheless, this complexity characterizes also the strength of this promising research field. Throughout this thesis, we aim at introducing a new neurophysiological feature to assess cognitive impairment in Multiple Sclerosis, by employing a neurocomputational model. This last statement presents the two main aspects concerning this thesis: a neurophysiological feature, and a neurocomputational model.

## 8.1 Conclusions

In Multiple Sclerosis, Cognitive Impairment is detected in more than 50% of the MS population. In clinical practise, CI is assessed by neuropsychological tests that, however, present some drawbacks, such as operator-dependency, and results' alteration due to training-effect[3, 14]. In this context, neuroimaging techniques are more and more employed, in order to infer reliable and objective parameters that can assess CI in MS. The brain anatomy is investigated by neuroimaging techniques such as MRI, already introduced in clinical practice to assess structural damages' location and lesion load[14, 60]. Despite the important role and improvements in diagnosis and prognosis, neuroanatomical features entail a clinico-radiological paradox[3, 61]. This points at the discrepancy between structural damages assessed by MRI, and the clinical assessment of psycho-physical decline. It is thought that including neurophysiological features might reduce this paradox, and bring in additional information[14, 61]. This last observation relates to the relationship between structural and functional brain networks, which can be described by Structural and Functional Connectivity, respectively. Although structural connections are always found to guide functional interactions, FC does not always show direct structural pathways underlying interacting regions. Therefore, this relationship between FC and SC is still under investigation[26, 39]. Despite the fact that functional aspects are more difficult to interpret and assess, recent studies show the capability of neurophysiological quantities, such as Functional Connectivity, to define reliable and objective **biomarker** in Multiple Sclerosis[24, 51, 61].

As far as this thesis is concerned, the innovative neurophysiological feature that we want to introduce is not extrapolated by a neuroimaging technique, but it is a parameter of a neurocomputational model, employed to simulate brain activity. The implementation of a biophysical model carries a new perspective in brain activity investigation: a bottom-up approach[41]. This allows to observe the mechanisms from which brain activity arises, and different scenarios can be designed[4].

Nevertheless, two aspects guide the model design[7]. First, the neurophysiological realism: model's parameters should reflect a characteristic of the physiological mechanisms that the model aims at reproducing. Moreover, to validate the model performances, the simulated brain activity is then compared to neuroimaging measurements. In this specific work, the empirical functional connectivity is extracted from resting-state MEG data, by computing the Pearson's correlation coefficients between amplitude envelope fluctuations related to each pair of brain regions. This empirical FC is correlated, by means of Pearson's correlation coefficient, with the simulated FC. In addition to this, some structural information is required by model inputs or design features. Consequently, the neuroimaging techniques properties dictate the spatio-temporal resolution of the model, to assure that the model assess the physiological aspect with the same perspective [8, 7].

Along this thesis, the implemented model is the *time-delayed coupled oscillators*, a variant of the Kuramoto model, which has successfully been employed to simulate resting-state brain activity in the literature[5, 55]. Several aspects make this model suitable for this work. First, an important assumption of the model is proposed: simulated functional networks are developed on a fixed structural network, that is provided to the model as input. Therefore, the underlying structural connections guide the functional interactions. Another important characteristic of the Kuramoto model concerns its parameter $\tau$, time delay. This factor is defined in function of the conduction velocity, a physiological quantity that is related to a cognitive domain, the information processing speed. This last results impaired in MS, and the IPS disruption is related to a decreasing conduction velocity[13]. However, there is no direct measurement that allows to assess the conduction velocity. By employing the Kuramoto model, the time delay that allows to find the strongest correlation coefficients between empirical and simulated activity, can infer the conduction velocity characterizing the brain dynamics. Therefore, in this context, time delay could be claimed as a biomarker to assess IPS.

Along this work, the model performance reproduces the results present within the literature, and simulated brain activity is found to optimally correlate with empirical data. Afterwards, the model is applied to simulate brain activity when groups of subjects with different conditions are considered, specifically, healthy controls, HC, and MS patients. The pair of model parameters that yields the strongest correlation coefficients is expected to vary case by case, by relating the model dynamics to the brain network dynamics. This assumption is verified when the model is implemented at the group level, and a qualitative observation infers an increasing time delay in those simulations concerning the MS population. When the analysis is narrowed down at the subject level, the model parameter, time delay, is correlated with the power $\alpha$-peak. The frequency at which this peak is detected is known to correlate with CI in early MS[6]. Therefore, it is used as an intermediate parameter to verify the adaptation of the time delay in MS patients. Despite the promising results when the model is employed at the group level, at a finer scale, the correlation between the model parameter and the intermediate neurophysiological feature, $\alpha$-peak, is not inferred, and neither is a significant difference between mean time delay related to different groups of subjects, MS and HC. Eventually, the model parameter $\tau$, is not proved to detect decreasing conduction velocity in MS. However, this is a subtle effect, and this investigation might be limited by the computation of FC, and the static perspective of analysis.

Another result obtained throughout this analysis concerns the comparison between $\alpha$-peak averages related to different groups of subjects, HC and MS. The shift towards low frequencies shown in the literature for MS patients is not detected, furthermore, no significant difference is elicited by the comparison of the $\alpha$-peak averages considering MS and HC groups[6]. The discrepancy between our results and the ones proposed in the literature can be caused by the different groups of MS patients in analysis. In fact, a heterogeneous group of patients is included in the available dataset, in which different types of MS and at different disease's stages are considered. MS is a very complex pathology, where both neuroanatomy and neurophysiology are affected differently depending on the disease onset and stage. Therefore, a more narrowed and consistent dataset in composition might lead to more significant results. Considering all the observations presented so far, possible new methods and approaches are proposed in the next section.

## 8.2 Future Developments

Throughout this thesis, several aspects are presented, and in each one a possible different implementation or advanced approach can be introduced. However, in this section two main aspects are addressed, the neurocomputational model, and the perspective of analysis; some alternatives to those employed are proposed.

As far as the Kuramoto model is concerned, its performance can be improved by fine tuning the model parameters, since the collective frequency of oscillations is affected by connectivity coefficients, time delays, and oscillator intrinsic frequency[5]. For instance, by defining a *local* transmission speed within the structural brain network, therefore a local time delay parameter. However, this would increase substantially the computational demand. Again, another aspect regards the introduction of a *local* natural oscillatory frequency. These last observations concern the improvement of the already employed Kuramoto model. Nevertheless, the possibility to implement a new neurocomputational model must be considered. As explained in chapter 3, there are several scenarios designed to depict the mechanisms underlying brain activity, and each proposes a different insight of the experimental context. The Kuramoto model gives a mechanistic perspective, while different other scenarios, such as neural mass models, could provide a more realistic description, and lead to new findings.

A second possible approach focuses on a different method to compute and investigate the Functional Connectivity. A different technique to assess FC can be introduced, considering the ones proposed in table 2.1, such as Phase Lag Index, PLI, or Synchrony Likelyhood, SL. These methods have been successfully employed in different analyses to investigate functional networks from a different perspective[62]. Furthermore, with the introduction of M/EEG in neurophysiological investigations, the time resolution for assessing brain activity has greatly improved with respect to classic fMRI acquisitions. Some studies have already detected the existence of meta-stable states that last only for $100 - 200$ ms[4, 51]. These observations yield the investigation of a *dynamic* functional connectivity, studying the fast alternation of brain activation patterns. This approach would allow a finer examination of the brain functional networks disruption.

So far, new approaches are proposed. However, a possible future analysis might consider to reproduce the work conducted throughout this thesis, selecting, from the available dataset, a set of MS patients that is consistent in MS typology and disease stage. This might help to reduce the inter-subjects variability characterizing MS, and some of the parameters employed along the analysis, such as the power $\alpha$-peak.

# Bibliography


[1] S. L. Hauser and J. R. Oksenberg, "The Neurobiology of Multiple Sclerosis: Genes, Inflammation, and Neurodegeneration," *Neuron*, vol. 52, no. 1, pp. 61–76, 2006.

[2] C. P. Kamm, B. M. Uitdehaag, and C. H. Polman, "Multiple sclerosis: Current knowledge and future outlook," *European Neurology*, vol. 72, no. 3-4, pp. 132–141, 2014.

[3] C. J. Stam, "Modern network science of neurological disorders," *Nature Publishing Group*, no. September, pp. 1–13, 2014. [Online]. Available: http://dx.doi.org/10.1038/nrn3801

[4] J. Cabral, M. L. Kringelbach, and G. Deco, "Functional connectivity dynamically evolves on multiple time-scales over a static structural connectome: Models and mechanisms," *NeuroImage*, vol. 160, pp. 84–96, 2017.

[5] J. Cabral, H. Luckhoo, M. Woolrich, M. Joensson, H. Mohseni, A. Baker, M. L. Kringelbach, and G. Deco, "Exploring mechanisms of spontaneous functional connectivity in MEG: How delayed network interactions lead to structured amplitude envelopes of band-pass filtered oscillations," *NeuroImage*, vol. 90, pp. 423–435, 2014. [Online]. Available: http://dx.doi.org/10.1016/j.neuroimage.2013.11.047

[6] M. L. V. D. Meer, P. Tewarie, M. M. Schoonheim, L. Douw, F. Barkhof, C. H. Polman, C. J. Stam, A. Hillebrand, and R.-s. Meg, "NeuroImage : Clinical Cognition in MS correlates with resting-state oscillatory brain activity : An explorative MEG source-space study ," *YNICL*, vol. 2, pp. 727–734, 2013. [Online]. Available: http://dx.doi.org/10.1016/j.nicl.2013.05.003

[7] M. W. Woolrich and K. E. Stephan, "NeuroImage Biophysical network models and the human connectome," *NeuroImage*, vol. 80, pp. 330–338, 2013. [Online]. Available: http://dx.doi.org/10.1016/j.neuroimage.2013.03.059

[8] S. Supek and C. J. Aine, *Magnetoencephalography From Signals to Dynamic Cortical Networks*, J. A. Cheryl and S. Selma, Eds. Springer Heidelberg New York Dordrecht London, 2014.

[9] Martini, Nath, and Bartholomew, *Fundamentals of Anatomy and Physiology*, 10th ed. PEARSON, 2015.

[10] S. Vanderberghe, V. Keereman, and P. Van Mierlo, *Neuromodulation and Imaging.*

[11] L. Scherwood, *Fondamenti di fisiologia umana*, 4th ed. PICCIN, 2012.

[12] M. D. Filippo, E. Portaccio, A. Mancini, and P. Calabresi, "Multiple sclerosis and cognition: synaptic failure and network dysfunction," *Nature Reviews Neuroscience*. [Online]. Available: http://dx.doi.org/10.1038/s41583-018-0053-9

[13] N. D. Chiaravalloti and J. Deluca, "Cognitive impairment in multiple sclerosis," 2008.

[14] J. V. Schependom and G. Nagels, "Targeting Cognitive Impairment in Multiple Sclerosis — The Road toward an Imaging-based Biomarker," vol. 11, no. June, pp. 2012–2017, 2017.

[15] A. Compston and A. Coles, "Multiple sclerosis," *The Lancet*, vol. 372, no. 9648, pp. 1502–1517, 2008. [Online]. Available: http://dx.doi.org/10.1016/S0140-6736(08)61620-7

[16] R. Dobson and G. Giovannoni, "Multiple Sclerosis - a review," *European Journal of Neurology*, pp. 0–2, 2018. [Online]. Available: http://doi.wiley.com/10.1111/ene.13819

[17] C. Stadelmann, C. Wegner, and W. Brück, "Inflammation, demyelination, and degeneration - Recent insights from MS pathology," *Biochimica et Biophysica Acta - Molecular Basis of Disease*, vol. 1812, no. 2, pp. 275–282, 2011. [Online]. Available: http://dx.doi.org/10.1016/j.bbadis.2010.07.007

[18] J. Herz, F. Zipp, and V. Siffrin, "Neurodegeneration in autoimmune CNS in fl ammation," vol. 225, pp. 9–17, 2010.

[19] H. Lassmann, W. Brück, C. Lucchinetti, and H. Lassmann, "Heterogeneity of multiple sclerosis pathogenesis : implications for diagnosis and therapy," vol. 7, no. 3, pp. 115–121, 2001.

[20] C. Stadelmann, C. Wegner, and W. Brück, "Biochimica et Biophysica Acta In fl ammation , demyelination , and degeneration — Recent insights from MS pathology," *BBA - Molecular Basis of Disease*, vol. 1812, no. 2, pp. 275–282, 2011. [Online]. Available: http://dx.doi.org/10.1016/j.bbadis.2010.07.007

[21] C. M. Poser, "The multiple sclerosis trait and the development of multiple sclerosis : Genetic vulnerability and environmental effect," vol. 108, pp. 227–233, 2006.

[22] P. Vub, G. N. Prof, J. D. K. Prof, M. Beatrice, P. Umons, M.-c. H. Prof, and G. Nagels, "Cognitive Impairment in MS Statistical and neurophysiological aspects Jeroen Van Schependom," 2015.

[23] B. O. Watson, "State of the art," pp. 345–367, 2012.

[24] M. Tahedl, S. M. Levine, M. W. Greenlee, R. Weissert, and J. V. Schwarzbach, "Functional Connectivity in Multiple Sclerosis : Recent Findings and Future Directions," vol. i, no. October, pp. 1–18, 2018.

[25] G. Gong, Y. He, L. Concha, C. Lebel, D. W. Gross, A. C. Evans, and C. Beaulieu, "Mapping Anatomical Connectivity Patterns of Human Cerebral Cortex Using In Vivo Diffusion Tensor Imaging Tractography," no. March, 2009.

[26] J. Cabral, M. L. Kringelbach, and G. Deco, "Exploring the network dynamics underlying brain activity during rest," *Progress in Neurobiology*, vol. 114, pp. 102–131, 2014. [Online]. Available: http://dx.doi.org/10.1016/j.pneurobio.2013.12.005

[27] "MRIquestions." [Online]. Available: http://mriquestions.com/index.html

[28] "Radiopaedia." [Online]. Available: https://radiopaedia.org/

[29] J. Veraart, D. H. J. Poot, W. V. Hecke, I. Blockx, A. V. D. Linden, M. Verhoye, and J. Sijbers, "More Accurate Estimation of Diffusion Tensor Parameters Using Diffusion Kurtosis Imaging," vol. 145, pp. 138–145, 2011.

[30] S. Malaysiana, P. Gabungan, O. Saiz, P. Tensor, D. Otak, and L. Bihan, "Determination of Optimum Combination of Voxel Size and b-value for Brain Diffusion Tensor Imaging," vol. 46, no. 1, pp. 67–74, 2017.

[31] J.-d. Tournier, S. Mori, and A. Leemans, "Diffusion Tensor Imaging and Beyond," vol. 1556, pp. 1532–1556, 2011.

[32] K. M. M. Koriem, "Multiple sclerosis: New insights and trends," *Asian Pacific Journal of Tropical Biomedicine*, vol. 6, no. 5, pp. 429–440, 2016.

[33] T. E. J. Behrens, H. J. Berg, S. Jbabdi, M. F. S. Rushworth, and M. W. Woolrich, "Probabilistic diffusion tractography with multiple fibre orientations : What can we gain ?" vol. 34, pp. 144–155, 2007.

[34] M. Woolrich, L. Hunt, A. Groves, and G. Barnes, "NeuroImage MEG beamforming using Bayesian PCA for adaptive data covariance matrix regularization," *NeuroImage*, vol. 57, no. 4, pp. 1466–1479, 2011. [Online]. Available: http://dx.doi.org/10.1016/j.neuroimage.2011.04.041

[35] G. L. Colclough, M. W. Woolrich, P. K. Tewarie, M. J. Brookes, A. J. Quinn, and S. M. Smith, "NeuroImage How reliable are MEG resting-state connectivity metrics ?" *NeuroImage*, vol. 138, pp. 284–293, 2016. [Online]. Available: http://dx.doi.org/10.1016/j.neuroimage.2016.05.070

[36] C. J. Stam, E. C. W. V. Straaten, E. V. Dellen, P. Tewarie, G. Gong, A. Hillebrand, J. Meier, and P. V. Mieghem, "The relation between structural and functional connectivity patterns in complex brain networks," *International Journal of Psychophysiology*, vol. 103, pp. 149–160, 2016. [Online]. Available: http://dx.doi.org/10.1016/j.ijpsycho.2015.02.011

[37] "Cambridge Dictionary." [Online]. Available: https://dictionary.cambridge.org/dictionary/english/network

[38] Y. Sun, R. Lee, Y. Chen, S. Collinson, and N. Thakor, "Progressive Gender Differences of Structural Brain Networks in Healthy Adults : A Longitudinal , Diffusion Tensor Imaging Study," pp. 1–18, 2015.

[39] P. Tewarie, A. Hillebrand, E. van Dellen, M. M. Schoonheim, F. Barkhof, C. H. Polman, C. Beaulieu, G. Gong, B. W. van Dijk, and C. J. Stam, "Structural degree predicts functional network connectivity: A multimodal resting-state fMRI and MEG study," *NeuroImage*, vol. 97, pp. 296–307, 2014. [Online]. Available: http://dx.doi.org/10.1016/j.neuroimage.2014.04.038

[40] J. A. Pineda-pardo, R. Bruña, M. Woolrich, A. Marcos, A. C. Nobre, F. Maestú, and D. Vidaurre, "NeuroImage Guiding functional connectivity estimation by structural connectivity in MEG : an application to discrimination of conditions of mild cognitive impairment," *NeuroImage*, vol. 101, pp. 765–777, 2014. [Online]. Available: http://dx.doi.org/10.1016/j.neuroimage.2014.08.002

[41] P. Kogut, J. Darvill, D. Rosenbluth, and D. Morgenthaler, "Top Down Bottom Up Brain Models," vol. 41, pp. 69–74, 2014.

[42] T. D. Satterthwaite, D. H. Wolf, D. R. Roalf, K. Ruparel, G. Erus, S. Vandekar, E. D. Gennatas, M. A. Elliott, A. Smith, H. Hakonarson, R. Verma, C. Davatzikos, R. E. Gur, and R. C. Gur, "Linked Sex Differences in Cognition and Functional Connectivity in Youth," no. September, pp. 2383–2394, 2015.

[43] B. Landeau, D. Papathanassiou, F. Crivello, O. Etard, N. Delcroix, B. Mazoyer, and M. Joliot, "Automated Anatomical Labeling of Activations in SPM Using a Macroscopic Anatomical Parcellation of the MNI MRI Single-Subject Brain," vol. 289, pp. 273–289, 2002.

[44] T. T. Nakagawa, M. Woolrich, H. Luckhoo, M. Joensson, H. Mohseni, M. L. Kringelbach, V. Jirsa, and G. Deco, "NeuroImage How delays matter in an oscillatory whole-brain spiking-neuron network model for MEG alpha-rhythms at rest," *NeuroImage*, vol. 87, pp. 383–394, 2014. [Online]. Available: http://dx.doi.org/10.1016/j.neuroimage.2013.11.009

[45] G. Deco, J. Cabral, M. W. Woolrich, A. B. Stevner, T. J. van Hartevelt, and M. L. Kringelbach, "Single or multiple frequency generators in on-going brain activity: A mechanistic whole-brain model of empirical MEG data," *NeuroImage*, vol. 152, no. November 2016, pp. 538–550, 2017.

[46] E. Florin and S. Baillet, "HHS Public Access," pp. 26–35, 2016.

[47] A. Manuscript and T. M. Brain, "NIH Public Access," vol. 81, no. 1, pp. 35–48, 2015.

[48] E. Angelakis, J. F. Lubar, S. Stathopoulou, and J. Kounios, "Peak alpha frequency : an electroencephalographic measure of cognitive preparedness," vol. 115, pp. 887–897, 2004.

[49] M. Bonnefond and O. Jensen, "Gamma Activity Coupled to Alpha Phase as a Mechanism for Top-Down Controlled Gating," pp. 1–11, 2015.

[50] E. Angelakis, J. F. Lubar, and S. Stathopoulou, "Electroencephalographic peak alpha frequency correlates of cognitive traits," vol. 371, pp. 60–63, 2004.

[51] Q. van Geest, L. Douw, S. van 't Klooster, C. E. Leurs, H. M. Genova, G. R. Wylie, M. D. Steenwijk, J. Killestein, J. J. Geurts, and H. E. Hulst, "Information processing speed in multiple sclerosis: Relevance of default mode network dynamics," *NeuroImage: Clinical*, vol. 19, no. April, pp. 507–515, 2018. [Online]. Available: https://doi.org/10.1016/j.nicl.2018.05.015

[52] P. Tewarie, "Explaining the heterogeneity of functional connectivity findings in multiple sclerosis An empirically informed m.pdf," 2018.

[53] J. A. Acebrón, R. Spigler, D. Matematica, R. Tre, and L. S. L. Murialdo, "The Kuramoto model : A simple paradigm for synchronization phenomena," vol. 77, no. January, 2005.

[54] E. Montbri and D. Paz, "Kuramoto model for excitation-inhibition-based oscillations," pp. 1–5, 2018.

[55] J. Cabral, E. Hugues, O. Sporns, and G. Deco, "Role of local network oscillations in resting-state functional connectivity," no. May 2018, 2011.

[56] R. Schmidt, K. J. R. Lafleur, M. A. D. Reus, and L. H. V. D. Berg, "Kuramoto model simulation of neural hubs and dynamic synchrony in the human cerebral connectome," *BMC Neuroscience*, pp. 1–13, 2015.

[57] W. H. Lee and S. Frangou, "Emergence of Metastable Dynamics in Functional Brain Organization via Spontaneous fMRI Signal and Whole - Brain Computational Modeling," *2017 39th Annual International Conference of the IEEE Engineering in Medicine and Biology Society (EMBC)*, pp. 4471–4474, 2017.

[58] "MWW test." [Online]. Available: https://nl.mathworks.com/matlabcentral/fileexchange/25830-mwwtest

[59] S. Helbling, "M / EEG Source Reconstruction," 2015.

[60] L. Leocani, T. Locatelli, V. Martinelli, M. Rovaris, M. Falautano, M. Filippi, G. Magnani, G. Comi, and S. R. V, "Electroencephalographic coherence analysis in multiple sclerosis : correlation with clinical , neuropsychological , and MRI findings," vol. 3, pp. 192–198, 2000.

[61] P. Tewarie, M. M. Schoonheim, C. J. Stam, M. L. V. D. Meer, and B. W. Van, "Cognitive and Clinical Dysfunction , Altered MEG Resting- State Networks and Thalamic Atrophy in Multiple Sclerosis," vol. 8, no. 7, 2013.

[62] M. J. Brookes, J. M. Zumer, C. Stevenson, and S. T. Francis, "Neuroimage," no. February, 2011.

# Appendix A

# MATLAB Code: Simulation Function

This appendix contains the main function used to performed all the analyses conducted along this thesis. These have been performed both on a local computer cluster, *cray-Z*, and on a remote supercomputer, *Hydra*, which have a huge computational power, allowing to significantly reduce the running time of each simulation to few days. This function is coded in such a way, so that can be used in both the environments without massive changes, the saving directory is the only item to be redefined.

The algorithm develops the workflow explained in chapter 5. The inputs are the Functional and Structural connectivity matrices of the group of subjects considered in the simulation, the settings' parameters, among which the filtering frequency bands are included, and the Distance matrix. This function recalls another important function, the *Network-Kuramoto()*, which can be found in literature [55]. This last codes for the actual Kuramoto Model, and the simulated phases are returned as outputs. After the model's simulation, the frequency content is extracted as well as the simulated Functional Connectivity, and the Pearson's correlation coefficient between simulated and empirical FC matrices is computed. These mentioned steps characterize the core of this function, which is enclosed in two for loops, over the two model's parameters $k/\tau$. To decrease the computational time, the second loop is coded as a *parfor* loop.

```
function [] = run_Kuramoto(filename,Dname,settingsfile)
%% load input:

%filemane = file in which both functional and structural
%connectivity are saved (char)
%Dname = file in which Distance matrix is saved(char)
%settingsfile = file in which all the settings are saved, such as
%freq bands, sampling, etc. Later on the employed
settings are identified.(char)

load(settingsfile) %load('settings.mat')
load(filename)
d=load(Dname);

%Definition of FC and SC with respect to the file uploaded by filename
FC=FC;
SC=SC;

%definition of the output file name:
```

```
[a,b,c]     = fileparts(filename);

%when working on Hydra
outputfolder='/u/chrossi/simulations/output/'
%when working on cray-Z
outputfolder='/home/crossi/Kuramoto_Chiara2/simulations/output';
if not(exist(outputfolder,'dir'))
    mkdir(outputfolder);
end
outputfile = [outputfolder b '_output' c];

%% The MaGiC:
% in this section the real simulation occurs

% SC              = Matrix of coupling strengths (NxN) between pairs of
%                   regions. It can be directed (i to j) and/or weighted.
% D               = Matrix of distances (in mm) (NxN)
% frequency_mean  = Neural populations average intrinsic frequency (Hz)
% f_std           = Standard deviation of intrinsic frequencies across reg.
%                   Can be 0 if all oscillators are equal.
% f_dist          = Distribution of intrinsic frequencies (Nx1).
                    %If all equal, than f_dist=ones(N,1)
% t_max           = Total time of simulated activity (seconds)
% dt              = Integration step (smaller than delays) (seconds)
%                   (ex. 1e-4)
% sampling        = sampling for saving simulated activity (ex. 10)
%                   => 10*dt = 1e-3 s = 1ms
% sig_n           = Standard deviation of noise (can be zero)

% addpath('/home/crossi/Downloads/fieldtrip-20180930/');

%extraction of all the important parameters from the settings file.
frequency_mean = settings.frequency_mean; %40
f_std          = settings.f_st; %0
f_dist         = ones(90,1);
t_max          = settings.t_max; %140
dt             = settings.dt; %1e-4
sampling       = settings.sampling; %10
sig_n          = settings.sig_n; %0
grid_k         = settings.grid_k; %[(1:1:20)/2]
grid_tau       = settings.grid_tau; %[1:1:30]
Nfreq          = size(settings.freq_bands,1); %5->number of frequency bands
Np             = size(SC,1); %90 -> number of regions parcellation
N              =settings.freq_bands; %[1-4Hz,4-8Hz,8-10Hz,10-12H,12-20Hz]
% Calculate sampling frequency at which Network_Kuramoto will return:
dt_output = dt*sampling;
Fs = 1/dt_output; %Fs=1000

ds_n1 = 2*Fs %2 seconds of data

nk = numel(grid_k);
nt = numel(grid_tau);

%to extract nf:
sim_data = zeros(1,(t_max-20)*Fs); %delete the first 20 sec
              %to avoid transition period to be considered
[simulated_freqs,f] = pwelch(sim_data',[],[],[],Fs);
```

```
nf = numel(f);

%Initialisation
simulated_freqcontent = zeros(nk,nt,nf);
mean_R = zeros(nk,nt);
std_R  = zeros(nk,nt);

%for loop on parameter k
for i=1:nk
%Inizialization of variables
j_simulated_freqcontent = zeros(nt,nf);
j_mean_R                = zeros(1,nt);
j_std_R                 = zeros(1,nt);
j_correspondance        = zeros(Nfreq,nt);
newj_mean_R                = zeros(Nfreq,nt);
newj_std_R                 = zeros(Nfreq,nt);

%parfor loop on parameter tau
parfor j=1:nt
%definition of k-tau pair for the simulation
k   = grid_k(i);
tau = grid_tau(j);

% the Joana magic: real model's simulation
[ths] = Network_Kuramoto(SC,d.D,frequency_mean,f_std,f_dist,k,...
    tau,t_max,dt,sampling, sig_n);

% Calculate simulated data: sinusoidal regime with constant amplitude
sim_data = sin(ths);

% Calculate the frequency content:
[simulated_freqs,f] = pwelch(sim_data',[],[],[],Fs);

%the simulated content saved is the average over all 90nodes' activities
j_simulated_freqcontent(j,:) = mean(simulated_freqs,2);

% Calculate R(t) order parameter
OrderParameter = sum(exp(1i.*ths),1)/Np;
R = abs(OrderParameter);
j_mean_R(j) = mean(R);
%Metastability
j_std_R(j)  = std(R);

% Calculate correspondence empirical and simulated FC in each freq band
for l=1:Nfreq
filtereddata = ft_preproc_bandpassfilter(sim_data, 250, [N(l,1) N(l,2)],...
    4, 'but', 'twopass', 'reduce');
%extract amplitude envelope
HA = abs(hilbert(filtereddata));
%filtering to extract amplitude envelope fluctuation
HA_lowpass = ft_preproc_bandpassfilter(HA,250,[0.01  0.1],5,...
    'but','twopass','reduce'); % used to be 0.1-0.5
HA_lowpass_mean = mean(HA_lowpass,2);
%delete common line
HA_lowpass = HA_lowpass - repmat(HA_lowpass_mean,1,size,(HA_lowpass,2));

%Downsample:
```

```
%number of simulated seconds for downsampled data --> half of
%the real number of simulated secs. the transient is discarded
n_downsampled = floor((t_max-20)/2);
%initialize downsampled data
HA_ds = zeros(n_downsampled,size(HA,1)); %size of HA_ds

for p=1:n_downsampled
mini = (p-1)*ds_n1+1; %time*freq
maxi = p*ds_n1;
HA_ds(p,:) = mean(HA(:,mini:maxi),2); %the averaged is made
%between the time points selected->row dimension
end

simu_FC = corr(HA_ds);
% Correspondance with real FC:
%we only compare upper diagonal of FC because it is symmetric
%(Pearson's correlation Coefficient)
idx_of_interest   = find(triu(ones(90),1));
% Extract real frequency content:
real_FC = FC(idx_of_interest);%only the upper triangular matrix
%is interesting since the connectivity matrix is symmetric
% Extract simulated frequency content:
simu_FC = simu_FC(idx_of_interest);
% Make the comparison:
j_correspondance(l,j) = corr(real_FC,simu_FC);

% Calculate the phase of the hilbert transform
HA_phase = angle(hilbert(HA_lowpass));

% Calculate the order parameter and metastabilility for each freq band:
OrderParameter = sum(exp(1i.*HA_phase),1)/90;
R = abs(OrderParameter);
newj_meanR(j,1)= mean(R);
newj_metastability(j,1)= std(R);
end

fprintf('Done : %2.0f / %2.0f - %2.0f / %2.0f \n',i,numel(grid_k)...
    ,j,numel(grid_tau));
end
%gather all results for the tau parameter used.
simulated_freqcontent(i,:,:) = j_simulated_freqcontent;
mean_R(i,:) = j_mean_R;
std_R(i,:)  = j_std_R;
correspondance(i,:,:) = j_correspondance;
newmean_R(i,:,:) = newj_mean_R;
newstd_R(i,:,:)  = newj_metastability;

end
save(outputfile,'correspondance','mean_R','std_R','settings',...
    'simulated_freqcontent', 'newmean_R','newstd_R');
```

# Acknowledgement

I sincerely thank Prof. Jeroen Van Schependom and Prof. Guy Nagels for giving me the opportunity to approach a study field i am very interested in. Their perspective and passion for the research work inspired me. A special thank goes to Prof. Van Schependom, who patiently guided me along this thesis. A quick talk or a simple suggestion always helped me moving forward. Thanks for pointing out the critical and weak points of my work, it helped me becoming more aware of it.
Ringrazio anche il Prof. Baselli che ha supervisionato il lavoro a distanza dando interessanti consigli. Purtroppo non le condizioni di questo ultimo anno non hanno aiutato lo sviluppo della collaborazione, ma l'interesse dimostrato nei pochi incontri ha reso il ritorno in Italia sicuramente più semplice.

I want to thank all the CIME members i shared this year with. Thanks to Johan and Lars for their help and kindness, especially during my worst crises. Thanks for pointing out only few times my italian temperament and accent, and always laughing at it. You taught me how to take care of plants, this will be very useful for my future! Thanks to Stijn, my dear office-mate, your laughs and cookies supported me along the work. Thanks to my Brazilian friends, Eric and Murillo, for the long discussion on Pizza that i constantly won supported by our very good chef Lars. Thanks to everybody for the "bothering time" that helped going through long days. All the team building events, every lunch and every laugh have characterized this challenging but great year in this group. I hope you will sometimes remember the small enthusiastic italian girl running around the corridor, because you will all remain as a permanent beautiful memory of my belgian lifetime. Grazie!

Last but not least, i thank my super family. Despite the difficult year and the distance, you never miss to support, and guide me. And I will always carry you all with me around the world, as i promised to my favourite person in the world.

Chiara